

CHARATERIZATION OF NEUTRON DOSIMETERS CONTAINING
PERFORATED NEUTRON DETECTORS

By

QUAJI MONWAR JAHAN

B.S., University of Dhaka, 1993
M.S., Kansas State University, 2004

A THESIS

Submitted in partial fulfillment of the requirements for the degree

MASTER OF SCIENCE

Department of Mechanical and Nuclear Engineering
College of Engineering

KANSAS STATE UNIVERSITY
Manhattan, Kansas

2008

Approved by:

Major Professor
William L. Dunn

Abstract

Neutron dosimeters measure neutron doses but portable, real time, high efficiency, and gamma insensitive neutron dosimeters are not commonly available. Characterization of a newly invented neutron dosimeter, based on perforated semiconductor neutron detectors (SNDs) whose perforations are filled with neutron reactive material, was the main purpose of this research study. The characterization procedure was performed by both simulation and experiment. The Monte Carlo N-Particle (MCNP) transport code was used to model a boron-filled dosimeter and to study the responses when the dosimeter was located on the surfaces of a water phantom and an anthropomorphic phantom for parallel beams of neutrons having various energy spectra. A pair of detectors was modeled: one bare and one Cd-filtered. Dosimeter responses were normalized for a beam that would produce 1 mSv ambient dose equivalent if incident on the ICRU sphere phantom. Dosimeter responses were estimated at different positions on the torso and it was found that the responses are relatively insensitive to the placement on the torso. For 100% efficient detectors and for beam with a Watt spectrum incident from front to back of the phantom, the bare detector produces about 140 counts per μSv and the Cd-filtered detector produces about 80 counts per μSv .

The experimental characterization study involves observing SND counts with the dosimeter placed on an anthropomorphic torso phantom and determining the corresponding neutron dose. A TLD pair method was used to determine the neutron dose on the surface of the phantom. The neutron reactive material of the dosimeter was ${}^6\text{LiF}$, which is different from that assumed for the modeled dosimeter. A bare dosimeter response collected over 10 min was 25113 ± 158 counts and the corresponding neutron dose was measured to be 2.57 mSv. The Cd-filtered dosimeter response collected over 10 min was 23886 ± 155 counts and the corresponding neutron dose was measured to be 2.32 mSv.

The neutron dosimeters are capable of detecting doses in the μSv range and above, and are anticipated to provide direct read-out in dose units in future using count-to-dose conversion factors for bare and Cd-filtered SNDs.

Table of Contents

List of Figures	vi
List of Tables	x
Acknowledgement	xii
Dedication	xiii
1 Introduction.....	1
2 Background.....	4
2.1 Neutron Detectors.....	4
2.1.1 Cadmium Cutoff.....	4
2.1.2 Slow Neutron Detection.....	5
2.1.3 Fast Neutron Detection.....	5
2.2 Neutron Dosimeters.....	5
2.2.1 Active Dosimeters.....	6
2.2.1.1 Tissue-Equivalent Proportional Counters (TEPC).....	6
2.2.1.2 Semiconductor Based Neutron Dosimeters.....	7
2.2.1.3 Bonner Sphere (Moderating Detector).....	7
2.2.2 Passive Dosimeters.....	8
2.2.2.1 Albedo Neutron Dosimeters (or Thermoluminescent Dosimeters).....	8
2.2.2.2 Etch-Track Dosimeter.....	8
2.2.2.3 Bubble Dosimeters.....	9
2.3 Radiation Quality and Dose Equivalent.....	9
2.3.1 Absorbed Dose.....	10
2.3.2 Quality Factor and Linear Energy Transfer (LET).....	10
2.3.3 Dose Equivalent.....	11
2.3.4 Operational Dose Quantities.....	11
2.3.5 Ambient Dose Equivalent.....	11
2.3.6 Personnel Dose Equivalent.....	12
2.4 Fluence-to-Dose Conversion.....	12
2.5 Phantoms.....	12

2.5.1	Reference Computational Model (or ICRU sphere)	13
2.5.2	Computational Anthropomorphic Phantom	13
2.5.3	Phantom Used for Detector Characterization	14
3	Monte Carlo Study for Characterization of Semiconductor Neutron Dosimeters	16
3.1	Theoretical Consideration of the Detector	16
3.2	Model Geometry for the Neutron Detector	17
3.3	Model Geometry for Water Phantom	18
3.3.1	Normalization Constants	19
3.3.2	MCNP Tally	22
3.3.3	Results and Discussion of Results	23
3.4	Anthropomorphic phantom	27
3.4.1	Model Geometry for Anthropomorphic Phantom	29
3.5	Results and discussion	29
3.5.1	Detectors on Chest Irradiated from Front (AP Incidence)	29
3.5.1.1	Spectrum Determination Constant	35
3.5.2	Detectors on Chest Irradiated from Left and Right	36
3.5.3	Detectors on Chest Irradiated from Back (PA Incidence)	44
4	Characterization of Semiconductor Neutron Dosimeter Experimental Study	48
4.1	Calculation of Neutron Flux	48
4.1.1	Efficiency of HPGe Detector	48
4.1.1.1	Theory	49
4.1.1.2	Methods for Calculation of Counts under the Peak	49
4.1.1.3	Experimental Procedure	51
4.1.1.4	Results and Discussion	53
4.1.2	Measurement of Flux	54
4.1.2.1	Theory	55
4.1.2.1.1	Activation with Cd-Covered Gold Foil	58
4.1.2.1.2	The Cadmium Ratio	59
4.1.2.1.3	Flux Perturbation and Self-Shielding	61
4.1.2.1.4	Self-Shielding for Thermal Neutrons	61
4.1.2.1.5	Self-Shielding for Epi-Thermal Neutrons	62
4.1.2.2	Experimental Procedure	62

4.1.2.3	Results.....	63
4.2	Measurement of Dose on the Surface of the Anthropomorphic Phantom	63
4.2.1	Thermoluminescent Dosimeters and Their Characteristics.....	64
4.2.1.1	Thermal Neutron Response Using TLDs.....	65
4.2.1.2	TLD Reader	65
4.2.1.3	Annealing of TLDs	66
4.2.1.4	Experimental Procedure.....	67
4.2.1.5	Results and Discussion of Results	67
4.2.2	Anthropomorphic Torso Phantom and TLDs	69
4.2.2.1.1	Results.....	70
4.2.3	Testing of Semiconductor-Based Neutron Dosimeter with the Phantom. 71	
4.2.3.1	Semiconductor-Based Neutron Dosimeter	71
4.2.3.2	Experimental Procedure.....	71
4.2.3.3	Results using Semiconductor-Based Neutron Dosimeter.....	74
5	Conclusion and Suggestions for Future Work	77
	References.....	79
	Appendix A - Monte Carlo Simulation Code Input Files.....	83
A.1.	Water Phantom.....	83
A.2.	Anthropomorphic Phantom.....	86
	Appendix B - Detailed Calculations for Neutron Dosimeter Modeling	93
B.1.	Calculation of Atom Density for ¹⁰ B Material.....	93
B.2.	Description to Calculate Detector Offset Position at x = 10 cm.....	94
B.3.	MCNP Neutron Dosimeter Normalization Constant	95
B.3.1	Watt Spectrum	95
B.3.2	Maxwellian Spectrum	96
B.3.3	Mono-Energetic Neutron Beam.....	96
	Appendix C - Efficiency of HPGe Detector	98
	Appendix D - Detail Calculation of Thermal and Epi-thermal Flux	100
D.1.	Flux Calculation.....	100
<i>Calculation of Fast Flux</i>		104
D.2.	Calculation of Propagation of Error.....	105
	Appendix E - Calculation of Dose	109

List of Figures

Figure 2.1. The ICRU Sphere.	13
Figure 2.2. Anthropomorphic Torso Phantom, Used for the Present Study.	15
Figure 3.1. Comparison of Neutron Cross Sections for ^{10}B and ^6Li material.	17
Figure 3.2. 70% Coverage of ^{10}B Material in the Si Semiconductor Substrate (Top View of a Detector).	18
Figure 3.3. Water Phantom with the Positions of Eight Pairs of Detectors (3-D view). ..	20
Figure 3.4. Water Phantom with the Positions of Eight Pairs of Detectors (2-D view). ..	20
Figure 3.5. Cylindrical Water Phantom (view in YZ plane), D1 ^{10}B Detector on the Surface of the Phantom and D2 is Cd-Coated ^{10}B Detector (not to scale).	21
Figure 3.6. Normalized Detector Responses on Water Phantom for 1-MeV Neutron Beam.	24
Figure 3.7. Normalized Detector Responses on Water Phantom for 2-MeV Neutron Beam.	24
Figure 3.8. Normalized Detector Responses on Water Phantom for 3-MeV Neutron Beam.	25
Figure 3.9. Normalized Detector Responses on Water Phantom for 4-MeV Neutron Beam.	25
Figure 3.10. Normalized Detector Responses on Water Phantom for 5-MeV Neutron Beam.	26
Figure 3.11. Normalized Detector Responses on Water Phantom for Watt Energy Distribution of ^{235}U	26
Figure 3.12. Normalized Detector Responses on Water Phantom for Maxwellian Energy Distribution of ^{235}U	27
Figure 3.13. Sectional View of Adult Male Anthropomorphic Phantom Modelled and the Positions of Pair Detectors.	28
Figure 3.14. Normalized Detector Responses on the Torso of the Anthropomorphic Phantom for 1-MeV Neutron Beam with AP Incidence.	30

Figure 3.15. Normalized Detector Responses on the Torso of the Anthropomorphic Phantom for 2-MeV Neutron Beam with AP Incidence.....	30
Figure 3.16. Normalized Detector Responses on the Torso of the Anthropomorphic Phantom for 3-MeV Neutron Beam with AP Incidence.....	31
Figure 3.17. Normalized Detector Responses on the Torso of the Anthropomorphic Phantom for 4-MeV Neutron Beam with AP Incidence.....	31
Figure 3.18. Normalized Detector Responses on the Torso of the Anthropomorphic Phantom for 5-MeV Neutron Beam with AP Incidence.....	32
Figure 3.19. Normalized Detector Responses on the Torso of the Anthropomorphic Phantom for Beam with a ^{235}U Watt-spectrum with AP Incidence.....	32
Figure 3.20. Normalized Detector Responses on the Torso of the Anthropomorphic Phantom for beam with a ^{235}U Maxwellian-Spectrum and with AP Incidence.....	33
Figure 3.21. Pu-Be Spectrum (Shultis and Faw, 2000).....	34
Figure 3.22. Normalized Detector Responses on the Torso of the Anthropomorphic Phantom for a Pu-Be Source and with AP Incidence.....	35
Figure 3.23. Normalized Detector Responses on the Torso of the Anthropomorphic Phantom for 1-MeV Neutron Beam and with LLAT Incidence.....	37
Figure 3.24. Normalized Detector Responses on the Torso of the Anthropomorphic Phantom for 2-MeV Neutron Beam and with LLAT Incidence.....	37
Figure 3.25. Normalized Detector Responses on the Torso of the Anthropomorphic Phantom for 3-MeV Neutron Beam and with LLAT Incidence.....	38
Figure 3.26. Normalized Detector Responses on the Torso of the Anthropomorphic Phantom for 4-MeV Neutron Beam and with LLAT Incidence.....	38
Figure 3.27. Normalized Detector Responses on the Torso of the Anthropomorphic Phantom for 5-MeV Neutron Beam and with LLAT Incidence.....	39
Figure 3.28. Normalized Detector Responses on the Torso of the Anthropomorphic Phantom for beam with a ^{235}U Maxwellian-Spectrum and with LLAT Incidence...	39
Figure 3.29. Normalized Detector Responses on the Torso of the Anthropomorphic Phantom for beam with a ^{235}U Watt-Spectrum with LLAT Incidence.....	40
Figure 3.30. Normalized Detector Responses on the Torso of the Anthropomorphic Phantom for 1-MeV Neutron Beam and with RLAT Incidence.....	40

Figure 3.31. Normalized Detector Responses on the Torso of the Anthropomorphic Phantom for 2-MeV Neutron Beam and with RLAT Incidence.....	41
Figure 3.32. Normalized Detector Responses on the Torso of the Anthropomorphic Phantom for 3-MeV Neutron Beam and with RLAT Incidence.....	41
Figure 3.33. Normalized Detector Responses on the Torso of the Anthropomorphic Phantom for 4-MeV Neutron Beam and with RLAT Incidence.....	42
Figure 3.34. Normalized Detector Responses on the Torso of the Anthropomorphic Phantom for 5-MeV Neutron Beam and with RLAT Incidence.....	42
Figure 3.35. Normalized Detector Responses on the Torso of the Anthropomorphic Phantom for Maxwellian-Spectrum of ^{235}U and with RLAT Incidence.....	43
Figure 3.36. Normalized Detector Responses on the Torso of the Anthropomorphic Phantom for beam with a ^{235}U Watt-Spectrum and with RLAT Incidence.....	43
Figure 3.37. Normalized Detector Responses on the Torso of the Anthropomorphic Phantom for beam with 1 MeV Neutron Beam and with PA Incidence.....	44
Figure 3.38. Normalized Detector Responses on the Torso of the Anthropomorphic Phantom with 2 MeV Neutron Beam and with PA Incidence.....	44
Figure 3.39. Normalized Detector Responses on the Torso of the Anthropomorphic Phantom for beam with 3 MeV Neutron Beam and with PA Incidence.....	45
Figure 3.40. Normalized Detector Responses on the Torso of the Anthropomorphic Phantom for beam with 4 MeV Neutron Beam and with PA Incidence.....	45
Figure 3.41. Normalized Detector Responses on the Torso of the Anthropomorphic Phantom for beam with 5 MeV Neutron Beam and with PA Incidence.....	46
Figure 3.42. Normalized Detector Responses on the Torso of the Anthropomorphic Phantom for beam with a ^{235}U Watt-Spectrum and with PA Incidence.....	46
Figure 3.43. Normalized Detector Responses on the Torso of the Anthropomorphic Phantom for beam with a ^{235}U Maxwellian Energy Spectrum and with PA Incidence.....	47
Figure 4.1. Peak with a Base Line to Calculate the Net Counts under the Full-Energy Peak (Spectrum: NE 799 HW).....	50
Figure 4.2. Mixed Source Spectrum.....	52

Figure 4.3. Double Peaks of the Mixed Source Spectrum at Energies, 121.2 (Eu 152) &123.13 (Eu 154) and 244 (Eu 152) & 248 ((Eu 154) (expand window).....	52
Figure 4.4. Double Peaks of the Mixed Source Spectrum at Energies 996.6 keV (Eu 154) and 1004.8 keV (Eu 154) (expand window).....	53
Figure 4.5. Efficiency vs. Energy Curve.....	54
Figure 4.6. TLD Reader Block Diagram.	66
Figure 4.7. Calibration Curve for TLD-600.....	68
Figure 4.8. Calibration Curve for TLD-700.....	68
Figure 4.9. The value of $k = \frac{R'_{600}}{R'_{700}}$ at Various Distances from the Source.	69
Figure 4.10. Block Diagram of Dosimeter Package.	71
Figure 4.11. Semiconductor-Based Neutron Dosimeter Experiment in the Beam Port. ..	73
Figure 4.12. Semiconductor-Based Neutron Dosimeter Placed in the Middle of Harry. ..	73

List of Tables

Table 2.1. Reactions for Detecting Slow Neutrons.....	5
Table 2.2. Values of the Quality Factor for Different Radiations [ICRP, 1991; NCRP 1993].	11
Table 2.3. Average Soft Tissue Elemental Composition of the ICRU Sphere.....	13
Table 2.4. Specifications of Adult Male Computational Model [ICRU, 1992].....	14
Table 2.5. The Dimensions of the Torso Phantom are as follows [Data Spectrum, 1995].	15
Table 3.1. Normalization Constant for Seven Cases of Neutron Sources Considered Irradiating the Phantom.....	22
Table 3.2. F4 Tally Multiplicative Constant.	23
Table 3.3. <i>SDC</i> for Various Neutron Energy Spectra.....	36
Table 4.1. Contents of the Mixed Source, Half-Lives, Decay Constants, Activities on Calibration Date and on Experiment Date.....	51
Table 4.2. The Mass, Thickness, Diameter, Irradiation Time, Wait Time and Count Time for Bare and Cd-covered Gold Foils.....	63
Table 4.3. Properties of TLD-600, TLD-700 used in the Experiment.....	65
Table 4.4. Bare TLD Responses on the Surface of Harry.	70
Table 4.5. Cd-filtered TLD Responses on the Surface of Harry.	70
Table 4.6. Dosimeter Counts, Dosimeter Display Facing Beam Port and Dosimeter Display Facing Back to Beam Port.....	72
Table 4.7. Bare and Cd-filtered SND Responses on Harry.	74
Table 4.8. Bare (N_b) and Cd-filtered (N_{Cd}) SND Counts on Harry, the Corresponding Dose and Count-to-Dose Conversion Factor.....	76
Table 4.9. The Count-to-dose Conversion Factors and the Corresponding Standard Deviations	76

Table - C.1. Emitting Isotopes of the Mixed Source and the Total Number of Radiation Quanta Emitted from Each Isotope.....	98
Table - C.2. Identified Energy from the Mixed Source Spectrum, Corresponding Emitting Isotope, Total Counts under Each Peak, Intensity and Calculated Efficiency.....	99
Table - D.1. Area Under the 411.8 keV Peak of the Irradiated Gold Foils.	100
Table - E.1. Source Reference Date, Experiment Date, Elapsed Time and Activity on Experiment Date.	109
Table - E.2. Calculated Dose Rates for TLD-700 Dosimeters at Different Distances from the Source.....	110
Table - E.3. Calculated Dose Rate for TLD-600 Dosimeters at Different Distances from the Source.....	110

Acknowledgements

I express my sincere gratitude to Dr. William L. Dunn for his valuable guidance and advice in the conduct of this research project. I am also very much thankful to him for his invaluable support and continued cooperation to complete the project and towards my future goals. I would like to thank Dr. J. Kenneth Shultis, who provided valuable suggestions during the study. I would also like to thank the members of the KSU SMART Laboratory: Dr. Douglas McGregor, Eric Patterson and Walter McNeil for their cordial help and support. I am grateful to reactor manager Mike Whaley and other colleagues for their support during the project. I would also like to thank Edgar Martinez for his help during my experimental study. I would also like to acknowledge my parents and my other family members and my husband who inspired me all the time towards my career goal.

I would also like to acknowledge my appreciation to the US Department of Energy for the funding of this research project.

Dedication

Dedicated to my husband ASM Sabbir Ahmed, without his help and cooperation I will not be able to complete the thesis and to my lovely little boy Bihan who has to sacrifice his mom's care for a while.

1 Introduction

Neutrons are uncharged atomic particles that can penetrate matter including living tissue. Neutron radiation is encountered in the nuclear fuel cycle, in nuclear power generation, in medical and research accelerators, and as a result of cosmic radiation. Because neutrons interact with nuclei and produce secondary ionizing radiation they can cause damage in humans, including nerve damage, cataracts, and cancer. Neutron radiation can also affect the blood-forming marrow in bones of humans and other animals. Neutron dosimeters are used to measure doses due to neutrons. However, at the present time, no efficient and convenient portable neutron dosimeters are readily available.

Personal dosimeters are worn on the body and therefore the backscattered radiation from the body has an effect on the detector responses [ICRU, 2001]. An anthropomorphic phantom is useful to characterize neutron detectors for use as personal dosimeters. This research is concerned with characterization of perforated semiconductor neutron detectors used in small self-powered packages to serve as neutron dosimeters. These will have low cost, photon insensitivity, and small size. Neutron personal dosimeters should be responsive over a broad energy range (0 – 15 MeV).

The most commonly used neutron dosimeters are the ‘albedo neutron dosimeter’, the tissue equivalent proportional counter, the bubble dosimeter, the etch-track dosimeter, the semiconductor-based neutron dosimeter, and the Bonner sphere. The disadvantages of albedo neutron dosimeters are strong energy dependence, high photon sensitivity, and low detection limit. Tissue-equivalent proportional counters consume high power and are costly to fabricate. A disadvantage of bubble dosimeters is that the detector response varies from detector to detector [Schwartz and Hunt (1990) and Chemtob and et. al. (1995)]. A difficulty of etch-track dosimeters is that the sensitivity of the detector material polyallyl diglycol carbonate (PADC) varies from batch to batch. The main disadvantage of Bonner spheres is that they are bulky to use for personal neutron dosimetry.

Therefore a great need exists for high efficiency, real time, room-temperature, low power personal neutron dosimeters that are gamma insensitive. Present designs of semiconductor neutron detectors achieve maximum thermal neutron detection efficiency of only 4% when operated with an energy threshold of 300 keV. The proposed semiconductor detector to be used for neutron dosimetry increases the thermal neutron detection efficiency to above 20%. The detectors are packaged in small rugged containers to be worn as active dosimetry badges that can be read in real time. These detectors will have a dramatic impact. For example, homeland security, treaty verification, personal neutron dosimetry, and neutron survey instrumentation will all greatly benefit from such neutron detectors.

In the design investigated, silicon semiconductor materials are perforated using plasma-etching techniques and the surface is coated and the perforations are filled with neutron reactive material (^{10}B or ^6LiF). Neutrons interact in the reactive material and produce detectable reaction products from either the $^{10}\text{B}(n, \alpha)^7\text{Li}$ or the $^6\text{LiF}(n, t)^4\text{He}$ reactions. These devices are insensitive to gamma rays and therefore provide a good neutron to gamma-ray detection ratio. These perforated semiconductor detectors appear to be capable of greater than 50% efficiency when used in a sandwich design. Devices incorporating bare and cadmium-filtered perforated detectors with a low-power operational amplifier, discriminator, and counter/display are able to process and read out the detectors and also are small enough to function as portable neutron dosimeters. The devices will be able to detect thermal and epithermal neutrons and relate the response to neutron dose.

The purpose of this research study is to characterize portable neutron dosimeter devices that incorporate these new highly efficient, low-noise, and real time semiconductor neutron detectors. The device tested experimentally contained one detector but dosimeter packages containing two detectors, one with a cadmium (Cd) filter to eliminate back-scattered thermal neutrons (filtered detector) and one without Cd to accept neutrons of all energies (bare detector) [Jahan and others, 2007] are possible. The dosimeter provides real-time readout of detector response in counts. The dose corresponding to a measured set of detector responses was estimated using a TLD pair of TLD 600 and TLD 700 thermoluminescence dosimeters (TLDs) First the calibration

curve for the TLD 600 and TLD 700 dosimeter was determined using a source with known strength and then the same pair of TLDs was placed on the phantom and irradiated. Then using the calibration curve, the neutron dose was determined (detailed description in section 4.2). An anthropomorphic torso phantom was used to simulate the effect of the human body [Section 3.4.].

The characterization procedure was performed in two parts: i) simulation and ii) experiment. The Monte Carlo N-particle (MCNP) Transport Code [Breisemeister, 2000] was used to model the response of the detectors placed near the phantom for various neutron beams. The characterization of these dosimeters along with the phantoms was performed for a parallel beam having a thermal Maxwellian distribution, a Watt distribution for ^{235}U fission neutrons, or monoenergetic neutrons. For the experimental study, the Kansas State University TRIGA Mark II Nuclear Reactor was used as a source of thermal and epithermal neutrons. Finally the model and the experimental results were compared.

2 Background

This review considers the different topics of neutron detectors, neutron dosimeters, dosimetric quantities, fluence-to-dose conversion, and dosimetric phantoms.

2.1 Neutron Detectors

Neutrons are uncharged particles that indirectly ionize material. Therefore neutrons are detected through the secondary particles resulting from nuclear interactions. A detection system can detect neutrons by observing: (i) the recoil nucleus from an elastic or inelastic scattering collision between a neutron and an atomic nucleus, (ii) energetic protons, alpha particles, or other ions that are released from the absorption of neutrons, or (iii) gamma rays that are released due to capture of inelastic scattering [NCRP, 1971].

Therefore, to be detected, neutrons have to cause a nuclear reaction that produces secondary particles. The kinetic energy of the secondary particles depends on the energy of the primary particles and the type of interactions. The neutron cross section can be a strong function of energy; therefore detection of neutrons is different in different energy regions. Due to this energy dependence the detection of neutrons typically is divided into two groups a) slow (low energy $< 0.5\text{eV}$) neutron detection and b) fast (high energy $> 0.5\text{eV}$) neutron detection.

2.1.1 Cadmium Cutoff

The response of a bare neutron detector, C_{bare} is due to a combination of slow and fast neutrons. Covering a detector with cadmium will effectively block out the thermal neutrons and the counts from these detectors are called filtered counts, $C_{filtered}$. Then it is possible to approximately determine the count, C_{th} , only for the thermal neutrons from

$$C_{th} = C_{bare} - C_{filtered} . \quad (2.1)$$

2.1.2 Slow Neutron Detection

Neutrons whose energies are below the cadmium cut-off are conventionally called slow neutrons [Knoll, 2000]. Several factors must be considered for the detection of neutrons: i) the cross section for the reaction (which should be as large as possible so that efficient detectors can be built with small dimensions), ii) the abundance of the target nuclide, iii) the Q -value of the reaction (which determines the energy liberated in the reaction following neutron capture), and iv) the range of the reaction products (since the size of the active volume of the detector depends on the range of the reaction products [Knoll, 2000]). The higher the Q -value, the higher the energy of the reaction products and the easier it is to discriminate the gamma-ray events by simply using amplitude discrimination. Typical values of relevant quantities for three reactions used to detect slow neutrons are given in Table 2.1.

Table 2.1. Reactions for Detecting Slow Neutrons.

Reaction	Q (MeV)	Thermal neutron cross section σ (barn)
${}^3\text{He}(n, p) {}^3\text{H}$	0.76	5330
${}^6\text{Li}(n, t) {}^4\text{He}$	4.78	940
${}^{10}\text{B}(n, \alpha) {}^7\text{Li}$	2.79	3840

2.1.3 Fast Neutron Detection

Fast neutrons can be detected from the recoil nuclei that are produced by elastic neutron scattering. Fast neutrons also can be detected by utilizing moderation (a process in which a neutron loses much of its kinetic energy), followed by the detection of low-energy neutrons. A neutron can transfer almost all of its energy in a single collision with light nuclei whereas only a small fraction can be transferred in a collision with heavy nuclei. Thus hydrogenous materials such as water, polyethylene, and paraffin often are used for neutron thermalization.

2.2 Neutron Dosimeters

Measuring radiation dose in a radiation environment is very important and for this reason different types of instruments called dosimeters or dosimeters are used [Eichholz and Poston, 1979]. Because interaction of neutrons inside the body produces photons

(e.g. capture of neutrons in hydrogen produces 2.223 MeV photons), an ideal neutron dosimeter should be photon insensitive and discrimination against photons in neutron dosimetry is very important [ICRU, 2001]. There are different approaches for different types of devices; for electronic devices that produce pulse height spectra, discrimination of photons may be possible by setting an electronic threshold above the height of pulses generated by photons. In some devices one element is chosen that is sensitive to both neutrons and photons and a second element is chosen that is sensitive to photons only. The difference between the signals can be used to estimate the neutron dose. Some other detectors, for example etch-track detectors and tissue equivalent proportional counters, are neutron sensitive only.

Neutron dosimeters can be divided into the following two groups:

- 1) Active neutron dosimeters, in which data are collected and displayed automatically. Real time data acquisition and good gamma ray discrimination are the main advantages of active dosimeters.
- 2) Passive neutron dosimeters, in which neutron interactions in the detectors induce some, charge that is measured later. In these types of dosimeters, data are recorded in the detector, which is then processed in the laboratory. Passive dosimeters provide delayed information and processing can be delayed from a few hours to several months. However passive dosimeters have some advantages over active dosimeters, such as lower unit cost.

In the following sections the basic working principles, advantages, and disadvantage of some of the present neutron dosimeters are discussed.

2.2.1 Active Dosimeters

Active dosimeters include gas counter and semiconductor detectors. Some of the active dosimeter devices are discussed in the following sections.

2.2.1.1 Tissue-Equivalent Proportional Counters (TEPC)

A TEPC is usually designed with a spherical or cylindrical cavity chamber of a few centimetres in diameter containing a central anode wire. These counters are operated with a tissue equivalent wall (A-150 tissue equivalent plastic) and filled with tissue-

equivalent gas [ICRU, 2001]. The problems associated with these counters are high power consumption and high fabrication cost.

2.2.1.2 Semiconductor Based Neutron Dosimeters

In semiconductor detectors, the charged particles produced by neutrons are detected by the detector itself or can also be detected by some special types of converter layers which are mounted very close to the detectors [ICRU, 2001]. Silicon, diamond, germanium, CdZnTe and GaAs are the most commonly used semiconductor materials and Boron-10 (^{10}B) and lithium-6 fluoride (^6LiF) are used as neutron reactive materials. These detectors are used to detect both thermal and epithermal neutrons.

A thin-film coated detector usually consists of a semiconductor diode coated with either ^{10}B or ^6LiF . A neutron interacts in the film and produces charged particles via the reactions $^{10}\text{B}(n, \alpha)^7\text{Li}$ or $^6\text{LiF}(n, t)^4\text{He}$. Some of these charged particles are transported into the semiconductor. The measured voltage signal is directly proportional to the number of electron hole pairs excited within the semiconductor. The energy of the charged particles produced in these reactions is relatively large and the produced signals are easily discernable from gamma-ray background. Coated semiconductor detectors offer the advantage of low power consumption and compact size; hence they are ideal for active “real-time” dosimeters. Such devices are limited to approximately 4% thermal neutron detection efficiency for both ^6LiF and ^{10}B single coated devices. Double-coated devices can achieve 8% thermal neutron detection efficiency [McGregor et al. 2003].

2.2.1.3 Bonner Sphere (Moderating Detector)

Monitoring of neutron fields is often performed with moderator-type dose-equivalent meters, which are also known as remmeters. Bonner spheres are the most commonly used moderating detectors. A Bonner Sphere Spectrometer (BSS) consists of a thermal neutron detector and moderating materials in the form of polyethylene spheres of various sizes in diameter, usually ranging from 5.1 to 45.7 cm. Increasing the amount of moderator causes higher energy incident neutrons to be thermalized before reaching the detector and attenuates lower energy incident neutrons by absorption. A variety of thermal neutron detectors may be used with a BSS. The Bonner sphere of 25 cm diameter approximates the dose responses of energies up to 5 MeV [Eichholz and Poston, 1979].

The Bonner balls are usually bulky (e.g. a 12-inch sphere weighs 15 kg) and therefore inconvenient to use for portable neutron dosimetry [ICRU, 2001].

2.2.2 *Passive Dosimeters*

Some examples of passive dosimeters are discussed in the following sections.

2.2.2.1 *Albedo Neutron Dosimeters (or Thermoluminescent Dosimeters)*

Thermoluminescent dosimeters (TLDs) are used in albedo neutron dosimeters. In TLDs, the ionization energy is absorbed in the thermoluminescent (TL) material and a portion of that energy causes electrons to become trapped. The number of trapped electrons is directly proportional to the incident radiation. The TL material is heated at a controlled rate to release the trapped electrons. The electrons escape from the traps and return to a lower energy state by releasing photons of visible light. The human body absorbs and scatters neutrons, which greatly influences the neutron dose [Barlett et al, 1999]. The basic principle of this detector is to detect low energy neutrons reflected from the body; for this reason it is known as the ‘albedo neutron dosimeter’. This dosimeter consists of detectors with natural and enriched abundances of ^6Li . These detectors can be covered by a layer of cadmium to absorb the very slow moving neutrons. These detectors have high detection sensitivity below 100 keV regions [Ing and Piesch, 1985]. Their main shortcomings are strong energy dependence; high photon sensitivity and lower detection limit [ICRU, 2001].

2.2.2.2 *Etch-Track Dosimeter*

The basic principle of etch-track dosimeters is that tracks are produced in the detector medium due to the neutron interactions [Ing and Piesch, 1985]. Caustic solutions are used to reveal the tracks and an electron microscope is used to view the tracks. For neutron dosimetry, the most commonly used etch track detector is polyallyl diglycol carbonate (PADC), which is also known as the CR-39.

Most commercially available etch track dosimeters can detect fast and thermal neutrons. The fast neutron dose is measured by counting the proton recoil tracks and the thermal neutron dose is measured by counting the alpha tracks produced in the PADC [ICRU, 1985]. The shortcoming of this detector as a neutron dosimeter is that the

performance of PADC in sensitivity varies from batch-to-batch and also sheet-to-sheet [ICRU, 2001]. Fading and ageing of the plastic are also great disadvantages of the detector of this dosimeter.

2.2.2.3 Bubble Dosimeters

Bubble dosimeters are also known as superheated-emulsion neutron dosimeters. These dosimeters consist of small droplets of a superheated liquid (i.e. a liquid at a temperature above its normal boiling point) scattered (dispersed) in a gel or in an elastic polymer. The interaction of neutrons with a nucleus inside or near the droplets produces secondary charged particles, which transfer energy to the droplet. As a result, the droplets vaporize and burst out into a noticeable bubble. The resulting bubbles are trapped in the visco-elastic medium. The production of bubbles is directly proportional to the incident neutron dose. The commercially available bubble dosimeters have a sensitivity of 5 bubbles per millirem [Cember, 1983]. The maximum number of bubbles that can be counted determines the maximum dose that can be measured. This dosimeter is reset by re-pressurization. These dosimeters are not widely used due to difficulties with reliability and durability [ICRU, 2001].

2.3 Radiation Quality and Dose Equivalent

The hazard due to exposure to ionizing radiation depends on both the exposure and its duration. Dosimetric quantities provide physical measurements of radiation effect at a point of interest. The biological hazard due to radiation results from the deposition of energy, ionization of the medium, and introduction of atomic displacements. The fundamental dosimetric quantities are absorbed dose, quality factors, and dose equivalent. These quantities are described in the following sections.

Neutrons are moderated, scattered, and captured inside the body or the phantom and all these processes have a great influence on neutron dose and hence the dosimeter reading [Barlett, et al., 1999]. There are two international organizations for developing dosimetric convention and assessing radiation doses from external radiation exposures and from intakes of radionuclides. The two international organizations are:

The International Commission on Radiation Units and Measurements (ICRU), at 7910 Woodmont Avenue, Suite 800, Bethesda, MD 20814-3095,

which issues international shielding and dosimetry guidelines and recommendations, and The International Commission on Radiological Protection (ICRP), SE-171 16 Stockholm, Sweden, which publishes international shielding, and radiological guidelines and recommendations.

Another organization, which issues various guidelines for the United States is, The National Council on Radiation Protection and Measurements (NCRP), at 7910 Woodmont Avenue, Suite 800, Bethesda, MD 20814-3095. In 1925, The International Congress of Radiology established the ICRU. The principal objective of ICRU was to develop internationally acceptable recommendations regarding the quantities and units of radiation. The ICRU also determines the measurements and application of these quantities in diagnostic radiology, radiation therapy, radiation biology, and industrial operations [Peurrung, 2000]. The ICRP is an independent Registered Charity, which is recognized for the protection of the public from radiation.

2.3.1 Absorbed Dose

Absorbed dose is a fundamental dosimetric quantity for radiological protection. Absorbed dose D is defined as the amount of energy absorbed per unit mass. The standard unit of absorbed dose is the gray (Gy) and is equal to an imparted energy of 1 joule per kilogram [Shultis and Faw, 2002]. The traditional unit of the absorbed dose is the rad and is defined as 100 ergs per gram. Therefore $1 \text{ rad} = 0.01 \text{ Gy}$.

2.3.2 Quality Factor and Linear Energy Transfer (LET)

Quality factor is a weighting factor that depends on the type and energy of radiation. The quality factor for photons and electrons of any energy is equal to 1. For neutrons the quality factor depends on their energy. The quality factor for a charged depends on its stopping power, which is also known as the linear energy transfer or LET. The LET is denoted as the expected energy loss per unit distance of travel by the charged particle. Typical values of the quality factors in terms of different radiations are given in Table 2.2 [Shultis and Faw, 2002].

**Table 2.2. Values of the Quality Factor for Different Radiations
[ICRP, 1991; NCRP 1993].**

Radiation	QF
X, γ , β^\pm , (all energies)	1
Neutrons < 10 KeV	5
10 – 100 KeV	10
0.1- 2 MeV	20
2 – 20 MeV	10
> 20 MeV	5
Protons (> 1 MeV) [ICRP]	5
Protons (> 1MeV) [NCRP]	2
Alpha Particles	20

2.3.3 Dose Equivalent

Dose equivalent, H is a measure of radiation risk and is the product of absorbed dose (D) and quality factor (QF) at a point in tissue i.e,

$$H = D(QF), \quad (2.2)$$

The standard unit of dose equivalent is the Sievert (Sv) and the traditional unit of dose equivalent is the rem where 1 rem = 0.01 Sv.

2.3.4 Operational Dose Quantities

The operational dose quantities are the radiation protection measurement quantities recommended by ICRP, which are also point functions (determined by the radiation field in the vicinity of a point in space). Phantoms are used for the calibration of personal dosimetry. For dosimetry of the trunk, the appropriate depth in the phantom for strongly penetrating radiation is 10 mm and for skin is 0.07 mm [ICRU, 2001]. The operational quantities for whole-body irradiations with neutrons are expressed with the ambient dose equivalent, $H^*(10)$, and the personal dose equivalent, $H_p(10)$ [ICRU, 2001].

2.3.5 Ambient Dose Equivalent

For area monitoring, ICRU recommends the use of the quantity ambient dose equivalent, with the symbol $H^*(10)$. This quantity is defined in a very simple phantom,

the ICRU sphere, by the dose equivalent at 10 mm depth, and provides unique calibration conditions for area dosimeters (area monitors and survey instruments) [ICRU, 2001].

2.3.6 Personnel Dose Equivalent

Personnel dose equivalent $H_p(d)$ is the dose equivalent at a depth d in soft tissue for penetrating radiation. The suggested depth is 10 mm for strongly penetrating radiation and $H_p(d)$ is written as $H_p(10)$. For weakly penetrating radiation the depth d is 0.07 mm for the skin and 3 mm for the lens of the eye.

Because personal neutron dosimeters are worn on the body, they should be calibrated on an anthropomorphic phantom and the calibration quantity is the personal dose equivalent at 10 mm depth, $H_p(10)$.

2.4 Fluence-to-Dose Conversion

The fluence-to-dose conversion coefficient is used to establish the relationship between measurable quantities and operational quantities. The fluence-to-dose equivalent conversion coefficients are also known as the response function, which is the dose or response per unit neutron fluence [Shultis and Faw, 2000]. The operational dose equivalent quantities are determined using the equation [ICRU, 2001]

$$H = \int \mathfrak{R}(E)\phi(E)dE, \quad (2.3)$$

where H is ambient or personal dose equivalent, $\mathfrak{R}(E)$ is the corresponding energy dependent fluence-to-dose equivalent conversion coefficient, and ϕ_E is the energy distribution of the neutron fluence [ICRU, 2001].

2.5 Phantoms

A phantom is a structure that contains tissue equivalent substances and is used to simulate radiation interactions in the body [Attix et. at. 1996]. Phantoms are widely used in radiation dosimetry, radiotherapy, nuclear medicine, radiation protection and in the calibration of radiation detection systems. There are three different types of phantoms available: 1) dosimetric phantom, 2) calibration phantom, and 3) imaging phantom. A dosimetric phantom is used for the measurement of absorbed dose in a specified

geometry, a calibration phantom is used for establishing the response of radiation detectors, and an imaging phantom is used for the assessment of radiation quality [ICRU, 1992].

2.5.1 Reference Computational Model (or ICRU sphere)

Simple mathematical models like slabs, cylinders, or spheres are used to estimate dose equivalents from different types of radiation [ICRP, 1987]. The most commonly used model is the reference computational model, which is also known as the ICRU sphere; this sphere is 30 cm in diameter and simulates the composition of soft tissue [ICRU, 1992]. The ICRU sphere, depicted in Figure 2.1, has a mass of 14.14 kg and a density of 1000 kg m^{-3} . The composition of the ICRU sphere is described in Table 2.3.

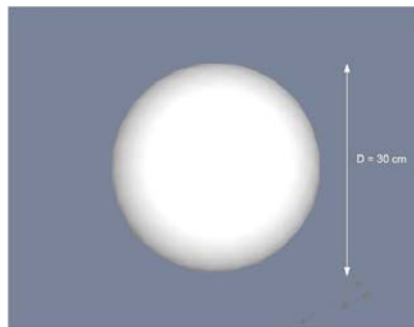


Figure 2.1. The ICRU Sphere.

Table 2.3. Average Soft Tissue Elemental Composition of the ICRU Sphere.

Element	Mass percent
H	10.1
C	11.1
N	2.6
O	76.2

2.5.2 Computational Anthropomorphic Phantom

A computational anthropomorphic phantom is a mathematical description of the human body, which uses mathematical expressions to represent plane, cylindrical, elliptical or spherical surfaces to represent different body organs [ICRU, 1992]. These phantoms are widely used for numerical simulation of the transport of radiation throughout the body.

The specifications of the adult male computational model are described in Table 2.4. The heights and masses of the whole body, as well as the masses of the internal organs are based on the ICRP Reference Man data [ICRP, 1975].

Table 2.4. Specifications of Adult Male Computational Model [ICRU, 1992].

Physical Dimension	Values	Body Tissues	Mass Density (kg m ⁻³)
Mass (Kg)	69.9	Soft Tissue	987
Height (cm)	170	Lung	296
Trunks + arms (cm)	40.0	Whole Skeleton	1486
Trunk (cm)	20.0	Skin	1105

The response functions are calculated for mono-energetic radiation incident on the phantom in a fixed geometry. The most commonly used geometries are [ICRP 1987]: Anterior Posterior (AP): irradiation from the front to the back of the phantom with the beam at right angles to the long axis of the body. Posterior Anterior (PA): irradiation from the back to the front of the phantom with the beam at right angles to the long axis of the body. Lateral (LAT): a parallel beam of particles impinging on the side of the phantom. There are two types of lateral beam RLAT (irradiated from right) and LLAT (irradiated from left). Rotational (ROT): a rotating plane parallel beam. The ROT is considered to be the perfect choice for a person moving with respect to a radiation source. Isotropic (ISO): an isotropic radiation field [Shultis and Faw, 2000].

2.5.3 Phantom Used for Detector Characterization

The anthropomorphic torso phantom from Biodex Medical was used for the characterization of the neutron dosimeter in the present study. The phantom is made of polymethyl methacrylate (PMMA), which is an organic compound and also known as Plexiglas or Lucite. The density of PMMA is 1.19 g cm⁻³ and its composition by weight is 8.05% hydrogen, 31.96% oxygen and 59.99% carbon [ICRU, 1984]. The density of the phantom is close to that of tissue, but the composition is somewhat different in that there is no nitrogen in the phantom. The phantom consists of a large, body-shaped cylinder with lung, liver, and spine inserts. The phantom simulates the anatomical structures of the upper torso of average to large male/female patients. Lung inserts can be filled with

Styrofoam beads and water to simulate lung tissue density. The phantom is shown in Figure 2.2 and the dimensions of the torso are given in Table 2.5.

**Table 2.5. The Dimensions of the Torso Phantom are as follows
[Data Spectrum, 1995].**

	Dimension (cm)
Lateral outside	38
Lateral inside	36
Anterior-posterior outside	26
Anterior-posterior inside	24
Wall thickness	0.92

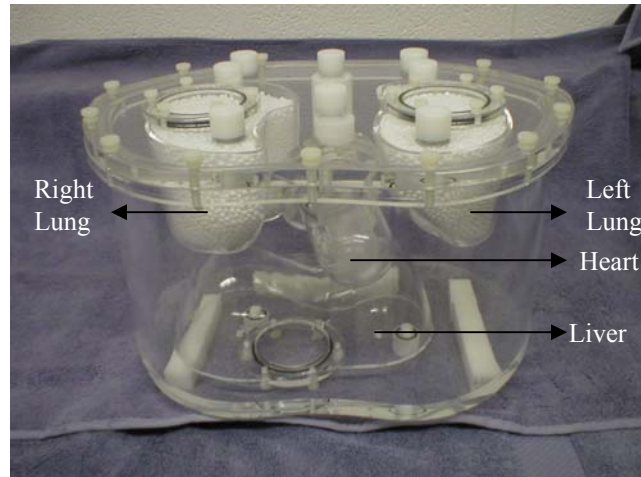
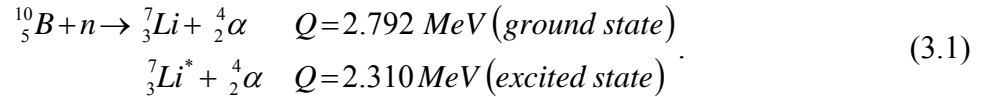


Figure 2.2. Anthropomorphic Torso Phantom, Used for the Present Study.

3 Monte Carlo Study for Characterization of Semiconductor Neutron Dosimeters

3.1 Theoretical Consideration of the Detector

A popular method to detect thermal neutrons using semiconductor detectors is to coat the semiconductor with a thin layer of neutron reactive material. The most commonly used semiconductor materials include bulk Si, GaAs, diamond and amorphous Si [Gersch, 2001]. Pure ^{10}B and ^6LiF are neutron reactive materials that are often used to coat semiconductors for the detection of neutrons. The $^{10}\text{B}(n, \alpha)^7\text{Li}$ reaction can be expressed as [Knoll, 2000],



The ^7Li reaction product in this reaction indicate is in the first excited state 93.7% of the time and de-excites to the ground state by releasing a 480 keV gamma-ray. The other 6.3% of the time ^7Li appears in the ground state.

The $^6\text{LiF}(n, {}^3\text{H})^4\text{He}$ reaction can be expressed as,



In both cases, the two reaction products are emitted in opposite directions. The microscopic absorption cross section of ^{10}B is 3,840 b at thermal energy (0.0253 eV) and decreases with increasing energy as the inverse of the neutron speed over a significant energy range [McLane, Dunford and Rose, 1988]. For ^6Li the absorption cross section at thermal energy is 940 b and varies approximately as $1/v$, where v is the neutron speed, except at certain resonances including one in which the absorption cross section surpasses that of ^{10}B for energies between approximately 150 keV and 300 keV [McLane, Dunford and Rose, 1988]. The absorption cross-sections for ^{10}B and ^6Li with respect to energy are shown in Figure 3.1. These data were generated using MCNP4C neutron cross-section library [Breisemeister, 2000].

Due to the higher thermal absorption cross-section, the $^{10}\text{B}(n, \alpha)^7\text{Li}$ reaction leads to higher reaction probability than the $^6\text{LiF}(n, {}^3\text{H})^4\text{He}$ for neutron energies below

100 keV. However the higher energy reaction products emitted from the ${}^6\text{Li}(n, {}^3\text{H}) {}^4\text{He}$ reaction are easier to detect than the particles emitted from the ${}^{10}\text{B}(n, \alpha){}^7\text{Li}$ reaction.

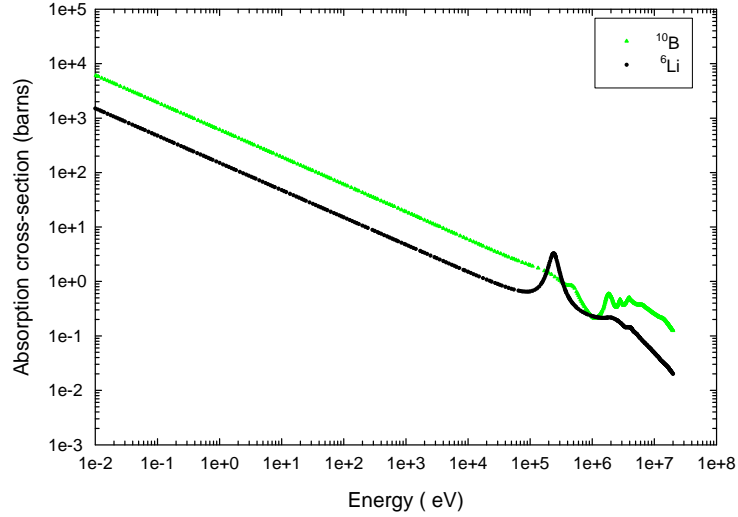


Figure 3.1. Comparison of Neutron Cross Sections for ${}^{10}\text{B}$ and ${}^6\text{Li}$ material.

3.2 Model Geometry for the Neutron Detector

Each detector was designed by utilizing a cavity structure in which deep holes are etched into the diode surface and the holes are filled with neutron reactive material [McGregor et. al. 2002]. This design increases the surface area of the device and produces a greater probability of ejecting a reaction product into the semiconductor substrate. The ${}^{10}\text{B}$ material was selected as the neutron reactive material for the detection of the thermal neutrons in the simulation study. The semiconductor material for the detector was considered as Si for its two important properties: i) the neutron cross-section for silicon is 0.16 barns, which indicates that the neutron has almost no interaction in the detector active region [McGregor et. al. 2001] and ii) the low atomic number of Si, which leads to a low absorption probability for gamma rays [Gersch, 2001]. Therefore the model assumes that neutrons interact only with the ${}^{10}\text{B}$ material and the charged particles produced are responsible for the creation of electron hole pairs in the detector active region. The MCNP Monte Carlo simulation code was used to estimate the detector responses when the detector was placed in front of a water phantom. An example code for the water phantom model is attached in Appendix A. For simplicity of the model it

was assumed that the ^{10}B material was uniformly distributed throughout the semiconductor with 70% coverage. The actual detector has neutron reactive material filling cylindrical perforations (see Figure 3.2) and covering the top of the detector. It was also assumed that the boron in the detector was enriched to 50%. Therefore the atom density, N_{10} of the ^{10}B material was adjusted for 70% coverage and for 50% enrichment,

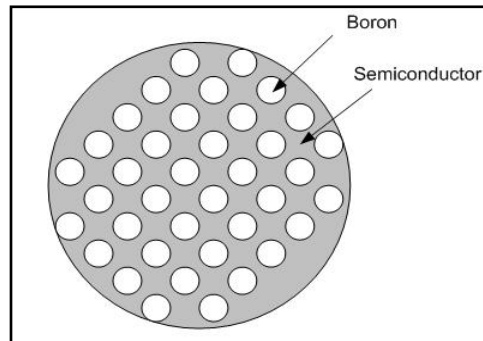


Figure 3.2. 70% Coverage of ^{10}B Material in the Si Semiconductor Substrate (Top View of a Detector).

as shown in Appendix B, the adjusted atom density was $N_{10} = 0.04620 \text{ atoms (b-cm)}^{-1}$.

The efficiency of this neutron detector depends on the probability of interactions of neutrons with the boron atoms and also on the probability of the detection of the emitted charged particles into the semiconductor substrate. In this model, it was assumed that the efficiency of detecting the charged particle is 100%. The model results can then be scaled according to the actual efficiency of the built detector.

The neutron dosimeter incorporated two neutron detectors: one with a Cd filter to eliminate thermal neutrons (filtered detector) and one bare, which is able to detect neutrons of all energies. Both the detectors were modeled as cylindrical disks of diameter 1 cm and thickness of 0.005 cm. The filtered detector had a 30 μm layer of cadmium behind it (between the detector disk and the phantom).

3.3 Model Geometry for Water Phantom

The detector responses were first calculated for a simple water phantom, which mimics a human torso as the human body is made of 60-75% water, and then the model was applied to the more complicated anthropomorphic phantom. The size of the water

phantom was chosen to be typical of a standard male torso with height along the z -axis of 70 cm and major (x -axis) and minor (y -axis) axis dimensions of 40 cm and 20 cm, respectively. The two detectors were used as a pair and the centers of the detectors were separated vertically by 2 cm. A total of eight pairs of detectors (eight dosimeters) were placed in front of the water phantom. In the water phantom the four dosimeters were placed on the front surface of the phantom at $x = 0$ cm, $y = 10$ cm, and at vertical positions $z = 0, 10, 20$ and 30 cm, where $z = 0$ cm is the mid-height of the phantom. The other four dosimeters were placed at $x = 10$ cm, $y = 8.66$ cm and rotated by 16.1° so as to be tangent to the phantom and at the same vertical positions. A three-dimensional (3-D) view of the positions of the detectors on the cylindrical water phantom is shown schematically in Figure 3.3. The detailed description of the separation of each detector in a two-dimensional (2-D) view is shown in Figure 3.4.

A parallel beam of neutrons 40 cm wide and 70 cm high was used to irradiate the water phantom in the AP manner. A 2-D view of the parallel beam and the water phantom and one pair of the detectors at $z = 0$ cm position is shown in Figure 3.5, where D1 is the bare detector and D2 is the filtered detector.

3.3.1 Normalization Constants

The detector responses were normalized for a beam that would produce 1mSv ambient dose equivalent if incident on the ICRU sphere phantom; this is $1/50^{\text{th}}$ of the annual occupational exposure limit recommended by the National Council on Radiation Protection and Measurements [NCRP 1987] for stochastic effects. A neutron beam will produce a dose equivalent in the ICRU sphere of

$$H = \int_0^\infty \mathfrak{R}(E)\Phi(E)dE, \quad (3.3)$$

where $\mathfrak{R}(E)$ is the neutron ambient dose equivalent response function [ICRU, 2001], and for the parallel beam

$$\Phi(E) = S_a \chi(E), \quad (3.4)$$

where S_a is the beam intensity per unit area and $\chi(E)$ the probability density function for neutron energy. Thus

$$H = S_a I, \quad (3.5)$$

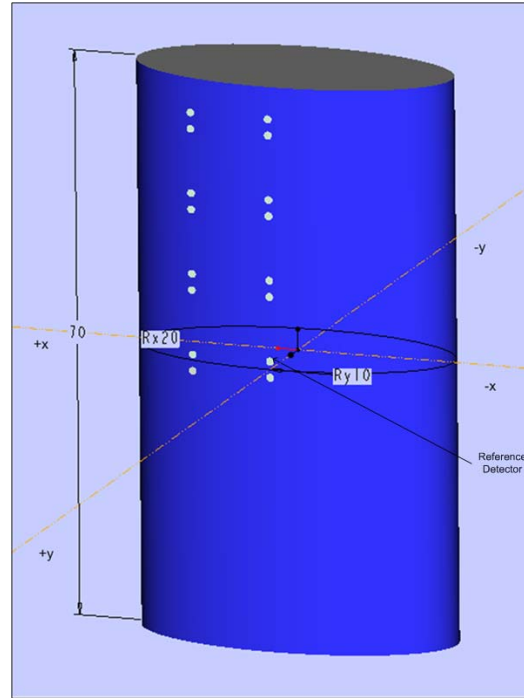


Figure 3.3. Water Phantom with the Positions of Eight Pairs of Detectors (3-D view).

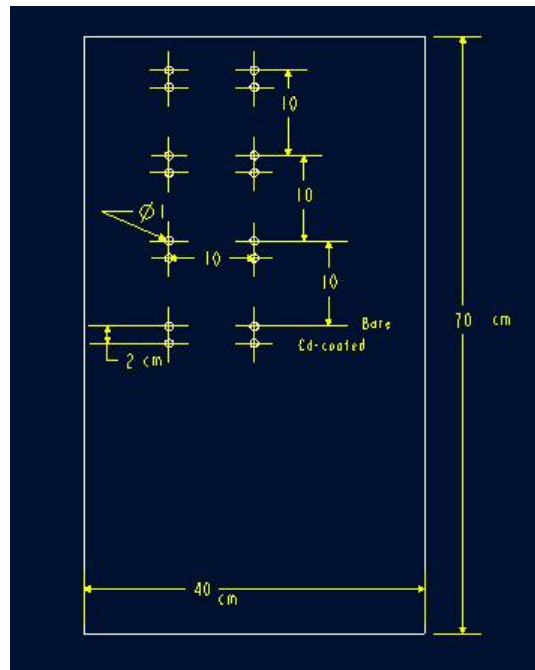


Figure 3.4. Water Phantom with the Positions of Eight Pairs of Detectors (2-D view).

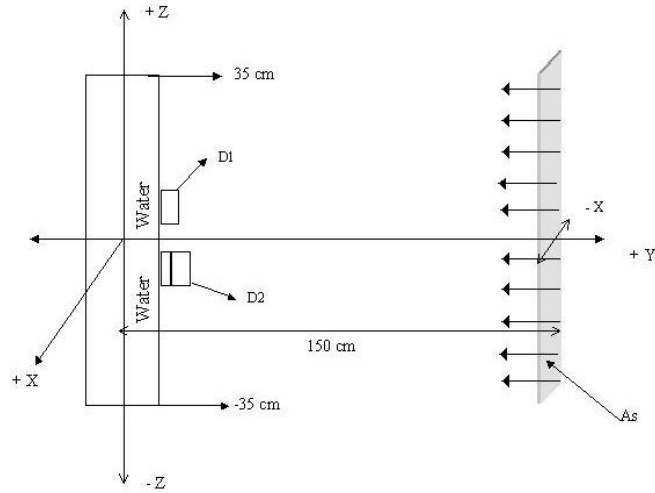


Figure 3.5. Cylindrical Water Phantom (view in YZ plane), D1 ^{10}B Detector on the Surface of the Phantom and D2 is Cd-Coated ^{10}B Detector (not to scale).

where

$$H = \int_0^{\infty} \mathfrak{R}(E)\Phi(E)dE . \quad (3.6)$$

Because the source is a parallel beam of neutrons 40 cm wide and 70 cm high and because MCNP scores results per source neutron, therefore

$$S_a = \frac{1}{40(70)} = \frac{1}{2800} \text{ cm}^{-2}. \quad (3.7)$$

The model was irradiated for seven different cases: a Maxwellian spectrum of neutrons of most probable thermal energy 0.0253 eV, a Watt fission spectrum typical of ^{235}U , and mono-energetic neutron of 1, 2, 3, 4 and 5 MeV. The appropriate normalization constants for all these cases are given in Table 3.1 and the detailed description for the calculations of the normalization constants are described in Appendix B.

Table 3.1. Normalization Constant for Seven Cases of Neutron Sources Considered Irradiating the Phantom.

Neutron Energy	$\frac{1}{S_a I}$ mSv ⁻¹
Maxwellian (T = 293.41 K)	2.64×10^{11}
Watt spectrum	7.27×10^9
1 MeV	6.73×10^9
2 MeV	6.67×10^9
3 MeV	6.80×10^9
4 MeV	6.86×10^9
5 MeV	6.91×10^9

3.3.2 MCNP Tally

Let dc_i be the count for detector i produced by neutrons with energies within dE about E , i.e.,

$$dC_i = \Sigma_{(n,\alpha)}(E)\Phi_i(E)dE \varepsilon_i v_i, \quad (3.8)$$

where $\Sigma_{(n,\alpha)}\Phi_i(E)dE$ is the number of reactions per unit volume in the detector due to neutrons having energies within dE about E (with Σ the macroscopic cross section, and $\Phi_i(E)$ the fluence) in the neutron reactive material of detector i , ε_i is the counts per unit energy (efficiency) of the detector, and v_i is the active volume of the detector i . Then the estimated detector count for a given fluence can be written as

$$\begin{aligned} C_i &= \varepsilon_i v_i \int_0^\infty \Sigma_{(n,\alpha)}(E)\Phi_i(E)dE \\ &= \varepsilon_i v_i N_i \int_0^\infty \sigma_{(n,\alpha)}(E)\Phi_i(E)dE \end{aligned} \quad (3.9)$$

Because the estimated detector response in the simulations is expressed in counts mSv⁻¹, therefore multiplying equation (3.9) with the normalization constant $1/S_a I$ will provide the desired result, namely

$$C_i = \underbrace{\varepsilon_i v_i N_i}_{\beta_2} \times \frac{1}{S_a I} \underbrace{\int_0^\infty \Sigma_{(n,\alpha)}(E)\Phi_i(E)dE}_{F_4} \text{ counts mSv}^{-1}, \quad (3.10)$$

where C_i is the response of the detector i for a fluence that produces 1 mSv in the ICRU sphere phantom. In MCNP, the F4 tally was used to estimate the detector responses.

The values considered for the detector are:

$$\varepsilon_i = 1, \quad (3.11)$$

because the detector is considered 100% efficient, and the volume of the detector in cm^3 is

$$v_i = \pi \times r^2 \times t = 3.93 \times 10^{-3}, \quad (3.12)$$

where $r = 0.5$ cm is the radius of the detector and $t = 0.005$ cm is the thickness of the detector. Therefore counts per neutron is

$$\beta_i = \varepsilon_i v_i N_{i(10)} = 1.81 \times 10^{-4}, \quad (3.13)$$

which is constant for the same type of neutron reactive material and same size of the detector and also constant for the all seven different energy cases considered in this study. The multiplicative constant for the F4 tally for the seven different cases are given in Table 3.2.

Table 3.2. F4 Tally Multiplicative Constant.

Neutron Energy	$\frac{1}{S_a I}$ mSv ⁻¹	$\beta_2 = \beta_1 \times \frac{1}{S_a I}$ counts mSv ⁻¹
Maxwellian spectrum	2.64×10^{11}	4.792×10^7
Watt spectrum	7.27×10^9	1.319×10^6
1 MeV	6.73×10^9	1.221×10^6
2 MeV	6.67×10^9	1.21×10^6
3 MeV	6.80×10^9	1.233×10^6
4 MeV	6.86×10^9	1.245×10^6
5 MeV	6.91×10^9	1.254×10^6

3.3.3 Results and Discussion of Results

The detector responses for seven cases: Five mono-energetic neutron-beams of 1, 2, 3, 4 and 5 MeV and a Watt spectrum of ²³⁵U are presented in Figure 3.6 to Figure 3.11.

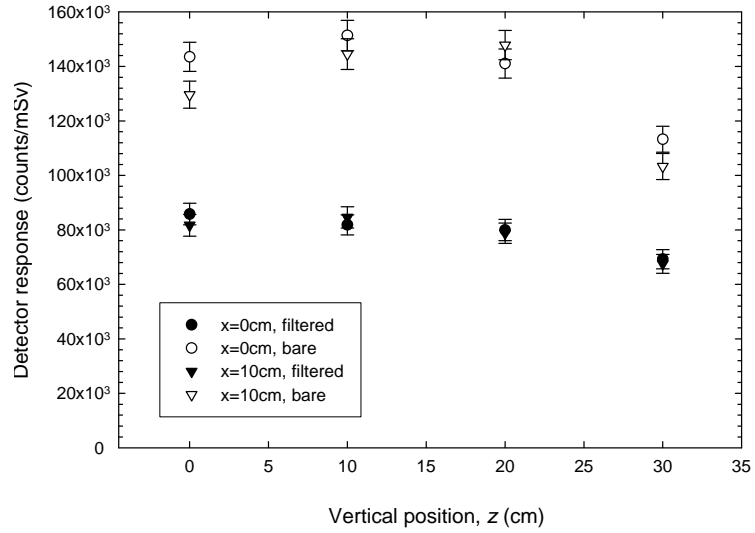


Figure 3.6. Normalized Detector Responses on Water Phantom for 1-MeV Neutron Beam.

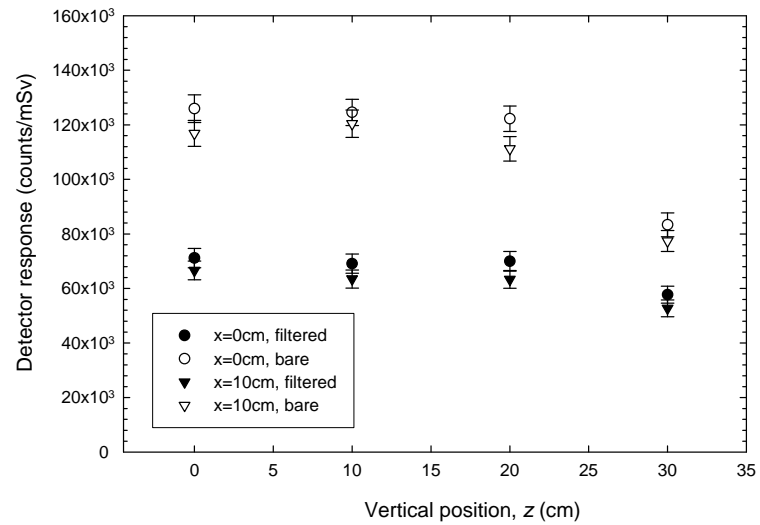


Figure 3.7. Normalized Detector Responses on Water Phantom for 2-MeV Neutron Beam.

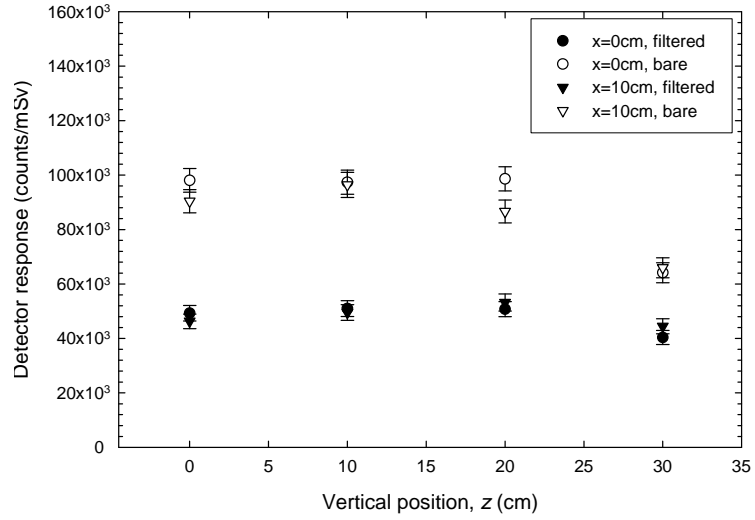


Figure 3.8. Normalized Detector Responses on Water Phantom for 3-MeV Neutron Beam.

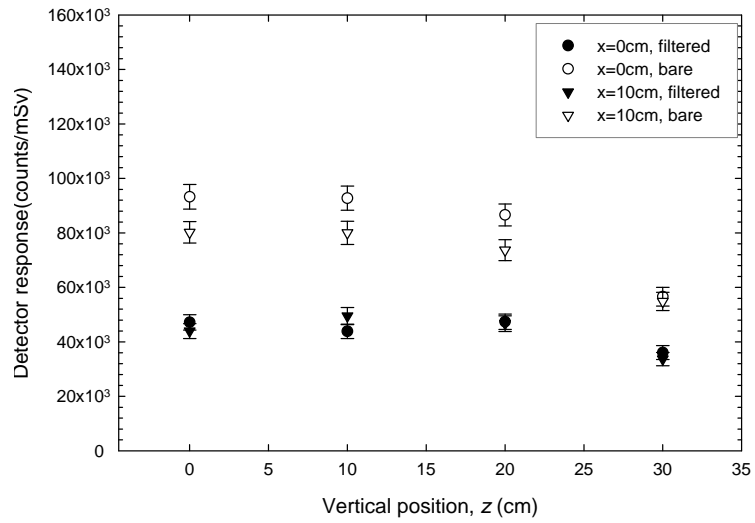


Figure 3.9. Normalized Detector Responses on Water Phantom for 4-MeV Neutron Beam.

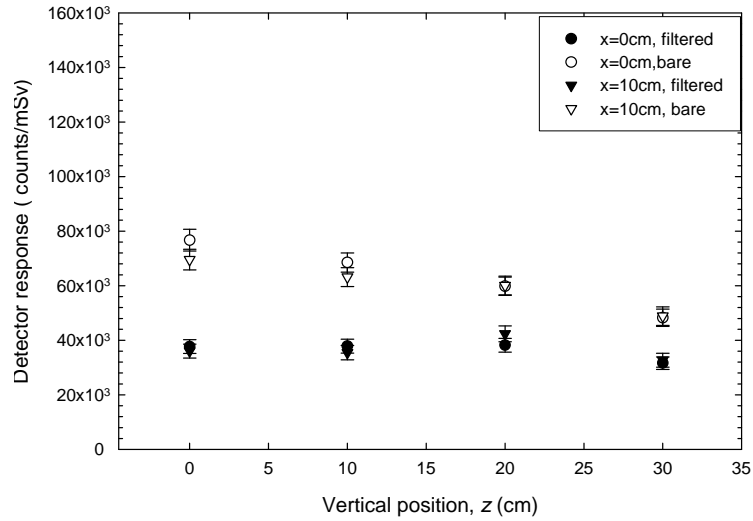


Figure 3.10. Normalized Detector Responses on Water Phantom for 5-MeV Neutron Beam.

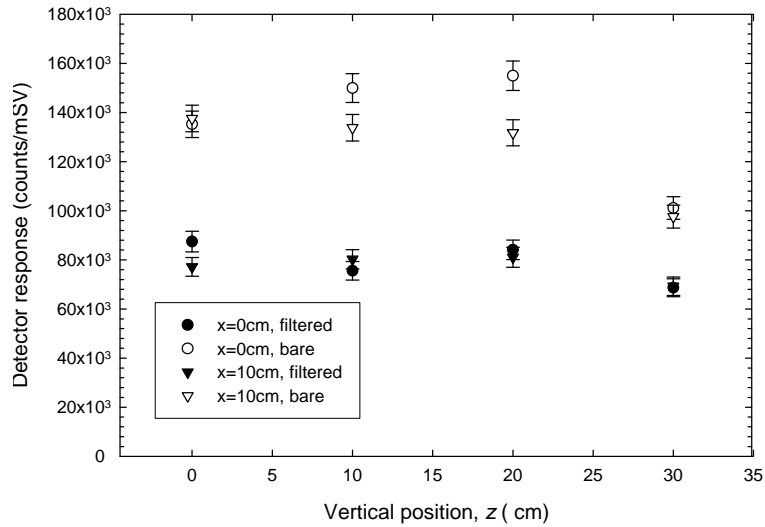


Figure 3.11. Normalized Detector Responses on Water Phantom for Watt Energy Distribution of ²³⁵U.

It is clearly noticeable that the detector responses gradually decrease with increasing neutron energy. The results indicate that the dosimeter will produce between about 30 to 145 counts per μSv for the mono-energetic neutron beams and for the Watt energy spectrum. Detector responses for a Maxwellian spectrum of ²³⁵U are shown in

Figure 3.12 and, as expected, the responses are significantly higher. Thus, the higher the average energy of the spectrum the lower the detector responses tend to be.

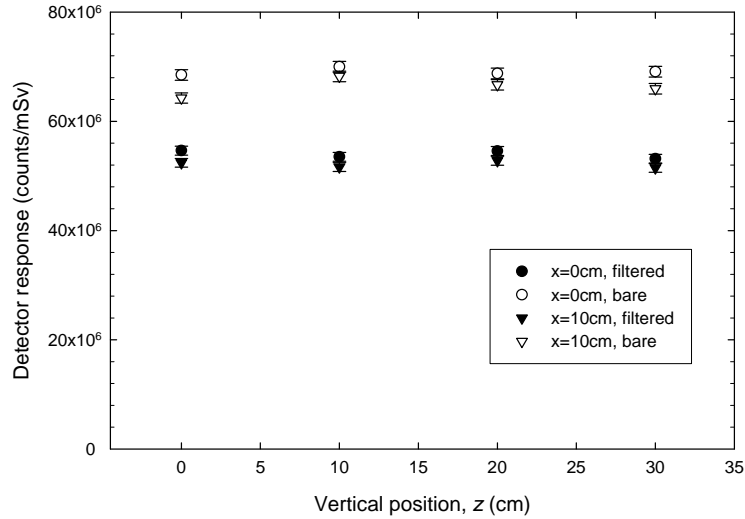


Figure 3.12. Normalized Detector Responses on Water Phantom for Maxwellian Energy Distribution of ^{235}U .

Another significant result is that the Cd-filtered detector responses were generally about 50% of the bare detector responses for the mono-energetic and Watt-spectrum neutron beam. However for the Maxwellian energy spectrum, the filtered detector responses were only about 20% of the bare detector responses. This expected result indicates that the thermalisation of neutrons occurred significantly for high-energy neutrons inside the water phantom. It can also be observed that the detector responses are relatively insensitive to location on the phantom in all energy cases.

3.4 Anthropomorphic phantom

An anthropomorphic phantom is a mathematical description or physical analog of a human body. A mathematical model of an anthropomorphic phantom can be described using Cartesian coordinates in three-dimensional space. The x , y and z axes of the model are shown in Figure 3.13; the origin of the coordinate system is at the center of the horizontal cross-section of the torso [ICRU, 1992].

For the present study, a male phantom was used [Kramer et. al. 1982]. The MCNP program was used to obtain the detector responses in counts $(\text{mSv})^{-1}$. An example code input file is attached in Appendix A. The normalization constant and the multiplicative constants used for the detector responses using F4 tally of the MCNP4C code are the same as for the case of the water phantom.

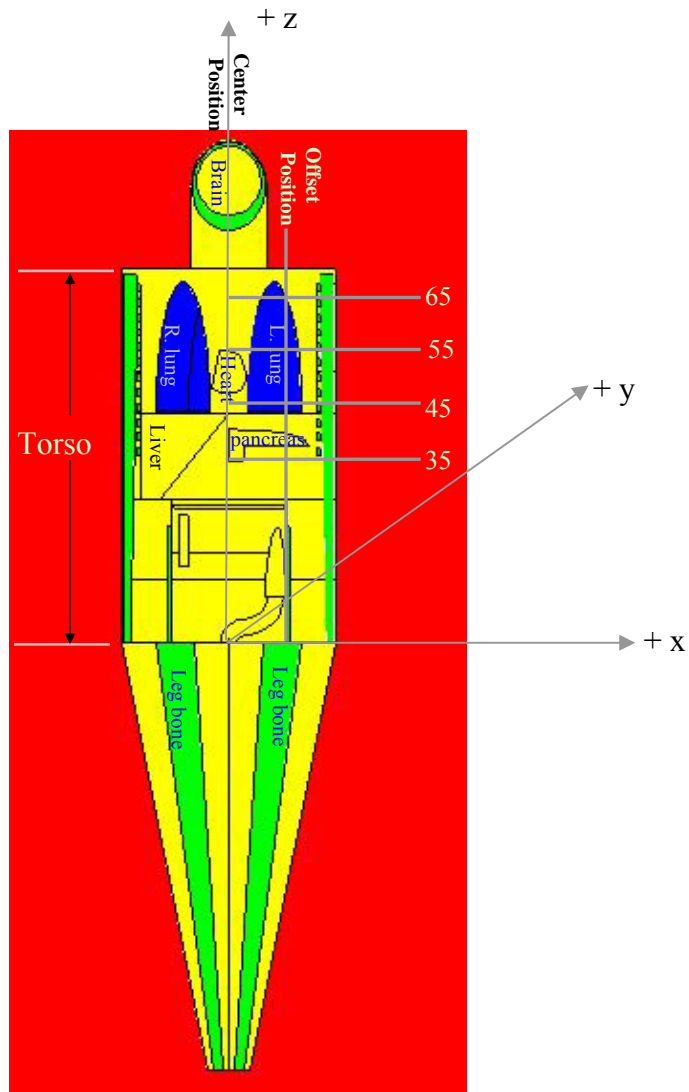


Figure 3.13. Sectional View of Adult Male Anthropomorphic Phantom Modelled and the Positions of Pair Detectors.

3.4.1 Model Geometry for Anthropomorphic Phantom

The responses of the detector pair (described in section 3.3) were observed at various positions on the torso of the anthropomorphic phantom to study the detector responses due to the phantom non-uniformity. The detector responses were normalized for a beam that would produce 1 mSv ambient dose equivalent if incident on the ICRU sphere phantom (section: 3.3.1). The four pairs of detectors were placed at the centerline of the upper torso at $x = 0$ cm, $y = -10$ cm, and at vertical positions $z = 35, 45, 55$ and 65 cm. The other four pairs of detectors were placed 10 cm offset to the left of the center line ($x = 10$ cm) and were rotated by 16.1° so as to be tangent to the phantom, at the same vertical positions.

The phantom was irradiated with a beam 40 cm wide and 70 cm high of parallel neutrons (same type of beam described for water phantom, section: 3.3) and was irradiated for the same seven cases: Maxwellian spectrum for neutrons of most probable energy 0.0253 eV, and a Watt fission spectrum for ^{235}U , and mono-energetic neutrons of 1, 2, 3, 4, and 5 MeV. The normalization constants and the multiplication constant for the Monte Carlo simulation code are described earlier in section: sections 3.3.1 and 3.3.2. The phantom was irradiated for four different directions of the neutron beam with the detectors on the chest: i) irradiation from front or AP incidence, ii) irradiation from left or LLAT incidence, iii) irradiation from right or RLAT incidence, and iv) irradiation from back or PA incidence.

3.5 Results and discussion

Results are presented in this section for various types of incidence on the torso of the anthropomorphic Phantom.

3.5.1 Detectors on Chest Irradiated from Front (AP Incidence)

The normalized detector responses for mono-energetic neutron beams and a Watt energy spectrum with AP incidence are shown in Figure 3.14 to Figure 3.19. The study indicates that the dosimeter will produce 80 (Cd filtered detectors) to 140 (bare detectors) counts μSv^{-1} for 1 MeV neutron beam and the counts μSv^{-1} decreases with increasing neutron energy [Dunn, 2006]. The study also showed that the dosimeter produce 80 (Cd

filtered detectors) to 140 (bare detectors) counts μSv^{-1} for a Watt energy spectrum of ^{235}U .

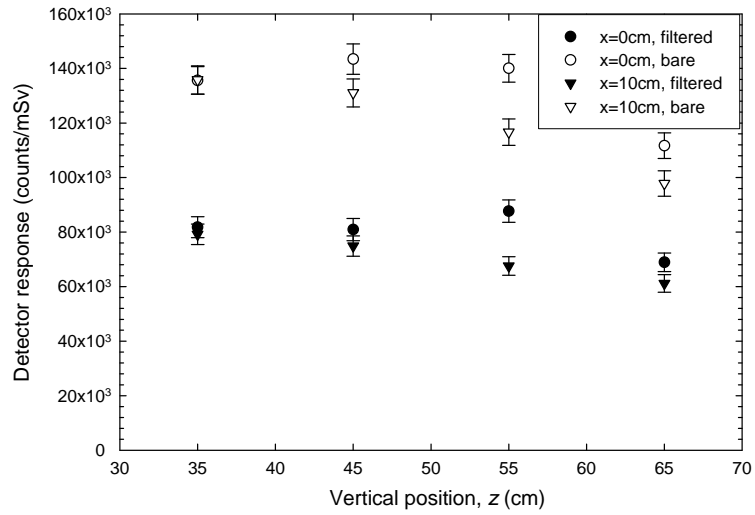


Figure 3.14. Normalized Detector Responses on the Torso of the Anthropomorphic Phantom for 1-MeV Neutron Beam with AP Incidence.

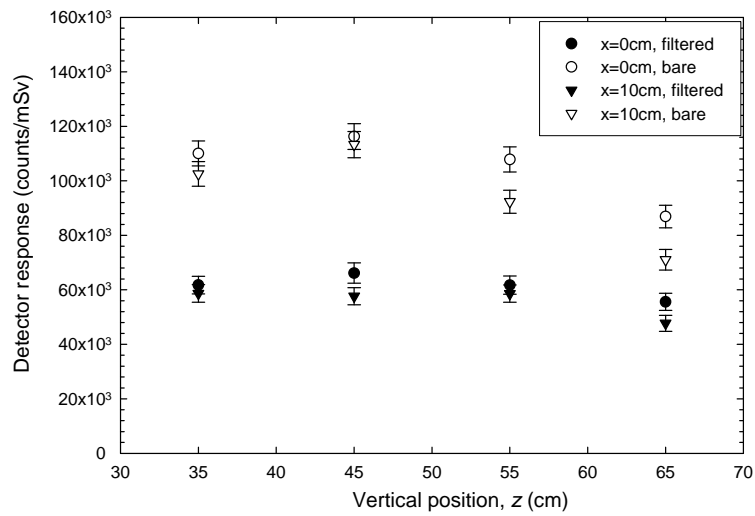


Figure 3.15. Normalized Detector Responses on the Torso of the Anthropomorphic Phantom for 2-MeV Neutron Beam with AP Incidence.

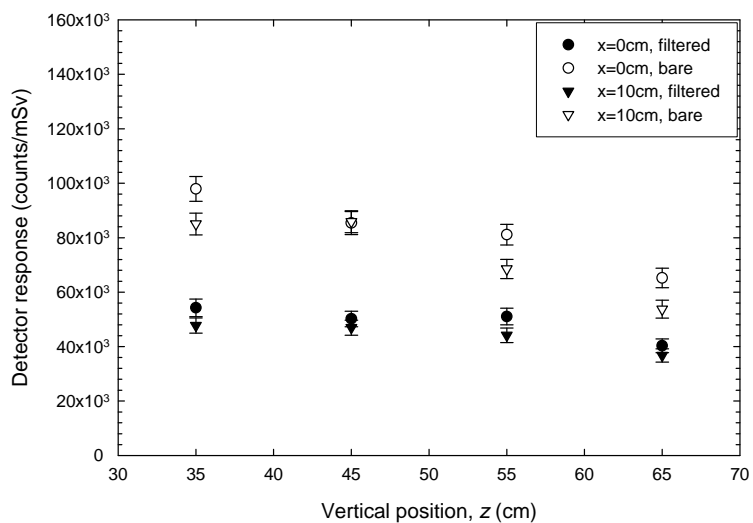


Figure 3.16. Normalized Detector Responses on the Torso of the Anthropomorphic Phantom for 3-MeV Neutron Beam with AP Incidence.

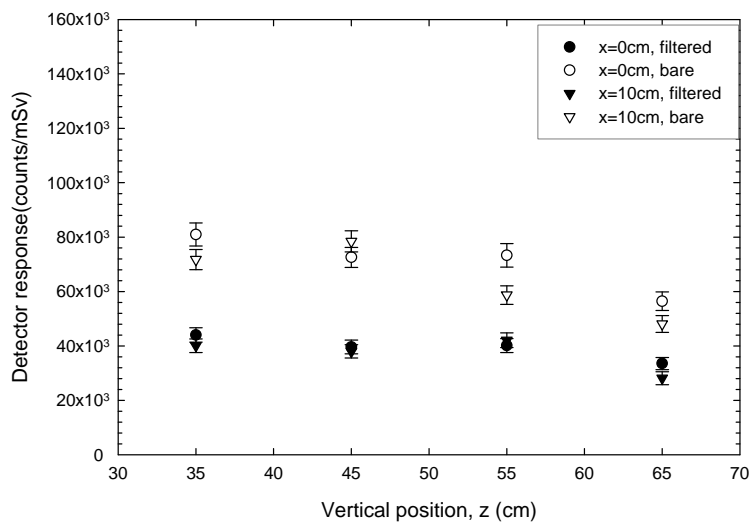


Figure 3.17. Normalized Detector Responses on the Torso of the Anthropomorphic Phantom for 4-MeV Neutron Beam with AP Incidence.

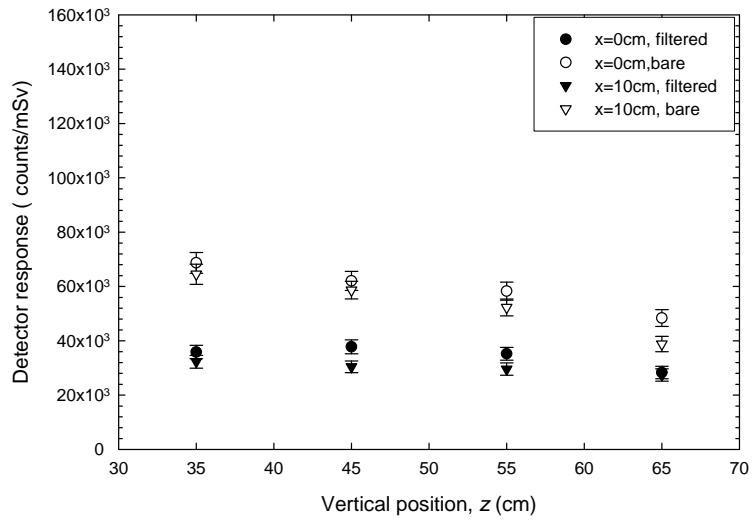


Figure 3.18. Normalized Detector Responses on the Torso of the Anthropomorphic Phantom for 5-MeV Neutron Beam with AP Incidence.

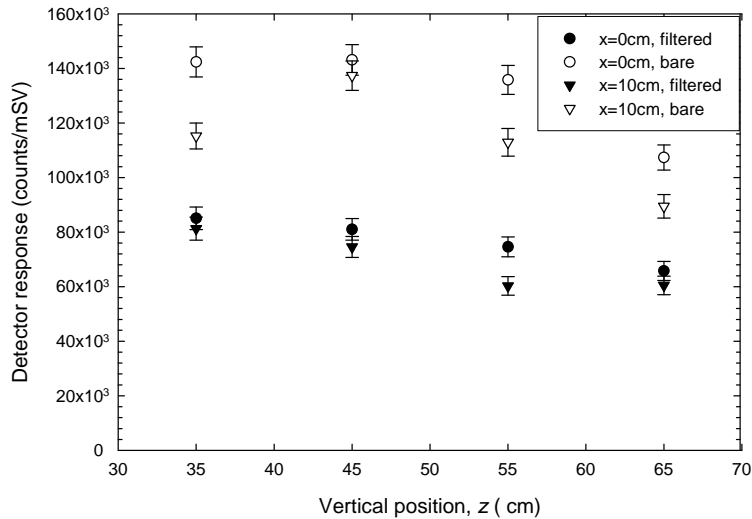


Figure 3.19. Normalized Detector Responses on the Torso of the Anthropomorphic Phantom for Beam with a ²³⁵U Watt-spectrum with AP Incidence.

The results for a Maxwellian spectrum of ²³⁵U are shown in Figure 3.20. Higher counts are obtained due to the higher thermal neutron absorption cross section.

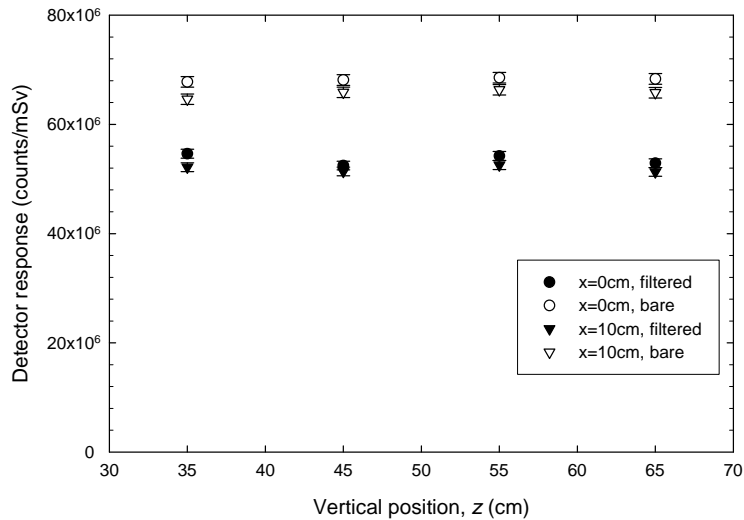


Figure 3.20. Normalized Detector Responses on the Torso of the Anthropomorphic Phantom for beam with a ^{235}U Maxwellian-Spectrum and with AP Incidence

Figure 3.14 to Figure 3.19 indicate that the differences among the vertical detector-responses positioned at $z = 35, 45, 55$ cm are fairly small (about 10%), whereas, the detector placed at $z = 65$ cm, shows 30% less responses than the previous one (at $z = 55$ cm). The Maxwellian energy spectrum produced significantly lower variation among the detector responses. Even the detector positioned at $z = 65$ cm did not show a significant change. For this energy spectrum, the difference between the detectors placed at the same position (center line or offset position) was about 5%. Therefore it can be concluded that the detector response is relatively independent on the placement of the detector on the torso.

For AP incidence another interesting result was observed for the Cd-filtered detectors. The responses are about 50% less than the bare detectors for the monoenergetic neutron beam and for Watt energy spectrum and about 20% less for the Maxwellian energy spectrum. The decrease in counts for the Cd filtered detectors indicates that the high energy neutrons are thermalized inside the anthropomorphic phantom and the neutrons below the Cd cutoff are filtered by the Cd filtered detectors.

Fast neutron sources such as Pu-Be are commonly used in the operation of nuclear reactor and the dosimetry of this source is a concern for the reactor personnel. Therefore the detector responses for AP incidence using Pu-Be source spectrum was also investigated. A Pu-Be source is a mixture of ^{238}Pu with ^9Be in which ^{238}Pu emits alpha particles that are absorbed by ^9Be followed by the prompt emission of neutrons. The reaction is



A typical spectrum of a Pu-Be source is shown in Figure 3.21. The detector responses normalized to a mSv in the ICRU spherical phantom as estimated by MCNP for a beam having a Pu-Be spectrum is shown in Figure 3.22.

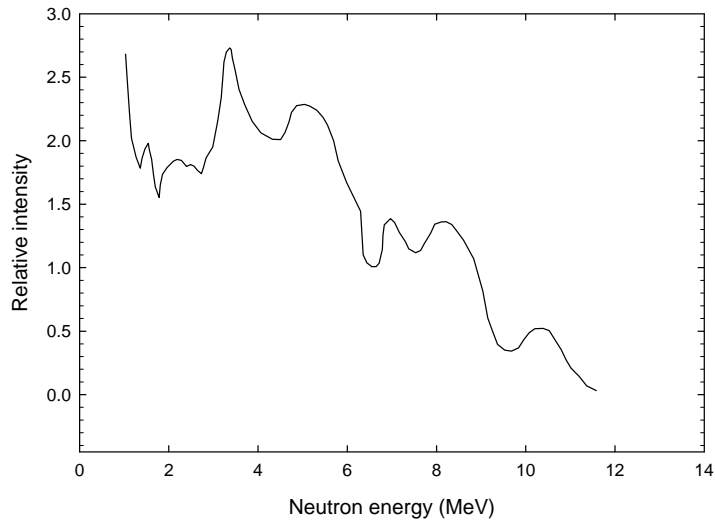


Figure 3.21. Pu-Be Spectrum (Shultis and Faw, 2000).

It was found that the dosimeter irradiated with this source produced 40 (filtered detectors) to 95 (bare detectors) counts and the differences between the bare and Cd-filtered detectors were about 50%.

Comparing the results obtained for the water phantom and anthropomorphic phantoms, it is found that for both cases AP incidence of the neutron beam produce similar results.

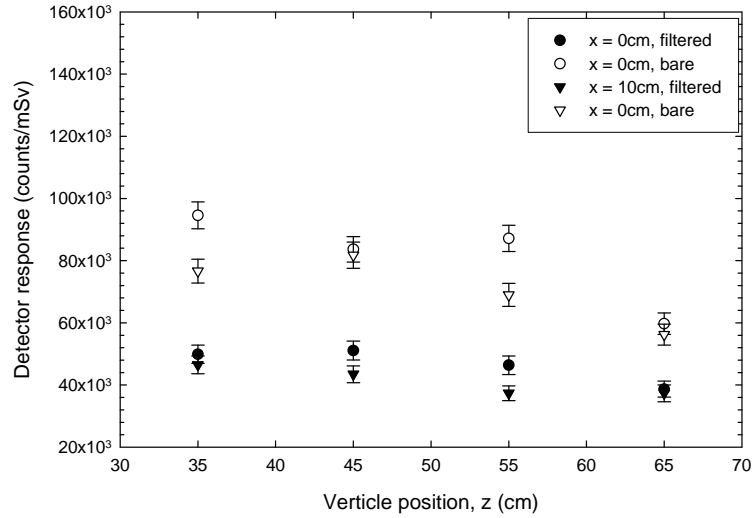


Figure 3.22. Normalized Detector Responses on the Torso of the Anthropomorphic Phantom for a Pu-Be Source and with AP Incidence.

3.5.1.1 Spectrum Determination Constant

Another interesting result can be observed from the simulation study that the difference of the bare and Cd-filtered detector counts which differs for different neutron spectra; this parameter is called “Spectrum Determination Constant (SDC)” in this study. This observation will provide some information about the incident neutron beam. This was observed for detector position was at $x = 0$ cm and $z = 45$ cm. The SDC is defined as

$$SDC = \frac{N_b - N_{Cd}}{N_b}, \quad (3.15)$$

where N_b , is the bare detector response, and N_{Cd} , is the Cd-filtered detector response.

Table 3.3. *SDC* for Various Neutron Energy Spectra.

Neutron Energy Spectrum	Bare detector Counts, N_b (Counts mSv ⁻¹)	Cd-filtered Detector Counts, N_{Cd} (Counts mSv ⁻¹)	<i>SDC</i>
Maxwell	68115100	52449900	0.23 ± 0.0001
Watt Energy Spectrum for ²³⁵ U	143108	80989.4	0.43 ± 0.0025
Mono-Energetic Neutron Beam			
1	143408	80891.2	0.44 ± 0.0025
2	116239	66146.5	0.43 ± 0.0028
3	85353.9	50149.9	0.41 ± 0.0033
4	72562.5	39623.6	0.45 ± 0.0034
5	62042.5	37788.1	0.39 ± 0.0040
Pu-Be Source	83623.1	51070.9	0.39 ± 0.0034

It can be observed from Table 3.3 that the *SDC* can clearly distinguish the slow from fast neutron spectra. It is more difficult, but perhaps possible, to distinguish between a Watt energy spectrum and a Pu-Be source spectrum.

3.5.2 Detectors on Chest Irradiated from Left and Right

The normalized detector responses for the same seven energy cases considered previously for left lateral (LLAT) incidence are shown in Figure 3.23 to Figure 3.29 and for right lateral (RLAT) incidence are shown in Figure 3.30 to Figure 3.36. The variation among the corresponding detectors is considerably lower for LLAT, RLAT incidence than for the AP case. But the dosimeters still produce tens of counts μSv^{-1} for the mono-energetic and Watt energy distribution and 200 to 20,000 counts μSv^{-1} for the Maxwellian energy distribution. The centered-positioned detector responses in both cases (LLAT and RLAT) are almost the same for all seven energy cases.

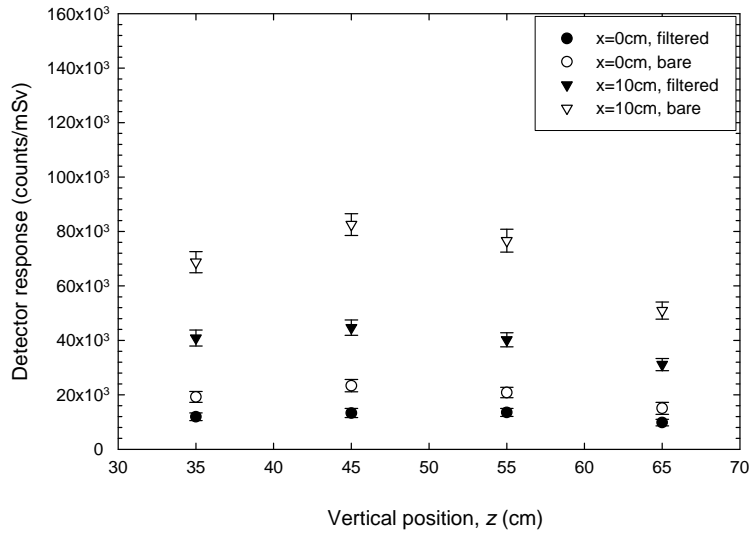


Figure 3.23. Normalized Detector Responses on the Torso of the Anthropomorphic Phantom for 1-MeV Neutron Beam and with LLAT Incidence.

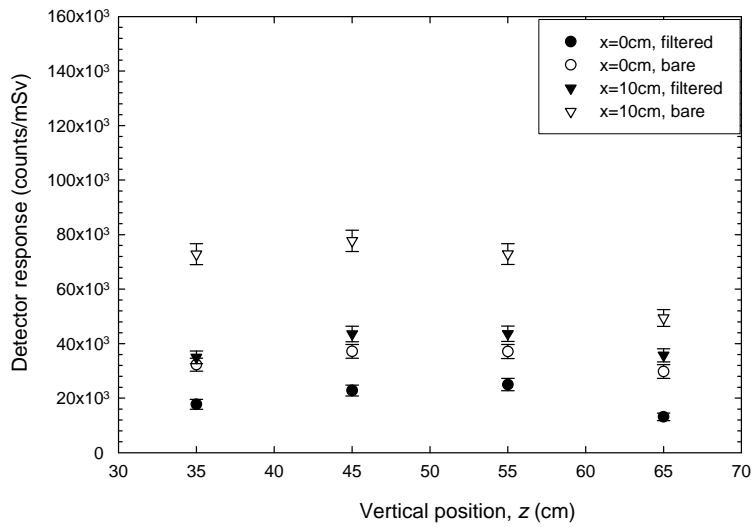


Figure 3.24. Normalized Detector Responses on the Torso of the Anthropomorphic Phantom for 2-MeV Neutron Beam and with LLAT Incidence.

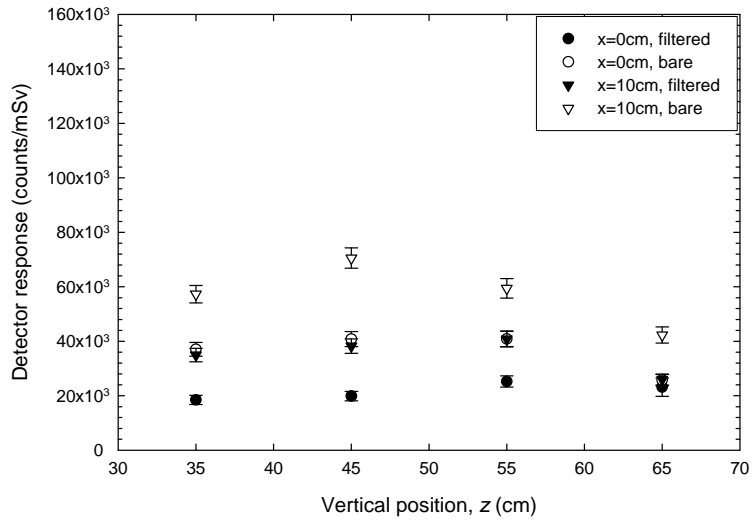


Figure 3.25. Normalized Detector Responses on the Torso of the Anthropomorphic Phantom for 3-MeV Neutron Beam and with LLAT Incidence.

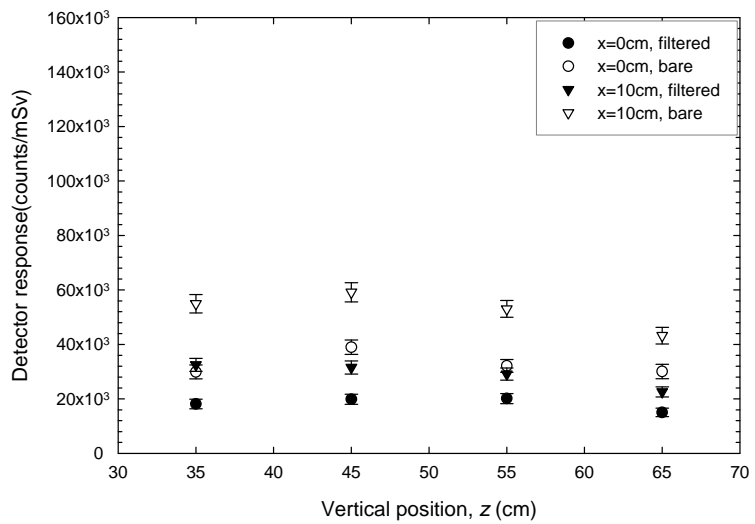


Figure 3.26. Normalized Detector Responses on the Torso of the Anthropomorphic Phantom for 4-MeV Neutron Beam and with LLAT Incidence.

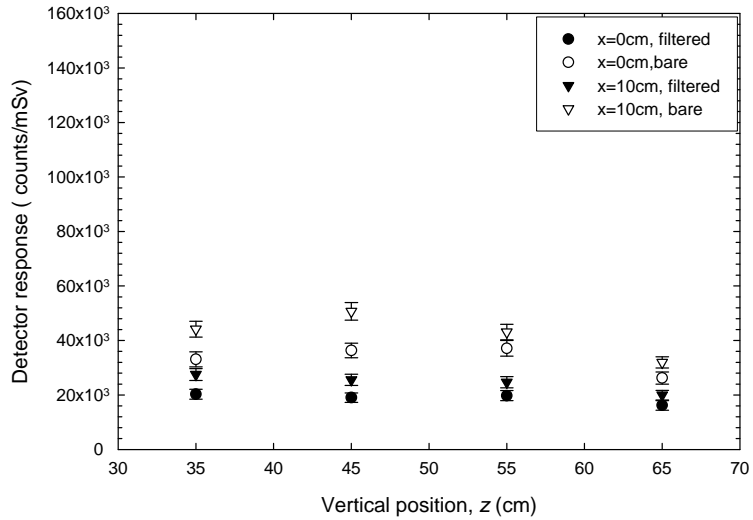


Figure 3.27. Normalized Detector Responses on the Torso of the Anthropomorphic Phantom for 5-MeV Neutron Beam and with LLAT Incidence.

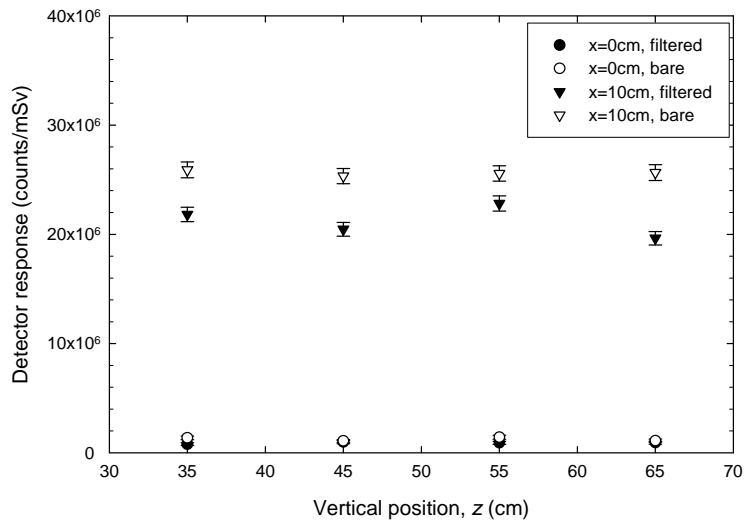


Figure 3.28. Normalized Detector Responses on the Torso of the Anthropomorphic Phantom for beam with a ²³⁵U Maxwellian-Spectrum and with LLAT Incidence.

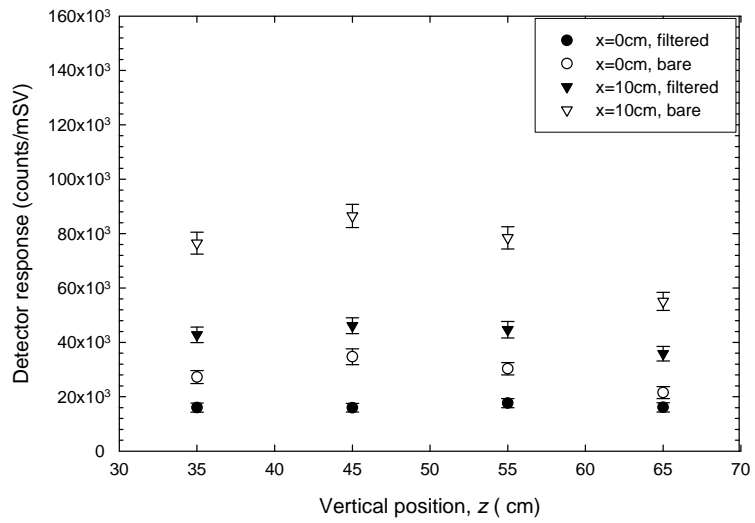


Figure 3.29. Normalized Detector Responses on the Torso of the Anthropomorphic Phantom for beam with a ²³⁵U Watt-Spectrum with LLAT Incidence.

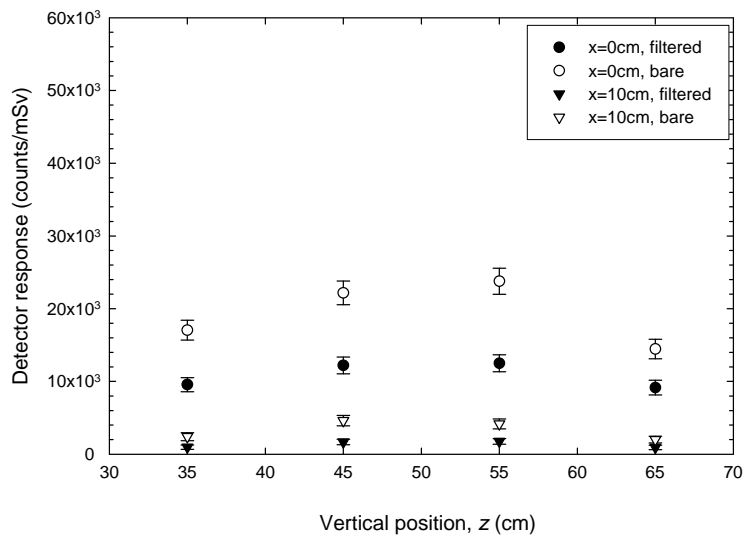


Figure 3.30. Normalized Detector Responses on the Torso of the Anthropomorphic Phantom for 1-MeV Neutron Beam and with RLAT Incidence.

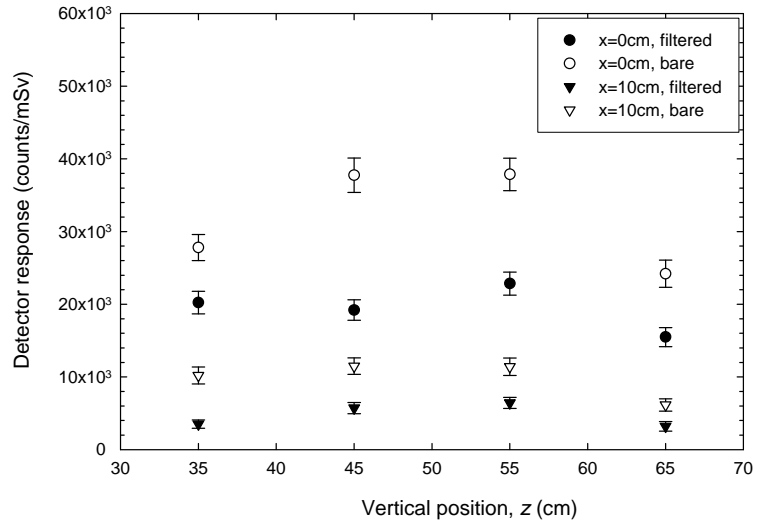


Figure 3.31. Normalized Detector Responses on the Torso of the Anthropomorphic Phantom for 2-MeV Neutron Beam and with RLAT Incidence.

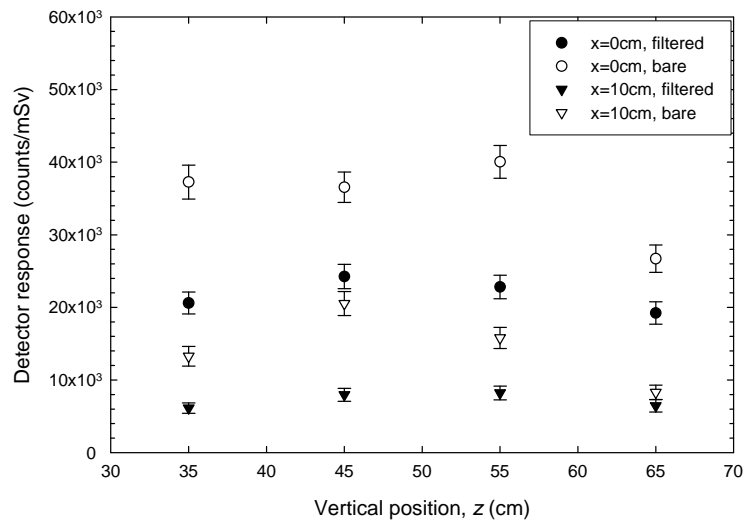


Figure 3.32. Normalized Detector Responses on the Torso of the Anthropomorphic Phantom for 3-MeV Neutron Beam and with RLAT Incidence.

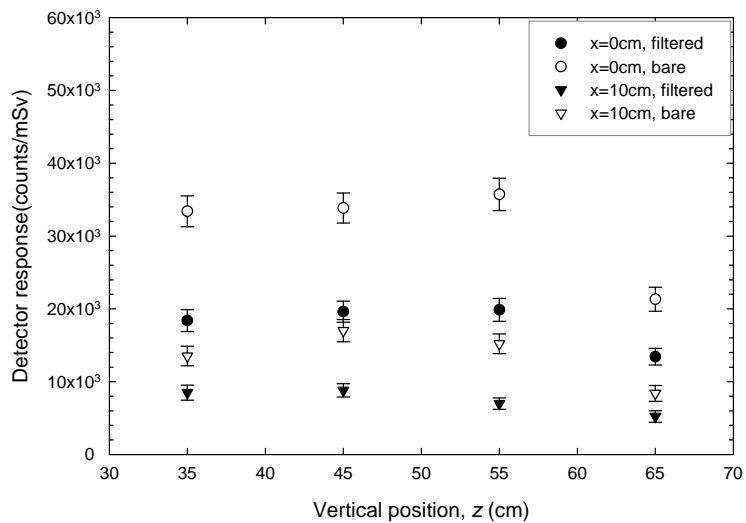


Figure 3.33. Normalized Detector Responses on the Torso of the Anthropomorphic Phantom for 4-MeV Neutron Beam and with RLAT Incidence.

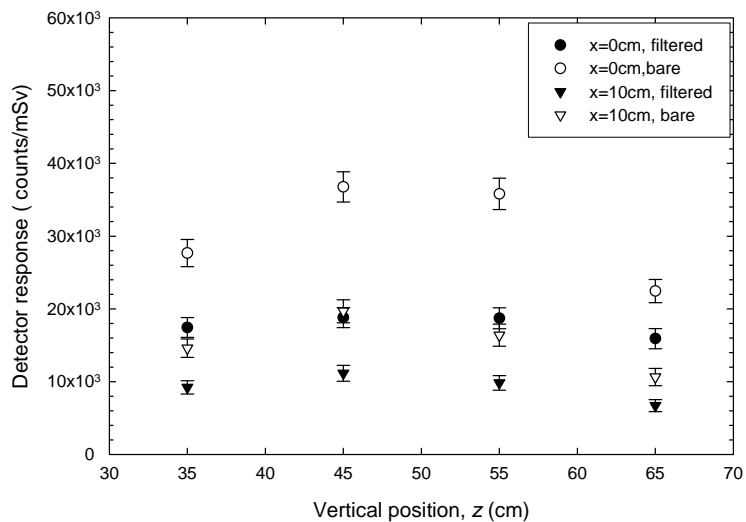


Figure 3.34. Normalized Detector Responses on the Torso of the Anthropomorphic Phantom for 5-MeV Neutron Beam and with RLAT Incidence.

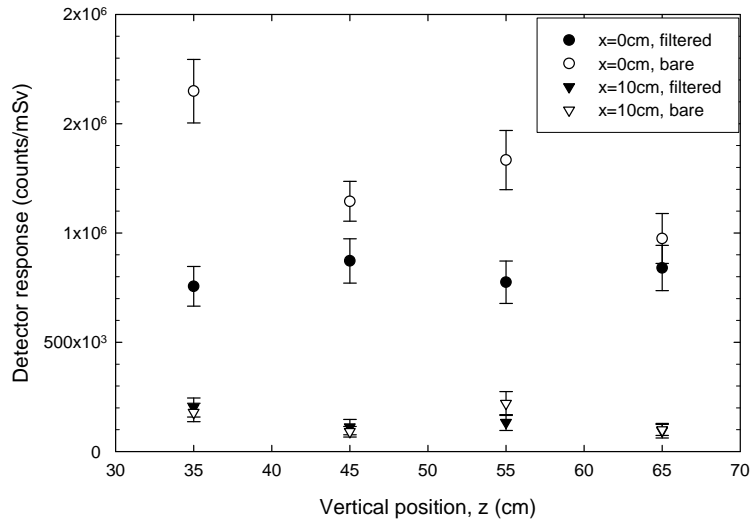


Figure 3.35. Normalized Detector Responses on the Torso of the Anthropomorphic Phantom for Maxwellian-Spectrum of ²³⁵U and with RLAT Incidence.

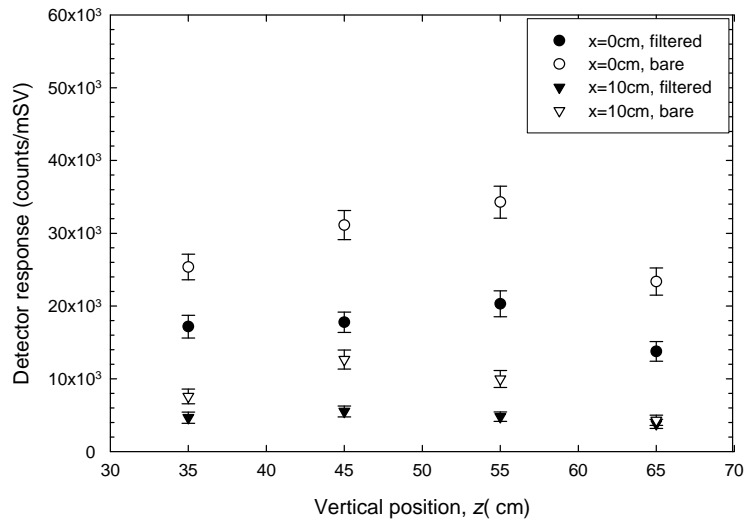


Figure 3.36. Normalized Detector Responses on the Torso of the Anthropomorphic Phantom for beam with a ²³⁵U Watt-Spectrum and with RLAT Incidence.

3.5.3 Detectors on Chest Irradiated from Back (PA Incidence)

The normalized detector responses for seven different energy cases for the posterior anterior (PA) cases are shown in Figure 3.37 to Figure 3.42.

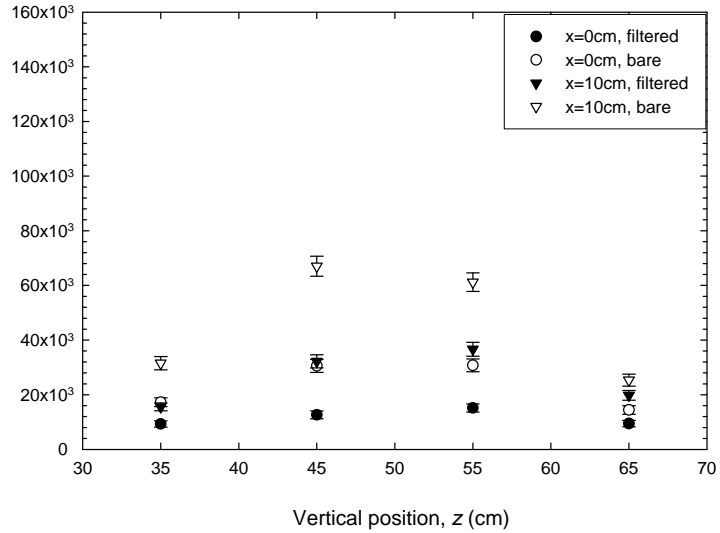


Figure 3.37. Normalized Detector Responses on the Torso of the Anthropomorphic Phantom for beam with 1 MeV Neutron Beam and with PA Incidence.

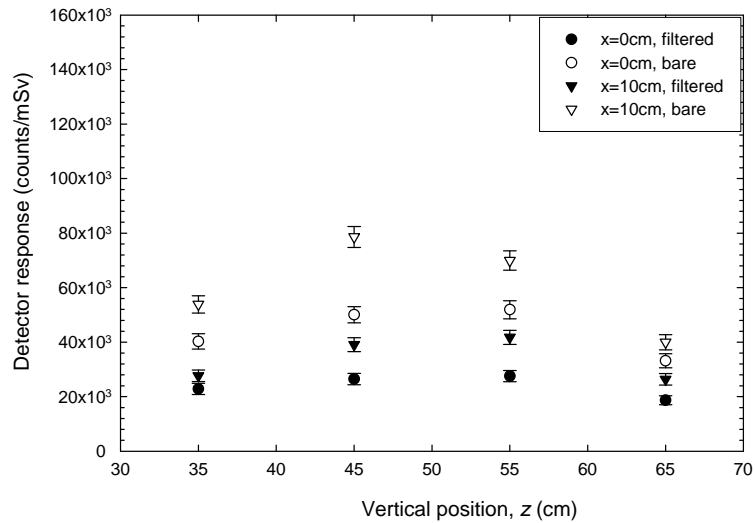


Figure 3.38. Normalized Detector Responses on the Torso of the Anthropomorphic Phantom with 2 MeV Neutron Beam and with PA Incidence.

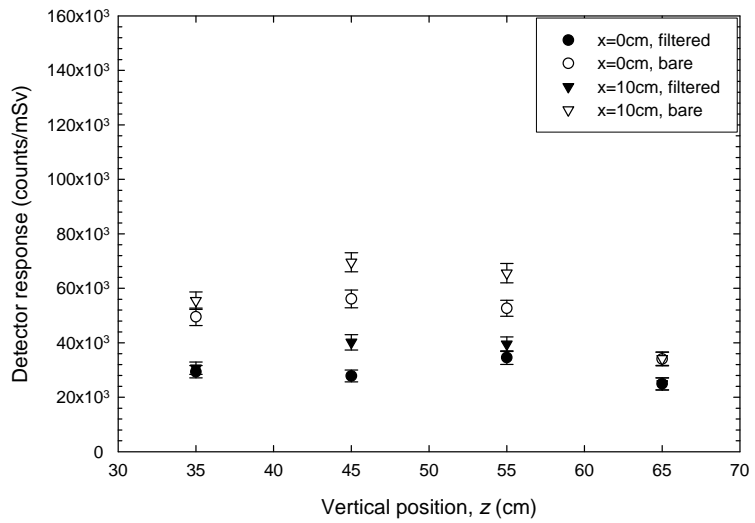


Figure 3.39. Normalized Detector Responses on the Torso of the Anthropomorphic Phantom for beam with 3 MeV Neutron Beam and with PA Incidence.

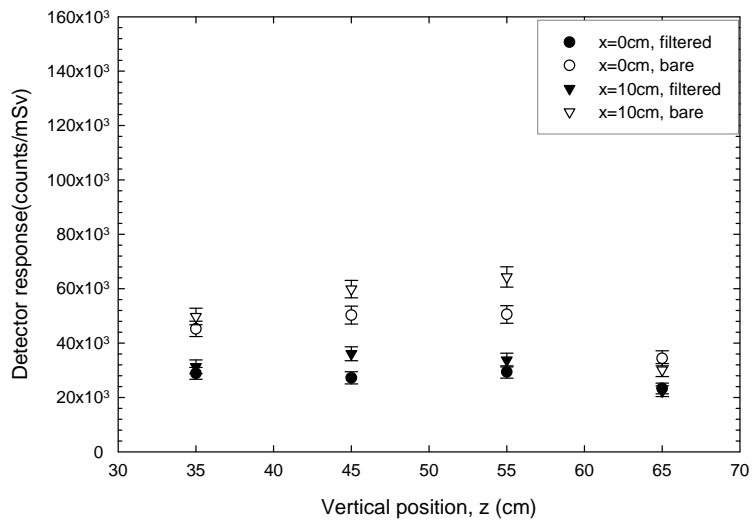


Figure 3.40. Normalized Detector Responses on the Torso of the Anthropomorphic Phantom for beam with 4 MeV Neutron Beam and with PA Incidence.

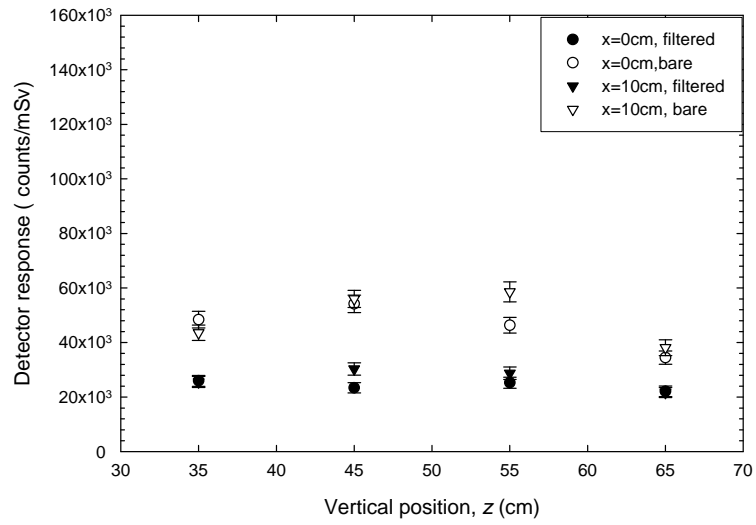


Figure 3.41. Normalized Detector Responses on the Torso of the Anthropomorphic Phantom for beam with 5 MeV Neutron Beam and with PA Incidence.

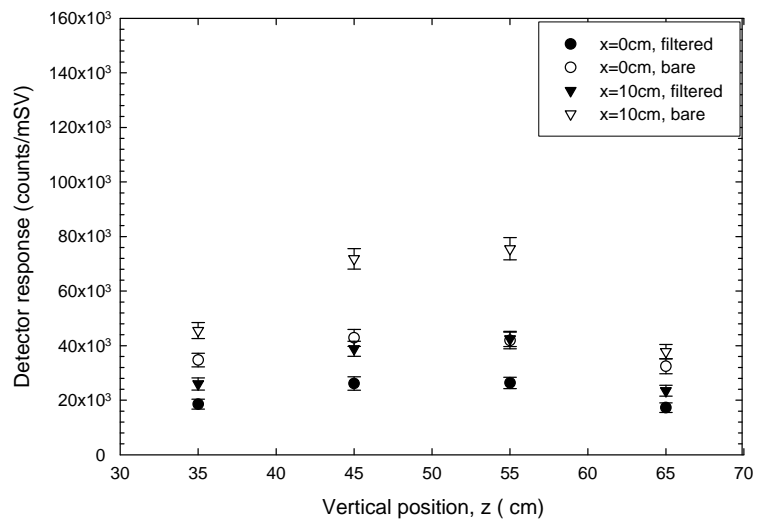


Figure 3.42. Normalized Detector Responses on the Torso of the Anthropomorphic Phantom for beam with a ²³⁵U Watt-Spectrum and with PA Incidence.

In this case the dosimeters are producing 20 to 60 counts μSv^{-1} for mono-energetic neutrons and the Watt energy distribution. However a significant increase in counts for the $z = 45$ and $z = 55$ cm, offset positioned detectors was observed. This is most probably due to the presence of the lung at these two positions on the torso. Because the density of the lung tissue is close to air, therefore fewer neutrons are thermalized in this part of the torso. For Maxwellian spectrum, Figure 3.43, it can be observed that the counts for these two positions detectors are increased significantly.

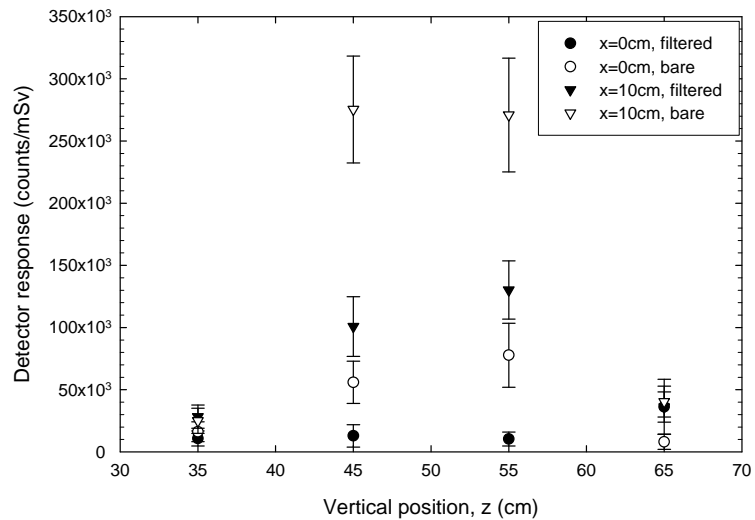


Figure 3.43. Normalized Detector Responses on the Torso of the Anthropomorphic Phantom for beam with a ^{235}U Maxwellian Energy Spectrum and with PA Incidence.

4 Characterization of Semiconductor Neutron Dosimeter Experimental Study

The perforated semiconductor neutron detector (SND) provides counts in a neutron field and the main purpose of this study is to characterize the SND, that is to estimate the relationship between detector counts and dose with a human torso present.

To relate the SND counts and dose, it is useful to know:

- i) Neutron flux of the beam that irradiates the phantom. The flux was determined from a gold foil experiment.
- ii) Neutron dose on the surface of an anthropomorphic phantom due to the neutron beam. Thermoluminescence dosimeters were used to determine neutron dose on the surface of the anthropomorphic phantom.
- iii) Counts on both bare and Cadmium (Cd) filtered SNDs recorded in the same geometry, by placing the SNDs on the anthropomorphic phantom. SND counts were also recorded without the phantom for a linearity check of the detector.

The experimental procedures to estimate these quantities with results and appropriate theories are discussed in the following sections.

4.1 Calculation of Neutron Flux

A gold-foil experiment was used to determine the neutron flux at the point where the SND counts would be recorded. To calculate flux, it was necessary to know the efficiency of the detector, which is essential for counting the irradiated gold foil. A high purity Germanium (HPGe) detector was used for counting.

4.1.1 Efficiency of HPGe Detector

Semiconductor detectors are useful for gamma ray spectroscopy because of their superior energy resolution. The detection efficiency as a function of photon energy was

studied for one of the high-purity germanium (HPGe) detectors (detector model GC4019) in the Neutron Activation Analysis (NAA) lab at Kansas State University.

4.1.1.1 Theory

Radiation detectors generally are not 100% efficient at detecting the radiation quanta that are incident on the detector. Therefore it is necessary to find the detector efficiency with respect to different gamma-ray energies. The total efficiency, ε of the detector at a particular energy E is defined as

$$\varepsilon = \frac{\text{number of full energy pulses recorded}}{\text{number of radiation quanta emitted by source}} \quad (4.1)$$

Total efficiency depends on the thickness and radius of the detector and also on source-to-detector distance.

The decay rate or activity of a sample is given by [Shultis and Faw, 2002]

$$A(t) = A_0 e^{-\lambda t}, \quad (4.2)$$

where A_0 is the initial activity, λ is the decay constant, and t is the elapsed time. The decay constant λ is defined as

$$\lambda = \frac{0.693}{t_{1/2}}, \quad (4.3)$$

where $t_{1/2}$, is the half-life (time to decay one-half of the initial isotopes) of the radionuclide.

The SI unit for activity is the Becquerel (Bq), which is defined as one disintegration per second. The older unit of activity is the Curie (Ci). The relationship between Ci and Bq is

$$1 \text{ Ci} = 3.7 \times 10^{10} \text{ Bq}. \quad (4.4)$$

4.1.1.2 Methods for Calculation of Counts under the Peak

To calculate the efficiency of the detector it is necessary to determine the area under the full-energy peaks that appear in the spectrum. The area under the peak can be determined by adding counts in the region of the full-energy peaks. But the full-energy peaks also have some contribution from other gamma rays; therefore it is necessary to

subtract some counts from the total counts of the full-energy peaks. Usually a base line is used to separate the peak from the background counts, as shown in Figure 4.1. Therefore the peak area can be written as [Knoll, 2000],

$$\sum_{j=i}^f C_j - (f-i) \frac{C_f + C_i}{2}, \quad (4.5)$$

where C_j is the number of counts in channel j , i is the initial channel number and f is the final channel number of the full-energy peak, C_i and C_f are the corresponding counts in channels i and f .

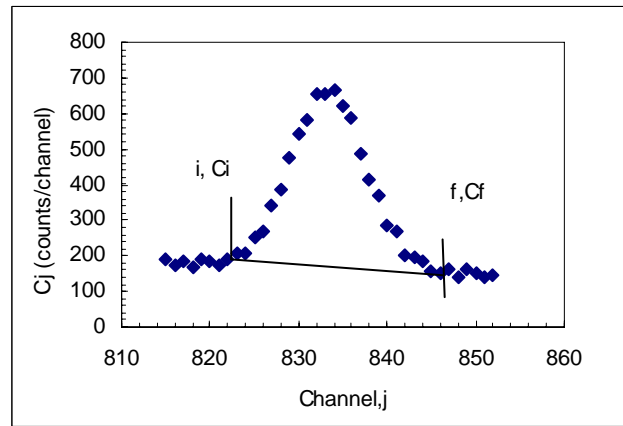


Figure 4.1. Peak with a Base Line to Calculate the Net Counts under the Full-Energy Peak (Spectrum: NE 799 HW).

There are sometimes two closely lying peaks (which are not fully separated) in the spectrum. To resolve this problem, an analytic function can be used to fit each individual peak and to calculate the peak area and the center energy of each peak. Because full-energy peaks can be approximated by Gaussian functions, the fitting function consists of a Gaussian to describe the peak and a linear function to describe the background of the peak [Tsoulfanidis, 1983], i.e.,

$$f(i) = a + bi + \sum_{j=1}^J \frac{C_j}{(\sqrt{2\pi})\sigma_j} \exp\left[-\frac{(\mu_j - i)^2}{2\sigma_j^2}\right], \quad (4.6)$$

where a is the intercept and b is the slope of the straight line, i corresponds to the channel number, J corresponds to the total number of full-energy peaks in the data, μ_j is

the mean of the j^{th} full-energy peak, σ_j is the standard deviation of the j^{th} peak (which is related to the width of the peak), and C is the peak height. The function $f(i)$ represents the modeled counts in channel i . The area under the j^{th} peak can be calculated by integrating the Gaussian function and is given by,

$$A_j = C_j . \quad (4.7)$$

4.1.1.3 Experimental Procedure

To determine the efficiency of the HPGe detector, the following procedure was followed:

- A mixed source consisting of Eu-152, Eu-154 and Eu-155 was used to collect gamma-ray spectra with peaks at several different energies.
- The correction for decay from the certification date to the counting date was calculated using equation (4.2). The contents of the mixed source: half-lives, activities on the calibration date (August 29th, 2005) in μCi and on the experiment date (June 20th, 2006) in μCi and in Becquerel are recorded in Table 4.1.

Table 4.1. Contents of the Mixed Source, Half-Lives, Decay Constants, Activities on Calibration Date and on Experiment Date.

Source	Half-life, (year)	Decay constant $= \frac{0.693}{t_{1/2}} (\text{day})^{-1}$	Activity on the calibration date, (August 29 th , 2005), μCi	Activity on the experiment date (June 20 th , 2006)	
				μCi	DPS
Eu -152	13.54	1.4022×10^{-04}	0.211	0.2024	7489.5
Eu -154	8.593	2.2095×10^{-04}	0.248	0.2327	8595.0
Eu -155	4.75	3.997×10^{-04}	0.357	0.3172	11736.

- The gamma-ray energies emitted from the mixed source and their respective intensities were collected from the web site <http://www.nndc.bnl.gov/nudat2/>.
- To obtain good counting statistics, the counts under the major peaks should be at least 10,000. Therefore the counting time of 40 minutes at a source detector distance of 4 inch (10.16 cm) was used. A 40 min background count was collected and was subtracted from the source counts.

- The collected spectrum is shown in Figure 4.2, and the two pairs of doublets (double peaks) at 122 & 123 keV and 245 & 248 keV are shown in Figure 4.3.

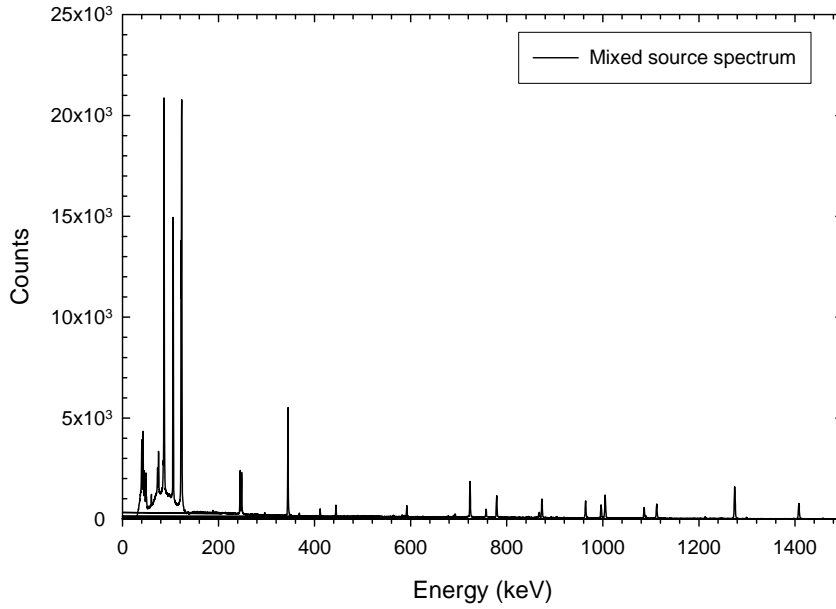


Figure 4.2. Mixed Source Spectrum.

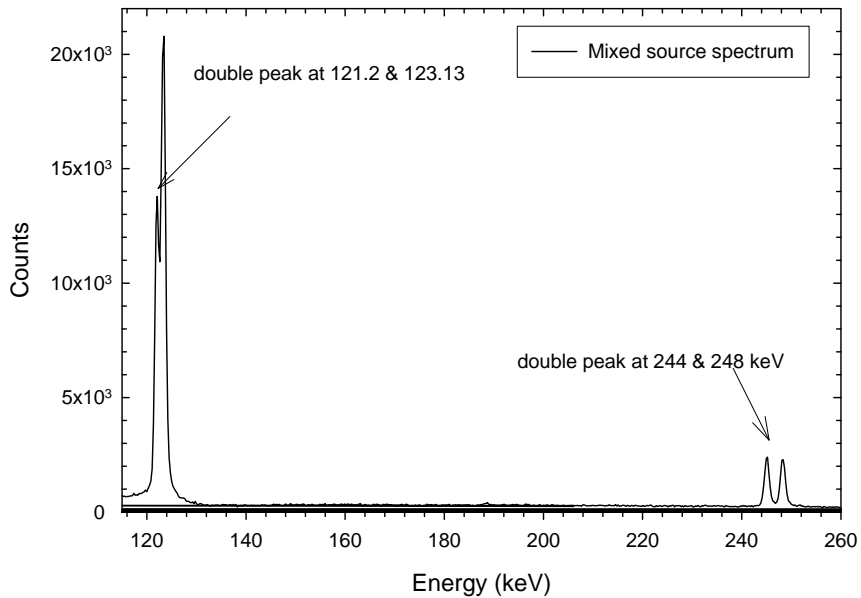


Figure 4.3. Double Peaks of the Mixed Source Spectrum at Energies, 121.2 (Eu 152) & 123.13 (Eu 154) and 244 (Eu 152) & 248 ((Eu 154) (expand window).

- Another doublet was observed at 996 & 1004.8 keV is shown in, Figure 4.4.

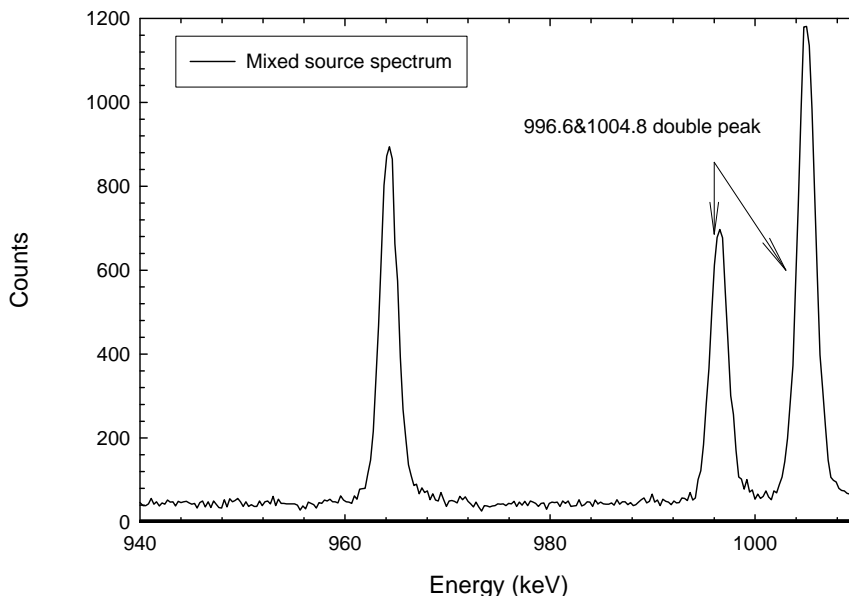


Figure 4.4. Double Peaks of the Mixed Source Spectrum at Energies 996.6 keV (Eu 154) and 1004.8 keV (Eu 154) (expand window).

4.1.1.4 Results and Discussion

The fit of the analytic function in Eq. (4.6) to the data was implemented using a FORTRAN program [Dunn, 2004]. The fitting function was used to calculate the area under the single peak and the center position of the single peak. The same fitting function was used to calculate the area and the center position of the individual peak of the doublets. The efficiencies of the detector were calculated using Eq. (4.1). The area under each peak, the related source, the corresponding intensities and the calculated efficiencies are listed in Appendix C.

The energy vs. efficiency of the detector is represented in Figure 4.5; the circles represent the data points and the solid line represents an empirical fit to these data points; a TableCurve (Jandel Scientific, 1996) computer program was used for this empirical fit. The curve fit equation was

$$\ln \varepsilon = a + \frac{b}{E^{0.5}} + \frac{c}{E}, \quad (4.8)$$

where $a = -7.9766141$, $b = 74.0188$, $c = -407.59598$ (from the curve fit equation), E represents the energy and ε is the corresponding efficiency. The efficiency of the detector was determined for a total of 20 energies in the energy range 60 keV to 1408 keV. The efficiency of the detector is increasing from 60 keV to 123 keV and after that the efficiency decreases with increasing energy (Figure 4.5). It is noted that the efficiencies of the two closely spaced peaks at 121.8 and 123.1 keV differ noticeably, indicating that there was likely a problem in fitting these two closely-spaced peaks.

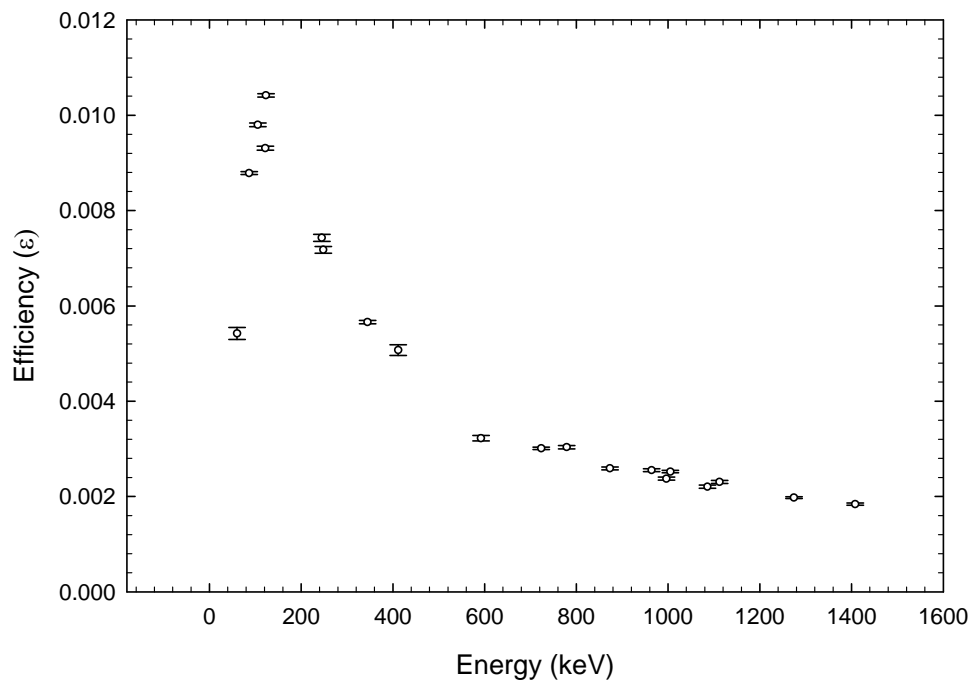


Figure 4.5. Efficiency vs. Energy Curve.

4.1.2 Measurement of Flux

The gold foil activation method was used to measure the thermal and fast flux in the same geometry where the semiconductor neutron detector counts were recorded but without the phantom. The tangential beam port of the KSU Triga Mark II Nuclear reactor was used for the irradiation of the gold foil. The theories needed for this measurement are discussed in the next sections.

4.1.2.1 Theory

Naturally occurring gold consists 100% of the isotope ^{197}Au . Gold is commonly used for flux measurement since it has an appreciable thermal neutron absorption cross-section (98.7 barns). After capture of a neutron ^{197}Au becomes ^{198}Au and emits a 411.8 keV [Baum and others, 2002] gamma ray with a frequency of $f = 95.5\%$. The 2.69 d half-life of ^{198}Au is also convenient.

Activation of a gold foil by a neutron spectrum will be due to the entire neutron population of both thermal and fast neutrons. It is possible to measure separately thermal and epithermal neutron fluxes by exposing one foil to the neutron flux and exposing the same or a different foil covered with 20 or 30 mils (1 mil = 0.001 inch or 0.00254 cm) of cadmium (Cd), which will effectively block out the neutrons below the “Cadmium cut off energy” of 0.4 eV. Thus, the Cd-covered gold foil will primarily be activated by epithermal neutrons.

Interaction of neutrons in the gold foil will activate the gold foil and the activation rate can be written as [Knoll, 2000]

$$M = \sum_{act} \phi V, \quad (4.9)$$

where \sum_{act} is the activation cross section averaged over the foil surface, ϕ is the neutron flux averaged over the foil surface, and V is the volume of the foil. As soon as the activation in the foil occurs, radioactive elements are produced which starts the radioactive decay process. Thus,

$$\frac{dN}{dt} = M - (\text{Rate of loss of } N). \quad (4.10)$$

The rate of loss equals is proportional to the number of nuclei N within the sample at that time. The constant of proportionality λ is the probability per unit time that a radioactive nucleus of interest will decay, which is also commonly known as the decay constant. Therefore

$$\text{Rate of loss of } N = \lambda N. \quad (4.11)$$

Thus Eq. (4.11), can be written as

$$\frac{dN}{dt} = M - \lambda N. \quad (4.12)$$

Now considering at $t = 0$, $N = 0$, the solution of Eq. (4.12) is

$$N(t) = \frac{M}{\lambda} (1 - e^{-\lambda t}) . \quad (4.13)$$

If t_0 is the irradiation time, then the activity after t_0 is

$$A(t_0) = \lambda N(t_0) = M (1 - e^{-\lambda t_0}) . \quad (4.14)$$

The rate of production can also be written as

$$M = \sum_{act} \phi V = N \bar{\sigma}_a \phi V = \frac{N_a \rho V}{A} \bar{\sigma}_a \phi , \quad (4.15)$$

where N is the atom density of gold, $\bar{\sigma}_a = \frac{\sigma_{a0}}{1.128}$ is the average microscopic thermal neutron absorption cross section, N_a is Avogadro's number, ρ is the density of gold, and A is the atomic mass of gold. The count rate R_γ at t_0 will be proportional to the activity of the ^{198}Au isotope

$$R_\gamma \propto \frac{N_a \rho V \phi \sigma_{a0}}{A(1.128)} [1 - e^{-\lambda t_0}] . \quad (4.16)$$

The proportionality constant is the product of the frequency of the gamma-ray emission, f , and the detector efficiency, ε . The activity will exponentially decay after irradiation. If counting begins after a waiting time t_w , and then the radioactive sample is counted for counting time t_c then

$$R_\gamma = \frac{\varepsilon f}{\lambda} \frac{N_a \rho V \phi \sigma_{a0}}{A(1.128)} [1 - e^{-\lambda t_0}] e^{-\lambda t_w} [1 - e^{-\lambda t_c}] . \quad (4.17)$$

Rearranging equation (4.17) and using Eq. (4.15), the rate of production can be written as

$$M = \frac{\lambda R_\gamma}{\varepsilon f [1 - e^{-\lambda t_0}] e^{-\lambda t_w} [1 - e^{-\lambda t_c}]} . \quad (4.18)$$

Equation (4.18) can be used to calculate the production rate of neutrons at the location of the irradiation. Irradiation of the bare foil will provide information related to thermal and epithermal neutrons and the Cd-covered foil is related primarily to the production rate of epithermal neutrons.

The flux distribution is assumed Maxwellian in the thermal region and “1/E” in the epithermal region. Therefore the thermal flux is defined as

$$\phi(E) = \phi_M(E, T) = \phi_t \frac{E}{E_T^2} e^{-\left(\frac{E}{E_T}\right)}; \quad 0 \leq E \leq E_{Tc}, \quad (4.19)$$

where $E_T = kT$ ($k = 8.617343 \times 10^{-5}$ eV K⁻¹ is the Boltzmann constant and $T = 293.41$ K) is the most probable neutron energy for thermal neutrons. The epithermal flux of neutrons is given as

$$\phi(E) = \frac{\phi_0}{E}; \quad E_{Tc} \leq E \leq E_{\max}. \quad (4.20)$$

Also the total thermal flux can be written as

$$\phi_T \cong \int_0^{E_{Tc}} \phi(E) dE = \int_0^{E_{Tc}} \phi(E, T) dE, \quad (4.21)$$

and the total fast flux can be written as

$$\phi_F \cong \int_{E_{Tc}}^{E_{\max}} \phi(E) dE = \int_{E_{Tc}}^{E_{\max}} \frac{\phi_0}{E} dE, \quad (4.22)$$

where, $E_{\max} = 20$ MeV and $E_{Tc} = 0.2$ eV.

Substituting the value of E_{\max} and E_{Tc} into Eq. (4.22) the fast flux is

$$\phi_F = \ln\left(\frac{20 \times 10^6}{0.2}\right) \phi_0 \cong 18 \phi_0. \quad (4.23)$$

Now, the activation rate in the gold foil when irradiated with a flux of $\phi(E)$ is

$$M_b = V_b \int \Sigma_a(E) \phi(E) dE, \quad (4.24)$$

where V_b is the volume of the bare gold foil. Eq. (4.24) can also be written as

$$M_b = \frac{N_a m_b}{A} \int_0^{\infty} \sigma_a(E) \phi(E) dE, \quad (4.25)$$

where A is the atomic weight of gold and m_b is the mass of the bare gold foil. As gold is $1/v$ absorber at thermal energies and has a resonance at about 4.9 eV, the microscopic absorption cross section can be written as

$$\sigma_a(E) = \sigma_a(E_0) \sqrt{\frac{E_0}{E}} = \sigma_{a0} \sqrt{\frac{E_0}{E}}; \quad 0 < E < E_{Tc}, \quad (4.26)$$

Using Eqs. (4.21), (4.22) and (4.26), Eq. (4.25) can be written as

$$M_b = \frac{N_a m_b}{A} \left[\int_0^{E_{Tc}} \sigma_{a0}(E) \sqrt{\frac{E_0}{E}} \phi(E, T) dE + \int_{E_{Tc}}^{E_{\max}} \sigma_a(E) \frac{\phi_0}{E} dE \right]. \quad (4.27)$$

The average thermal cross section is defined as

$$\bar{\sigma}_a = \frac{\int_0^{E_{Tc}} \sigma_{a0}(E) \phi_M(E, T) dE}{\int_0^{E_{Tc}} \phi_M(E, T) dE}. \quad (4.28)$$

Equation (4.28) can be written as

$$\bar{\sigma}_a \phi_t = \int_0^{E_{Tc}} \sigma_{a0}(E) \phi_M(E, T) dE. \quad (4.29)$$

Substituting from Eq. (4.29) into Eq. (4.27) yields

$$M_b = \frac{N_a m_b}{A_d} \left[\bar{\sigma}_a \phi_t + \int_{E_{Tc}}^{E_{\max}} \sigma_a(E) \frac{\phi_0}{E} dE \right]. \quad (4.30)$$

The integral of Eq. (4.30) can also be written as

$$\int_{E_{Tc}}^{E_{\max}} \sigma_a(E) \frac{\phi_0}{E} dE = \phi_0 \sigma_{a0} \int_{E_{Tc}}^{E_{CC}} \sqrt{\frac{E_0}{E}} \frac{1}{E} dE + \phi_0 \int_{E_{CC}}^{E_{\max}} \frac{\sigma_a(E)}{E} dE. \quad (4.31)$$

Equation (4.31) can be written as

$$\int_{E_{Tc}}^{E_{\max}} \sigma_a(E) \frac{\phi_0}{E} dE = \phi_0 \sigma_{a0} \sqrt{4E_0} \left[\frac{1}{\sqrt{E_{Tc}}} - \frac{1}{\sqrt{E_{CC}}} \right] + \phi_0 \int_{E_{CC}}^{E_{\max}} \frac{\sigma_a(E)}{E} dE. \quad (4.32)$$

Therefore Eq. (4.30) can be written as

$$M_b = \frac{N_a m_b}{A_d} \left[\bar{\sigma}_a \phi_t + \phi_0 \bar{\sigma}_a \sqrt{\frac{16E_T}{\pi}} \left\{ \frac{1}{\sqrt{E_{Tc}}} - \frac{1}{\sqrt{E_{CC}}} \right\} + \phi_0 \int_{E_{CC}}^{E_{\max}} \frac{\sigma_a(E)}{E} dE \right]. \quad (4.33)$$

Equation (4.33) gives the activation rate in bare gold foil.

4.1.2.1.1 Activation with Cd-Covered Gold Foil

The activation for Cd-covered gold foil can be written as [Dunn, 2005]

$$M_c = \frac{N_a m_c}{A_d} \left[\phi_0 \int_{E_{cc}}^{E_{\max}} \frac{\sigma_a(E)}{E} dE \right]. \quad (4.34)$$

The integral term in the above equation is known as the resonance integral and the value of the integral for gold is [ANL 5800, 1963]

$$I_d = \int_{E_{cc}}^{E_{\max}} \frac{\sigma_a(E)}{E} dE = 1558 \text{ b}. \quad (4.35)$$

Using Eq. (4.35), Eq. (4.34) can be written as

$$M_c = \frac{N_a m_c}{A_d} \phi_0 I_d. \quad (4.36)$$

The masses of the two foils can be different. Therefore the specific activation rate for the bare gold foil is

$$\hat{M}_b = \frac{M_b}{m_b}, \quad (4.37)$$

and for the Cd-covered gold foil is

$$\hat{M}_c = \frac{M_c}{m_c}, \quad (4.38)$$

where, m_b is the mass of the bare gold foil and m_c is the mass of the Cd-covered gold foil. Therefore the difference between the responses from bare and Cd-covered gold foil will provide the information about the productions rate of epithermal neutrons in the gold foil

$$\hat{M}_b - \hat{M}_c = \frac{N_a \bar{\sigma}_a}{A_d} \left[\phi_t + \phi_0 \sqrt{\frac{16 E_T}{\pi}} \left\{ \frac{1}{\sqrt{E_{TC}}} - \frac{1}{\sqrt{E_{CC}}} \right\} \right]. \quad (4.39)$$

The typical values of different energy parameters of the above equation are [Dunn, 2005],

$$E_T = 0.03 \text{ eV}, \quad E_{TC} = 0.2 \text{ eV}, \quad E_{CC} = 0.4 \text{ eV}. \quad (4.40)$$

Substituting the values from Eq. (4.40) into Eq. (4.39)

$$\hat{M}_b - \hat{M}_c = \frac{N_a \bar{\sigma}_a}{A_d} [\phi_t + 0.256 \phi_0]. \quad (4.41)$$

4.1.2.1.2 The Cadmium Ratio

The cadmium ratio is defined as

$$CR = \frac{\hat{M}_b}{\hat{M}_c}. \quad (4.42)$$

Using Eq. (4.33) and Eq. (4.36) the cadmium ratio can be written as

$$CR = \frac{\frac{N_a}{A_d} \left[\bar{\sigma}_a \phi_t + \phi_0 \bar{\sigma}_a \sqrt{\frac{16 E_T}{\pi}} \left[\frac{1}{\sqrt{E_{TC}}} - \frac{1}{\sqrt{E_{CC}}} \right] + \phi_0 I_d \right]}{\frac{N_a}{A_d} \phi_0 I_d}. \quad (4.43)$$

The simplified form of Eq. (4.43) is

$$CR = 1 + \frac{\bar{\sigma}_a}{I_d} \left[\frac{\phi_t}{\phi_0} + \sqrt{\frac{16E_T}{\pi}} \left\{ \frac{1}{\sqrt{E_{TC}}} - \frac{1}{\sqrt{E_{CC}}} \right\} \right]. \quad (4.44)$$

Substituting the values from Eq. (4.40), Eq. (4.44) can be written as

$$CR = 1 + \frac{\bar{\sigma}_a}{I_d} \left[\frac{\phi_t}{\phi_0} + 0.256 \right]. \quad (4.45)$$

The thermal and epithermal fluxes can be calculated using Eq. (4.41) and Eq. (4.45). In these two equations no corrections factors for flux depression or self-shielding were considered.

If cadmium is a perfect filter, it will block all the thermal neutrons and pass all the epithermal neutrons. But a real Cd-filter will pass some thermal neutrons of energy $< E_{CC}$ and some epithermal neutrons of energy $> E_{CC}$ will be absorbed. Therefore, there is an introduction of cadmium filter correction factor [Dunn, 2005]

$$F_{cd} = \frac{M_{epi}}{M_c}, \quad (4.46)$$

where M_{epi} and M_c are the activation rates due to epithermal response in a bare foil and epithermal response in a cadmium covered foil, respectively. Let, α be the probability that a 4.91 eV neutron passes through a cadmium cover of thickness, t_c .

Equation (4.46) can be rewritten as,

$$F_{cd} = \frac{M_{epi}}{\alpha M_{epi}} = \frac{1}{\alpha}. \quad (4.47)$$

For a beam incident normally on a cadmium covered foil with resonance energy $E_\gamma = 4.91$ eV,

$$\alpha = e^{-\tau_c}, \quad (4.48)$$

where

$$\tau_c = \sum_{cd}(E_r) t_c. \quad (4.49)$$

Now, for a beam incident normally on the cadmium covered foil, the cadmium correction factor can be written as

$$F_{cd} = e^{\tau_c}. \quad (4.50)$$

Therefore the cadmium-covered activation rate can be modified by

$$M_{epi} = F_{cd} M_c, \quad (4.51)$$

Similarly the specific epithermal production rate can be expressed as

$$\hat{M}_{epi} = F_{cd} \hat{M}_c. \quad (4.52)$$

4.1.2.1.3 Flux Perturbation and Self-Shielding

The flux in the foil is perturbed because of the absorption of neutrons within the foil, which is also known as self-shielding. Therefore the average neutron flux in the foil can be written as

$$\bar{\phi} = \left(\frac{\bar{\phi}}{\phi_s} \right) \left(\frac{\phi_s}{\phi_\infty} \right) \phi_\infty, \quad (4.53)$$

where ϕ_∞ is the unperturbed flux, ϕ_s is the flux at the surface of the foil, $\bar{\phi}$ is the average flux within the foil. From Eq. (4.54), the unperturbed flux can be written as

$$\phi_\infty = \frac{1}{F_1 F_2} \bar{\phi}, \quad (4.54)$$

where F_1 is the self-shielding correction factor,

$$F_1 = \frac{\bar{\phi}}{\phi_s}, \quad (4.55)$$

and F_2 is the depression factor,

$$F_2 = \frac{\phi_s}{\phi_\infty}. \quad (4.56)$$

For a perpendicular beam incident on the large edge of the foil, the depression factor is

$$F_2 = \frac{\phi_s}{\phi_\infty} \cong 1. \quad (4.57)$$

The self-shielding factor is different for thermal and epithermal neutrons.

4.1.2.1.4 Self-Shielding for Thermal Neutrons

For gold foil it can be assumed that the absorption cross section is much larger than the scattering cross section, therefore $\Sigma_a \gg \Sigma_s$. Therefore the flux as a function of position can be written as

$$\phi(x) = \phi_s e^{-\bar{\Sigma}_a x}, \quad (4.58)$$

where, x is the distance into the foil. If the foil is very thin, the spectrum is not hardened significantly within the foil. Therefore the self-shielding correction factor can be written as

$$F_1 = \frac{\bar{\phi}}{\phi_s} = \frac{1}{\phi_\infty} \frac{\int_0^t \phi(x) dx}{\int_0^t dx} = \frac{\phi_s}{\phi_\infty t} \int_0^t e^{-\bar{\Sigma}_a x} dx = \frac{1 - e^{-\bar{\Sigma}_a t}}{\bar{\Sigma}_a t}, \quad (4.59)$$

where t is the thickness of the gold foil.

4.1.2.1.5 Self-Shielding for Epi-Thermal Neutrons

Assuming that the absorption of neutrons in the epithermal regions are dominated by the resonance at energy $E_\gamma = 4.91$ eV, the self-shielding factor in the epithermal region is

$$F_1 = e^{-\Sigma_{ar}^{\max} t} \left[I_0 \left(\frac{\Sigma_{ar}^{\max} t}{2} \right) + I_1 \left(\frac{\Sigma_{ar}^{\max} t}{2} \right) \right], \quad (4.60)$$

Where I_0 and I_1 are the modified Bessel functions of the first kind of order zero and one respectively, t is the foil thickness, and $\Sigma_{ar}^{\max} = N_t \sigma_{ar}^{\max}$. The value of $\sigma_{ar}^{\max} \cong 30,600$ b at 4.91 eV resonance.

4.1.2.2 Experimental Procedure

The objective of this experiment was to determine the thermal and fast neutron flux at the point of interest where the SND counts were to be recorded. The experiment was performed at the tangential beam port (SE port) of the KSU TRIGA MARK II Nuclear Reactor. The Au foils were placed at a distance of 1 meter from the beam port.

The gold foils were washed with deionized water and the masses for each sample were measured and recorded. Then the bare-Au foil was inserted in a plastic bag and was hung at the same position as the semiconductor neutron detector would later be placed. The foil was irradiated at full power (nominally 240 kW) for three hours. The other gold foil was inserted inside a cadmium cover and then placed in a plastic bag. The Cd-covered gold foil with the plastic bag was hung at the same location as the bare foil was placed. The Cd-covered gold foil was irradiated also for three hours at full power of the reactor. After each irradiation was completed the sample was taken to the NAA lab (in Kansas State University) for counting. The masses of the Au foil samples and other

pertinent are recorded in Table 4.2. The area under the 411.8 keV peak from the spectrum of each of the bare and Cd-covered foils was used for the estimation of the thermal and epithermal fluxes on the surface of the torso phantom.

Table 4.2. The Mass, Thickness, Diameter, Irradiation Time, Wait Time and Count Time for Bare and Cd-covered Gold Foils.

Type of foils	Mass (gm)	Thickness (cm)	Irradiation time, t_0 (hour)	Wait time, t_w , (hour)	Count time, t_c (hour)
Bare	0.02610	0.00153	3	3.2	1
Cd-covered	0.04180	0.00245	3	3.1	3

4.1.2.3 Results

The thermal and epithermal fluxes from the tangential beam tube at nominal full power were calculated. The average thermal flux is $(\phi_\infty)_t = 6.96 \times 10^6 \pm 0.58 \times 10^6 \text{ cm}^{-2} \text{ s}^{-1}$ and for 1 kW of reactor power $(\phi_\infty)_t = 2.9 \times 10^4 \pm 0.24 \times 10^4 \text{ cm}^{-2} \text{ s}^{-1} \text{ kW}^{-1}$ and the epithermal flux is $(\phi_\infty)_{epi} = 1.85 \times 10^6 \pm 0.0016 \times 10^6 \text{ cm}^{-2} \text{ s}^{-1}$ and for 1 kW of reactor power $(\phi_\infty)_{epi} = 7.71 \times 10^3 \pm 0.0067 \times 10^3 \text{ cm}^{-2} \text{ s}^{-1} \text{ kW}^{-1}$. The detailed description of the calculation is provided in Appendix D.

4.2 Measurement of Dose on the Surface of the Anthropomorphic Phantom

Thermoluminescent dosimeters were used to estimate the dose on the surface of the anthropomorphic phantom. To estimate the dose of the irradiated TLDs on the surface of the phantom, it was necessary to know the dose calibration curve i.e., dose vs. deposited charge in the TLDs. The gamma-ray portion of this was accomplished by irradiating TLDs using a Panoramic Irradiator (which contains ^{137}Cs source) and then the deposited charge was read out using a TLD reader (Harshaw Chemical Company, model 2000). Then the charge was plotted against the calculated dose. The next few sections will discuss thermoluminescence dosimeters and their characteristics, the TLD reader and annealing of TLDs.

4.2.1 Thermoluminescent Dosimeters and Their Characteristics

Thermoluminescent dosimeters are made from thermoluminescent (TL) material, within which electrons and holes are produced when exposed to a radiation field. These electrons and holes are trapped in the lattice defects of the crystal structure; if the traps are far enough in energy from the conduction band they remain in the trap. But if the exposed material is heated at sufficient temperature the trapped electrons are released and raised to the conduction band. The electrons eventually combine with the holes emitting visible light, which is known as thermoluminescence. Holes can also be trapped in a similar process and combined with an electron and produce visible light. The total amount of light is proportional to the amount of energy absorbed from the radiation and hence provides a measure of total absorbed dose. TLDs can be reused by emptying all the traps with heating for a long time, which is also known as annealing (Section: 4.2.1.3).

Good TLDs should have a large linear dose range, a significant amount of light output, and an ability to retain the trapped electrons for a long period of time [Tsoulfanidis, 1983]. Lithium fluoride is one of the materials with all these requirements and is commercially available. Lithium fluoride TLDs can be used to determine the dose rate due to thermal neutrons and to gammas. Because there are no TLDs available that are sensitive to only thermal neutrons, a pair of TLDs is formed to determine the thermal neutron dose. A TLD-600 and TLD-700 pair was used in the recent study. The material, relative Li concentration, and sensitivity are described in Table 4.3 The useful range for these TLDs are 10 μ Gy-10 Gy and the dimensions are 3.2 \times 3.2 \times 0.89 mm. The ^6Li has higher thermal neutron cross-section (940 b) whereas ^7Li has very small cross-section for thermal neutrons (71 b) [Lamarsh, 2002]. Therefore TLD-600 responses are for both neutron and gamma radiation and TLD-700 responses measure dose essentially only for gamma radiation.

Table 4.3. Properties of TLD-600, TLD-700 used in the Experiment.

Material	Detector Type	Relative Li concentration	Sensitivity
⁶ LiF: Mg, Ti	TLD-600	⁶ Li = 95.62% ⁷ Li = 4.38%	Thermal neutron, Gamma
⁷ LiF: Mg, Ti	TLD-700	⁶ Li = 0.007% ⁷ Li = 99.993%	Gamma

4.2.1.1 Thermal Neutron Response Using TLDs

The thermal neutron response is estimated by subtracting the TLD-700 responses from the TLD-600. From the above discussion it can be concluded that in a mixed neutron and photon field, the TLD-600 response is [Velyhan and others (2006)]

$$R_{600}^{n+\gamma} = R_{600}^n + R_{600}^{\gamma}, \quad (4.61)$$

and the TLD-700 response is

$$R_{700}^{n+\gamma} = R_{700}^{\gamma}. \quad (4.62)$$

The ratio of the two TLD responses in a gamma only field can be expressed as

$$k = \frac{R_{600}^{\gamma}}{R_{700}^{\gamma}}. \quad (4.63)$$

The value of k can be determined by exposing the TLDs to γ -ray from sources such as ¹³⁷Cs or ⁶⁰Co [Velyhan and others (2006)]. Therefore the response due to the thermal neutrons can be expressed as

$$R_{600}^n = R_{600}^{n+\gamma} - kR_{700}^{n+\gamma}. \quad (4.64)$$

4.2.1.2 TLD Reader

The basic function of TLD readers are to heat the dosimeters at a constant rate and to detect the light emitted by the material. A low noise and high gain photomultiplier tube (PMT) is used to convert the light into a current signal. Then the signal is amplified and displayed. The heater, TLD, and photomultiplier tube are enclosed in a light tight box and connected to a pure (99.9999%) nitrogen tank (see Figure 4.6). A nitrogen

atmosphere is created to eliminate spurious luminescence, which is caused by oxygen. This is also known as nitrogen quenching.

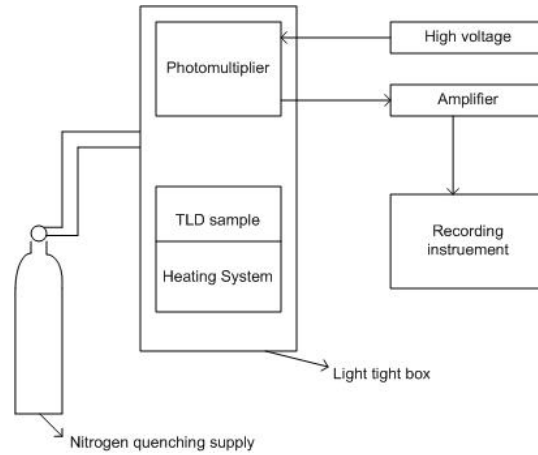


Figure 4.6. TLD Reader Block Diagram.

4.2.1.3 Annealing of TLDs

Annealing after irradiation is a heating process followed by cooling of the thermoluminescence material. Through annealing, the trapping centers of the residual charges are removed and thermoluminescent materials are returned to their background state [Driscoll and others, 1986]. Annealing is performed at high temperature for a relatively short time.

Annealing usually takes place in a conventional oven and is different for different TLD materials. The annealing procedure for TLDs containing ${}^6\text{LiF}$ and doped with Mg and Ti (${}^6\text{LiF}:\text{Mg, Ti}$) is: 1 h at 400°C followed by 20 h at 80°C (or 2 hours at 100°C). The TLDs should cool down at a constant rate after annealing with high temperature and before being placed in a low temperature. High temperature annealing is important for higher dose levels above about 1 Gy [Horowitz (1990)]. The present experiment did not involve higher dose levels and therefore the annealing procedure was performed using the TLD reader. After recording the charge of the irradiated TLDs, the TLDs were read two times and if the second reading is less than 2% of the first then the dosimeter is considered annealed. If the difference is greater than 2%, the procedure is continued [Harshow Instruction Manual].

4.2.1.4 Experimental Procedure

To establish the calibration curve (charge with respect to a known dose) for TLD 600 and TLD 700, these two TLDs need to be exposed in a known radiation field. A Panoramic Irradiator, which contains a ^{137}Cs source with a known source strength, was used to irradiate the TLDs. Before the irradiation procedure the TLDs were annealed using the TLD reader by re-reading the dosimeters a couple of times or until the reading is close to background. The initial charge of each TLD was recorded. Five TLDs were placed at five positions (20, 30, 40, 50 and 60 cm) from the source. The irradiation time was 40 minutes. The irradiated TLDs were read in the TLD reader with a temperature setting of T_1 (initial temperature) = 135°C , T_2 (final temperature) = 265°C and rate of temperature increment, $T_{\text{rate}} = 10^\circ\text{C s}^{-1}$ and the corresponding charges were recorded. The initial charge of each TLD was subtracted from the final charge.

4.2.1.5 Results and Discussion of Results

The dose rate was calculated using the following equation [Shultis and Faw (2000)]

$$D = \left(\frac{S_p}{4\pi r^2} \right) (\mathfrak{R}) \text{ Sv s}^{-1}, \quad (4.65)$$

where S_p is the source strength (photons s^{-1}), r is the source-to- dosimeter distance in cm, and \mathfrak{R} is the response function in Sv cm^2 . The response function used in this case was for a parallel beam with AP incidence on the anthropomorphic torso phantom. The detailed calculation of the dose for TLD-600 and TLD-700 is discussed in Appendix E.

The dose calibration curve for TLD-600 and TLD-700 are shown in Figure 4.7 and Figure 4.8, respectively. The circles represent the data points and the solid line is a linear fit to the data points of the form

$$y = a + bx, \quad (4.66)$$

where, y is the charge and x represents the corresponding dose. The curve fit equation parameters for TLD-600 were $a = -0.0188$ and $b = 0.5766$, and for TLD-700 were $a = 0.0012$ and $b = 0.6476$. The corresponding k values are shown in Figure 4.9.

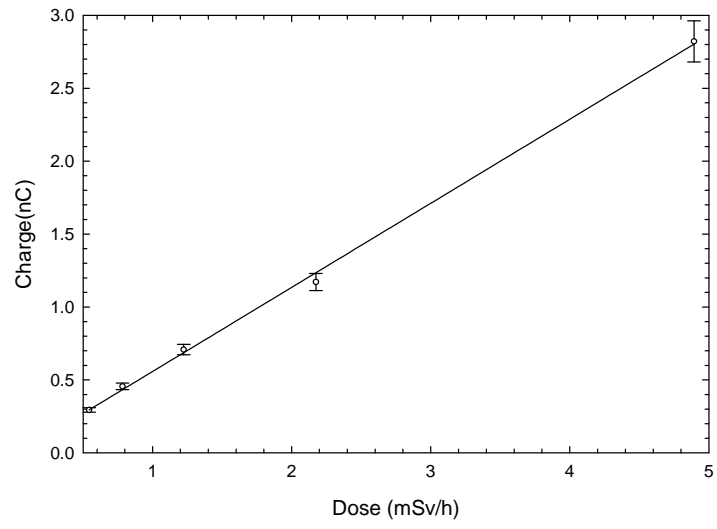


Figure 4.7. Calibration Curve for TLD-600.

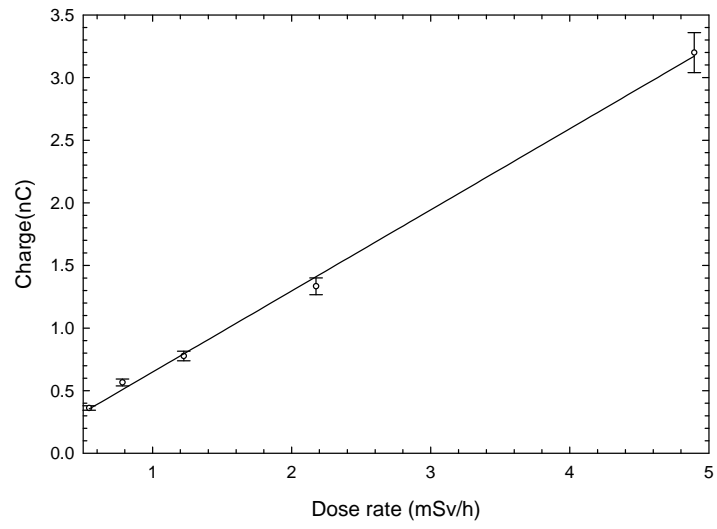


Figure 4.8. Calibration Curve for TLD-700.

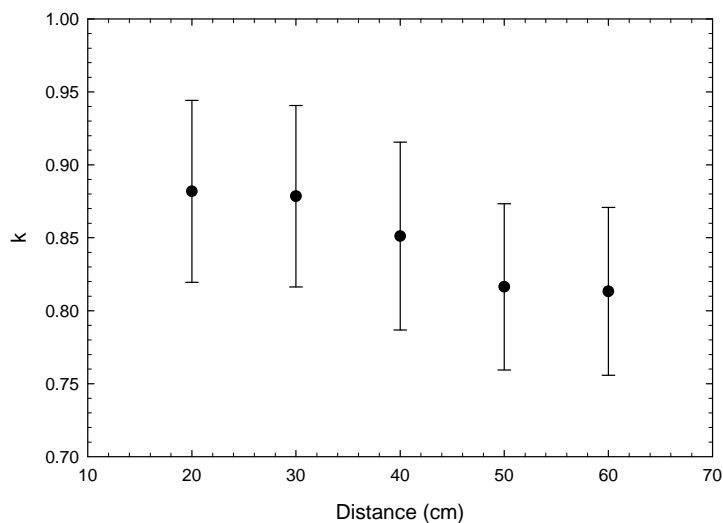


Figure 4.9. The value of $k = \frac{R_{600}^{\gamma}}{R_{700}^{\gamma}}$ at Various Distances from the Source.

The k value was determined to be the average of the readings at the five different distances, $k = 0.8486 \pm 0.03$.

4.2.2 Anthropomorphic Torso Phantom and TLDs

The descriptions of the anthropomorphic phantom (named Harold or Harry for short) that was used for dosimeter characterization are discussed in section: 2.5.3. Therefore for the rest of this section the anthropomorphic torso phantom will be replaced by Harry. The TLDs were used to convert the counts of the neutron dosimeter into dose on Harry. A pair of TLD-600 and TLD-700 dosimeters was used. The experiment was performed at the tangential beam port of the KSU TRIGA Mark II Nuclear Reactor. A shutter was used in the open beam port and a beam catcher was placed at a distance of 3.32 m away from the shutter. The position of Harry was 1 m from the shutter end and a TLD pair (TLD-600 and TLD-700) was placed in the middle of the front of Harry. The TLD pair was irradiated at a reactor power of 100 kW for 1.5 hours. The same experimental procedure was repeated with a cadmium sheet between the TLD pair and Harry. The TLD responses was read-out using Harshaw 2000-C model reader at a heating ramp rate of $10^{\circ} \text{C s}^{-1}$ from 135°C to 265°C in an nitrogen atmosphere.

4.2.2.1.1 Results

Bare and Cd-filtered TLD pair responses on Harry are recorded in Table 4.4 and Table 4.5 respectively. The initial charge (IC) for each TLD was recorded before the experiment and recorded in column 2. The charge after the irradiation (C) for each TLD was recorded in column 3, and finally the final charge (C – IC) for each TLD is recorded in column 4.

Table 4.4. Bare TLD Responses on the Surface of Harry.

	Initial Charge (IC), nC	Charge After Irradiation (C), nC	Final Charge Deposited, (C - IC), nC
TLD 700	0.07	2.60	2.53
TLD 600	0.08	891.80	891.73

Table 4.5. Cd-filtered TLD Responses on the Surface of Harry.

	Initial Charge (IC), nC	Charge After Irradiation (C), nC	Final Charge Deposited, (C-IC), nC
TLD 700	0.08	23.80	23.72
TLD 600	0.08	822.20	822.12

Therefore from Table 4.4 and Table 4.5, the bare and Cd-filtered TLD-600 response on Harry for 100 kW of reactor power was calculated, using the Eq. (4.65) and the k value.

The bare TLD-600 response is

$$\left(R_{600}^n\right)_{bare} = 889.56 \text{ nC}, \quad (4.67)$$

and the Cd-filtered TLD-600 response is

$$\left(R_{600}^n\right)_{Cd-covered} = 801.76 \text{ nC}. \quad (4.68)$$

The corresponding neutron dose for both bare and Cd-filtered TLD responses was calculated using Eq. (4.66), therefore

$$\left(D_{600}\right)_{bare} = 1542.91 \text{ mSv h}^{-1}, \quad (4.69)$$

and

$$\left(D_{600}\right)_{Cd-covered} = 1390.53 \text{ mSv h}^{-1}, \quad (4.70)$$

4.2.3 Testing of Semiconductor-Based Neutron Dosimeter with the Phantom

4.2.3.1 Semiconductor-Based Neutron Dosimeter

The basic detector design of the semiconductor neutron dosimeter was discussed in section 3.2. The neutron reactive material in the actual dosimeter is ${}^6\text{LiF}$ instead of ${}^{10}\text{B}$ which was used in the Monte Carlo simulation study. Generally small holes are etched into the front surface of the semiconductor (Si) substrate, and then neutron reactive material was used to fill the holes and to cover the top surface (with a cap thickness of ${}^6\text{LiF}$) [McGregor and et. al. 2002]. The device characterized in this study has the following characteristics: the diameter of the active diode (Si) is 6 mm and the diameter of the neutron reactive coating is 5.6 mm, each hole is 30 μm in diameter and 76.6 μm deep and the cap thickness is 39.5 μm . The dosimeter package is portable and battery-operable. The counts created in the detector were collected and passed to an amplifier, then to discriminator and digital conversion unit, and finally to counter/display components. The block diagram of the operation of the dosimeter package is described in Figure 4.10.

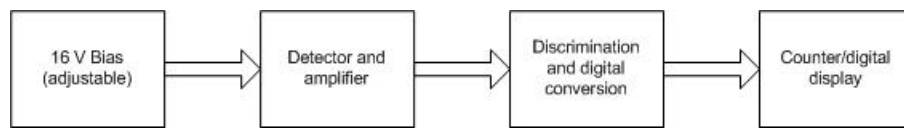


Figure 4.10. Block Diagram of Dosimeter Package.

4.2.3.2 Experimental Procedure

Before placing the semiconductor neutron dosimeter on Harry for the experiment, the linearity of the dosimeter was observed. The dosimeter counts were recorded for two minutes and for reactor powers of 10, 50, 100, 200 and 500 watt. The counts were recorded for two orientations of the dosimeter with respect to the beam port: i) facing the dosimeter display toward the beam port and ii) facing the opposite side of the display toward the beam port. The recorded counts are shown in Table 4.6. It can be observed that the dosimeter count is considerably higher facing the dosimeter display to the beam port than facing the dosimeter display back to the beam port. Therefore the dosimeter

reading for the rest of the experiment was performed by facing the dosimeter display to the neutron beam. It was also observed that the dosimeter reading was increasing with increasing reactor power, which illustrated that the dosimeter response is linear.

Each time the dosimeter was turned on, it provided some initial arbitrary reading. Thus during some experiment it was decided not to turn off the dosimeter and the end count of one reading is the arbitrary start count for the next reading. The net count for each measurement was estimated by subtracting the arbitrary start count from the final count.

The counts of the neutron dosimeter were observed after placing the dosimeter on Harry with display facing the beam. A shutter was used in the beam port and a beam catcher was placed at a distance of 3.32 m away from the shutter. Harry was positioned at 1 m from the shutter and the dosimeter was placed in the middle of Harry (which is the middle of the torso of a standard male). The experimental arrangement is shown in Figures 4.11 and 4.12. The dosimeter was irradiated at a reactor power of 1 kW and for 5, 10 and 15 minutes. The same experimental procedure was repeated by filtering the dosimeter with a cadmium sheet between the dosimeter and Harry. The counts recorded using semiconductor neutron dosimeter is attached in Table 4.7.

Table 4.6. Dosimeter Counts, Dosimeter Display Facing Beam Port and Dosimeter Display Facing Back to Beam Port.

Reactor Power (Watt)	Dosimeter Display Facing to the Beam Port			Dosimeter Display Facing Back to the Beam Port		
	Arbitrary Start Count, I	Count After Irradiation, F	Net Count, $N = F - I$	Arbitrary Start Count I	Count After Irradiation, F	Net Count $N = F - I$
10	169	184	15	88	115	27
50	74	168	94	151	199	48
100	135	347	212	167	264	97
200	92	589	497	121	214	93
500	213	1087	874	91	358	267



Figure 4.11. Semiconductor-Based Neutron Dosimeter Experiment in the Beam Port.



Figure 4.12. Semiconductor-Based Neutron Dosimeter Placed in the Middle of Harry.

4.2.3.3 Results using Semiconductor-Based Neutron Dosimeter

The bare and Cd-filtered semiconductor neutron dosimeter counts are presented in Table 4.7. In both tables the arbitrary start count of the dosimeter is denoted by I and the count after irradiation is denoted by F . The net count, $N = F - I$, is the difference between the two counts. The net count for the bare dosimeter is denoted by N_b and for the Cd-filtered dosimeter is denoted by N_{Cd} . Because N is the total number of counts collected over a period of time, the standard deviations can be expected to be, for the bare dosimeter

$$\sigma_b = \sqrt{N_b}, \quad (4.71)$$

and for the Cd filtered dosimeter

$$\sigma_{Cd} = \sqrt{N_{Cd}}. \quad (4.72)$$

Let the difference between bare and Cd-filtered dosimeter counts be denoted by D , i.e.,

$$D = N_b - N_{Cd}. \quad (4.73)$$

The corresponding standard deviation is

$$\sigma_D = \sqrt{\sigma_b^2 + \sigma_{Cd}^2}. \quad (4.74)$$

Table 4.7. Bare and Cd-filtered SND Responses on Harry.

Type of Dosimeter	Irrad. Time (min)	Start Count I	Count After Irradiation F	Net Count, $N = F - I$	$\sigma_b = \sqrt{N_b}$	D	σ_D
Bare				N_b			
	5	72050	84583	12533	111.95		
	10	84584	109697	25113	158.47		
	15	10969	147181	37484	193.61		
Cd-filtered				N_{Cd}	$\sigma_{Cd} = \sqrt{N_{Cd}}$		
	5	43	12011	11968	109.40	565	156.53
	10	12011	35897	23886	154.55	1227	221.36
	15	35897	72050	36153	190.14	1331	271.36

From Table 4.7, it can be determined that the count rate for the bare dosimeter, is 42 counts s^{-1} and for the Cd-filtered dosimeter, is 40 counts s^{-1} , which are constant irrespective of the irradiation time.

The main purpose of the experimental study is to relate the dosimeter counts to the corresponding dose and to find a count-to-dose conversion factor. The dose on the surface of Harry was estimated at 100 kW of reactor power and presented in Eq. 4.70 and Eq. 4.71 for bare and Cd-filtered TLDs respectively. Therefore the doses for 1 kW of reactor power were

$$(D_{600})_{bare} = 15.43 \text{ mSv h}^{-1}, \quad (4.75)$$

and

$$(D_{600})_{Cd-filtered} = 13.91 \text{ mSv h}^{-1}. \quad (4.76)$$

For 1 kW of reactor power, the thermal neutron flux on the surface of Harry was

$$(\phi_{\infty})_t = 2.90 \times 10^4 \pm 0.24 \times 10^4 \text{ cm}^{-2} \text{ s}^{-1} \text{ kW}^{-1}, \quad (4.77)$$

and the epithermal neutron flux was

$$(\phi_{\infty})_{epi} = 7.71 \times 10^3 \pm 0.067 \times 10^3 \text{ cm}^{-2} \text{ s}^{-1} \text{ kW}^{-1}. \quad (4.78)$$

Now to find the count-to-dose conversion factor, the relationship between counts and dose for three different time periods (5, 10 and 15 minutes) on the surface of Harry are presented in Table 4.8. The count-to-dose conversion factor is calculated using the relationship

$$C = \frac{D}{N} \text{ (}\mu\text{Sv count}^{-1}\text{)}, \quad (4.79)$$

and the corresponding standard deviation was calculated using the following equation

$$\sigma_c = \sqrt{\left(\frac{\partial C}{\partial D}\right)^2 \sigma_D^2 + \left(\frac{\partial C}{\partial N}\right)^2 \sigma_N^2}. \quad (4.80)$$

The count-to-dose conversion factor and the associated standard deviation are presented in Table 4.9.

Table 4.8. Bare (N_b) and Cd-filtered (N_{Cd}) SND Counts on Harry, the Corresponding Dose and Count-to-Dose Conversion Factor.

Irrad. time (min)	N_b	Dose (μSv)	$C_b = \frac{D}{N}$ ($\mu\text{Sv count}^{-1}$)	N_{Cd}	Dose (μSv)	$C_{Cd} = \frac{D}{N}$ ($\mu\text{Sv count}^{-1}$)
5	12533	1285.76	0.1026	11968	1158.78	0.0968
10	25113	2571.51	0.1024	23886	2317.55	0.0970
15	37484	3857.27	0.1029	36153	3476.33	0.0962

Table 4.9. The Count-to-dose Conversion Factors and the Corresponding Standard Deviations

Irrad. time (min)	$C_b = \frac{D}{N}$ ($\mu\text{Sv count}^{-1}$)	σ_{C_b}	$C_{Cd} = \frac{D}{N}$ ($\mu\text{Sv count}^{-1}$)	$\sigma_{C_{Cd}}$
5	0.1026	0.005217	0.0968	0.004921
10	0.1024	0.005161	0.0970	0.004891
15	0.1029	0.005173	0.0962	0.004834

Finally, the average count-to-dose conversion factors for bare (C_b) and for Cd-filtered (C_{Cd}) SND responses are

$$C_b = 0.1026 \pm 0.003 \text{ } (\mu\text{Sv count}^{-1}), \quad (4.81)$$

and

$$C_{Cd} = 0.1026 \pm 0.0028 \text{ } (\mu\text{Sv count}^{-1}). \quad (4.82)$$

The count-to-dose conversion factors can be used to convert the recent SND-based dosimeter's readout in counts into dose units. The total dose is given by the response of a bare detector times C_b . Then, subtracting the dose as measured by a Cd-filtered detector response times C_{Cd} , a dose due to slowing in the phantom can be estimated. Values of this dose will depend on the neutron spectrum, and thus, in principle, provide some information about the neutron source.

5 Conclusion and Suggestions for Future Work

The simulation studies were completed before the SND-based dosimeter was constructed. At the time of the simulation study, the type of neutron reactive material and the exact diameter of the SND detector were not established. Therefore for the purpose of the simulation study, a notional detector design was considered. The simulated detector was 1cm in diameter and 0.005 cm in thickness and the neutron reactive material was ^{10}B . For the simulation study, the neutron reactive material was assumed to be uniformly distributed throughout the semiconductor substrate and the efficiency of the detector was considered 100%. The results can be scaled down according to the actual efficiency of an as-built detector.

The dosimeter used for the experimental study incorporated a perforated semiconductor neutron detector and the neutron reactive material was ^6LiF . In this detector design, the diameter of the SND was 6 mm and the diameter of the perforation was 5.6 mm. The exact efficiency of this detector at the time of the experiment was not known, but it can be assumed to be 5 and 25%. From the experimental study, it was observed that the bare dosimeter on the surface of Harry, produced 25,113 counts when exposed to the neutron beam for 10 minutes and the corresponding dose was estimated by TLD experiments to be 2.57 mSv. The Cd-filtered (Cd sheet between detector and Harry) dosimeter produced 23,886 counts when exposed to the neutron beam for 10 minutes and the corresponding dose was estimated to be 2.32 mSv. A parameter Spectrum Determination Constant (*SDC*) was introduced in Chap.3, which can only provides information about slow neutrons spectra if $SDC \cong 0.23$ and fast neutron spectra if the value of *SDC* is 0.39 to 0.46.

The experimental results were obtained for a detector that was different than the detector that was modeled. Nevertheless the results of the experimental study compare favorably with the model result of the anthropomorphic phantom for AP incidence of a neutron beam having a Watt energy spectrum. From the simulation study it was observed that the bare dosimeter produced 140,000 counts per mSv and the Cd-filtered dosimeter

produced 80,000 counts per mSv for 100% efficient detectors. Therefore bare detectors having 5-25% efficiency will produce 7,000 - 35,000 counts per mSv and Cd-filtered detectors will produce 4,000 – 20,000 counts per mSv. From the experimental results above, it is seen that the ^6LiF coated detector recorded 9,771 counts per mSv when bare and 10,296 counts per mSv when Cd-filtered. Therefore it can be concluded that the ^6LiF coated detector will produce at about 10,000 counts per mSv.

The *SDC* for the experimental study was determined 0.04, but can't draw a conclusion about the spectrum determination as the experimental study was performed only for thermal neutron beam port (which is a mixture of thermal and epithermal neutrons) of TRIGA Mark II Nuclear Reactor. But it is noticeable that the *SDC* is significantly smaller than the simulation study; obvious reason that the detector's neutron reactive material is different, and also the difference between bare and Cd-covered detector counts are not significant (~ 4%).

To extend this research study in future, the MCNP model can be developed for a ^6LiF dosimeter and the dosimeter responses can be observed on the Anthropomorphic Torso Phantom. The responses then can be compared with the recent experimental study of a ^6LiF dosimeter. The dosimeter device also can be made to read out directly in dose units using the count-to-dose conversion factors.

REFERENCES

- Attix, F. H., Rosech, W. C, and Tochilin, E (1996), *Radiation Dosimetry* (2nd ed.), Academic Press, New York, NY.
- Barlett, D. T., Tanner, R.J. and Thomas, D.J. (1999), Active Neutron Personal Dosimeters-a Review of Current Status, *Radiat. Prot. Dosim.* **vol. 86**, No.2, pp.107-122.
- ANL-5800 (1963), *Reactor Physics Constant*, 2nd ed. Argonne National Laboratory.
- Baum, E. M., Knox, H. D. and Miller, T. R. (2002), Chart of the Nuclides (16th ed.), KAPL, Inc., a subsidiary of Lockheed Martin.
- Breismeister, J. F., 2000. *MCNP – A General Monte Carlo N-Particle Transport Code*, Los Alamos National Laboratory, LA-12625-M, Version 4C.
- Cember, H. (1983), *Introduction to Health Physics* (2nd ed.), Pergamon Press, New York, NY.
- Chemtob, M., Dollo, R., Coquema, C., Chary, J. and Ginisty, C. (1995), Essais de dosimètres neutrons à bulles, modèle BD 100 R-PND et modèle BDT. *Radioprotection* **30**, 61-78.
- Data Spectrum (1995), Data Spectrum Corporation SPECT Anthropomorphic Torso Phantom User's Manual, *Data Spectrum Corporation, Hillsborough, NC*.
- Dunn, W. L. (2004), A Radio-optic Method for Measuring Relative Motion, *Nucl. Instrum. and Meth. in Phys. Res. B* **vol. 213**, pp. 481-485.
- Dunn, W. L. (2005), *Lecture Notes Nuclear Reactor Laboratory (NE 648)*, Department of Mechanical and Nuclear Engineering, Kansas State University, Manhattan, KS.
- Dunn, W.L., Quaji M. Jahan, Eric L. Patterson, J. Kenneth Shultis, Clell J. (C.J.) Soloman (2006), Design and Performance of a Portable Neutron Dosimeter, *Proc. Workshop on European Collaboration for Higher Education and Research in Nuclear Engineering and Radiological Protection, 13-15 March*, Universidad Politécnica de Valencia (UPV), Valencia, Spain.
- Eichholz, G. G. and Poston, J. W. (1979), *Principles of Nuclear Radiation Detection*, Ann Arbor Science Publishers, Inc., Ann Arbor, MI.

- Gersch, H. K., McGregor, D. S., and Simpson, P. A. (2001), A study of the Effect of Incremental Gamma-Ray Doses and Incremental Neutron Fluences Upon the Performance of Self-Biased ^{10}B -Coated High-Purity Epitaxial GaAs Thermal Neutron Detectors, *IEEE*, pp. 4-42:4-46.
- ICRU (1984), Stopping powers for electrons and positrons, *Report 37*, International Commission on Radiation Protection and Measurements, Bethesda, MD.
- ICRU (1985), Determination of Dose Equivalents Resulting from External Radiation Sources. *Report 39*, International Commission on Radiation Protection and Measurements, Bethesda, MD.
- ICRU (1992), Phantoms and computational Models in Therapy, Diagnosis and Protection, *Report 48*, International Commission on Radiation Protection and Measurements, Bethesda, MD.
- ICRU (2001), Determination of Operational Dose Equivalent Quantities for Neutrons, *Report 66*, International Commission on Radiation Protection and Measurements, Bethesda, MD.
- ICRP (1975), Reference Man: Anatomical, Physiological and Metabolic Characteristics, *ICRP Publication 23*, International Commission on Radiological Protection, Pergamon Press, Oxford, England.
- ICRP (1985), Protection of the Patient in Radiation Therapy, *ICRP publication 44*, vol. 15/2, International Commission on Radiological Protection, Elsevier, Canada.
- Ing, H. and Piesch, E. (1985), Status of Neutron Dosimetry, *Radiat. Prot. Dosim.*, **vol. 10**, No. 1-4, pp. 5-15.
- Harshaw, *Model 2000-A, -C, -P Thermoluminescence Detectors Instruction Manual*, The Harshaw Chemical Company.
- Jahan, Q., Patterson, E. Rice, B., Dunn, W.L., and McGregor, D.S. (2007), Neutron Dosimeters Employing High-efficiency Perforated Semiconductor Detectors, *Nucl. Instrum. and Meth. in Phys. Res. B*, **vol. 263**, pp 183-185.
- Jandel Scientific (1996), "Table Curve," San Mataso, CA.
- Knoll, G. F. (2000), *Radiation Detection and Measurement* (3rd ed.), John Wiley & Sons, Inc. New York, NY.

- Kramer, R., Zankl, M., Williams, G., and Drexler, G. (1982), The Calculation of Dose from External Photon Exposures Using Reference Human Phantoms and Monte Carlo Methods, Part I: The Male (Adam) and Female (Eva) Adult Mathematical Phantoms, *Report GSF-Bericht S-885*, Gesellschaft für Umweltforschung, Munich (Reprinted 1986).
- Lamarsh, J. R. (2002), *Introduction to Nuclear Reactor Theory*, Copyright-American Nuclear Society, LaGrange Park, IL.
- McGregor, D. S. and Shultis, J. K. (2004), Spectral identification of thin-film-coated and solid-form semiconductor neutron detectors, *Nucl. Instrum. and Meth. in Phys. Res. A* **vol. 517**, pp. 180-188.
- McGregor, D. S., Hammig, M. D., Gersch, H. K., Yang, Y-H., Klann, R. T. (2003), Considerations for Thin Film Coated Semiconductor Thermal Neutron Detectors, Part I: Basics Regarding Alpha Particle Emitting Neutron Reactive Films, *Nucl. Instrum. and Meth. in Phys. Res. A* **vol. 500**, pp.272-308.
- McGregor, D. S., Klann, R. T., Gersch, H. K., Ariesanti, E, Sanders, J. D. VanDerElzen, B. (2002), New Surface Morphology for Low Stress Thin-Film-Coated Thermal Neutron Detectors, *IEEE Transaction on Nuclear Science*, **vol. 49**, No. 4, pp. 1999-2004.
- McGregor, D. S., Klann, R. T., Gersch, H. K., Sanders, J. D. (2001), Designs for thin-Film-Coated semiconductor thermal neutron detectors, *Nuclear Science Symposium Conference Record IEEE*, 4-10 Nov., **vol. 4**, pp. 2454-2458.
- McLane, V., Dunford, C. L. and Rose, P. F. (1988), *Neutron Cross-Sections*, **Vol.2**, Academic-Press, San Diego, CA.
- NCRP (1971), Protection against Neutron Radiation, **Report 38**, National Council on Radiation Protection and Measurements, Bethesda, MD.
- NCRP (1987), Radiation Exposure of the U.S Population from Consumer Products and Miscellaneous Sources, **Report 95**, National Council on Radiation Protection and Measurements Washington, DC.
- NCRP (1993), Recommendation on limits for Exposure to ionizing Radiation, **Report 116**, National Council on Radiation Protection and Measurements, Bethesda, MD.

- Peurrung, A. J. (2000), Recent developments in neutron detection, *Nucl. Instrum. and Meth. in Phys. Res. A* **vol. 443**, 400-415.
- Schwartz, R. B. and Hunt, J. B. (1990), Measurement of the Energy Response of Superheated Drop Neutron Detectors. *Radiat. Prot. Dosim.* **vol. 34**, 377-380.
- Shultis, J.K, and Faw, R. E. (2000), *Radiation Shielding*, American Nuclear Society, LaGrange Park, IL.
- Shultis, J. K. and Faw, R. E. (2002), *Fundamental of Nuclear Science and Engineering* Marcel Dekker, Inc., New York, NY.
- Tsoufanidis, N. (1983), *Measurement and Detection of Radiation*, Hemisphere Publishing Corporation, New York, NY.
- Velyhan, A., Krása, J., Bienkowska, B., Ivanova-Stanik, I. M., Juha, L., Karpinski, L., Kyr, D., Králík, M., Kravárik, J., Kubeš, P., Paduch, M., Scholz, M and Tomaszewski, K., (2006), Use of thermoluminescent dosimeters for measurements of fast-neutron spatial-distribution at the plasma focus device PF-1000, *Physica Scripta* **vol. T123**, pp. 112-115.
- Zwillinger, Daniel (2003), *CRC Standard Mathematical Tables and Formula*, 31st ed., Chapman & Hall/ CRC Press, New York, NY.

Appendix A - Monte Carlo Simulation Code Input Files

A.1. Water Phantom

MCNP4C example code used to observe the detector responses for a parallel beam of Watt energy spectrum on the surface of the water phantom.

```
C Calculation of dose using the semiconductor neutron detector for water phantom c
c
c ***** cell cards *****
c ----- Detector at the origin -----
c ----- Detector 1 -----
c
1 3 -0.7683 -41 71 -72 imp:n=1 $ D1, boron cell
2 5 -8.69 -42 71 -74 imp:n=1 $ Cd on back, D1
c ----- Detector 2 -----
3 3 -0.7683 -42 74 -73 imp:n=1 $ D2, boron cell
c ----- Detector at 10 cm ----
4 3 -0.7683 -43 71 -72 imp:n=1 $ D1, boron cell
c ----- Detector 2 -----
5 5 -8.69 -44 71 -74 imp:n=1 $ Cd on back, D1
6 3 -0.7683 -44 74 -73 imp:n=1 $ D2, boron cell
c ----- Detector at 20 cm ----
c
7 3 -0.7683 -45 71 -72 imp:n=1 $ D1, boron cell
c ----- Detector 2 -----
8 5 -8.69 -46 71 -74 imp:n=1 $ Cd on back, D1
9 3 -0.7683 -46 74 -73 imp:n=1 $ D2, boron cell
c
c ----- Detector at 30 cm ----
c
10 3 -0.7683 -47 71 -72 imp:n=1 $ D1, boron cell
c ----- Detector 2 -----
11 5 -8.69 -48 71 -74 imp:n=1 $ Cd on back, D1
12 3 -0.7683 -48 74 -73 imp:n=1 $ D2, boron cell
c
c ----- Detector at 10cm on x and 0cm on z ----
c
13 3 -0.7683 -51 81 -82 imp:n=1 $ D1, boron cell
c ----- Detector 2 -----
14 5 -8.69 -52 81 -84 imp:n=1 $ Cd on back, D1
15 3 -0.7683 -52 84 -83 imp:n=1 $ D2, boron cell
c
c ----- Detector at 10cm on x and 10cm on z ----
c
16 3 -0.7683 -53 81 -82 imp:n=1 $ D1, boron cell
c ----- Detector 2 -----
17 5 -8.69 -54 81 -84 imp:n=1 $ Cd on back, D1
18 3 -0.7683 -54 84 -83 imp:n=1 $ D2, boron cell
c
c ----- Detector at 10cm on x and 20cm on z ----
c
19 3 -0.7683 -55 81 -82 imp:n=1 $ D1, boron cell
c ----- Detector 2 -----
20 5 -8.69 -56 81 -84 imp:n=1 $ Cd on back, D1
```

```

21 3 -0.7683 -56 84 -83 imp:n=1 $ D2, boron cell
c
c ----- Detector at 10cm on x and 30cm on z ----
c
22 3 -0.7683 -57 81 -82 imp:n=1 $ D1, boron cell
c ----- Detector 2 -----
23 5 -8.69 -58 81 -84 imp:n=1 $ Cd on back, D1
24 3 -0.7683 -58 84 -83 imp:n=1 $ D2, boron cell
c
c ----- Water phantom -----
41 2 -1 -10 -11 12 imp:n=1 $ water phantom
42 4 -0.0012 -99 (10:11:-12) #1 #2 #3 #4 #5 #6 #7 #8 #9 &
#10 #11 #12 #13 #14 #15 #16 #17 #18 &
#19 #20 #21 #22 #23 #24 imp:n=1 $ air inside the boundary
99 0 99 imp:n=0 $ graveyard

c ***** Surface Cards *****
c ----- Cylindrical water phantom -----
c
10 sq 1 4.0 0 0 0 0 -400.0 0 0 0
11 pz 35
12 pz -35
c ----- End of water phantom -----
c
c ----- Detectors -----
c
c ----- Positions of detectors along the z-axis -----
41 c/y 0 1 0.5
42 c/y 0 -1 0.5
43 c/y 0 11 0.5
44 c/y 0 9 0.5
45 c/y 0 21 0.5
46 c/y 0 19 0.5
47 c/y 0 31 0.5
48 c/y 0 29 0.5
c
c ----- Positions of the detector at -10 cm on x axis -----
51 1 c/y 0 1 0.5
52 1 c/y 0 -1 0.5
53 1 c/y 0 11 0.5
54 1 c/y 0 9 0.5
55 1 c/y 0 21 0.5
56 1 c/y 0 19 0.5
57 1 c/y 0 31 0.5
58 1 c/y 0 29 0.5
c
71 py 10.001 $ B, for D1
72 py 10.006 $ B, for D1
73 py 10.009 $ B, for D2
c ----- Detector no. 2 -----
c
74 py 10.004 $ Cd on back 2nd surface
c
81 1 py 0.001 $ B, for D1
82 1 py 0.006 $ B, for D1
83 1 py 0.009 $ B, for D2
c ----- Detector no. 2 -----
c
84 1 py 0.004 $ Cd on back.2nd surface
99 so 2000 $ Radius of the graveyard

c

```

```

c ***** Data Cards *****
c
c ----- Parallel beam of Watt energy spectrum -----
SDEF pos = 0 150 0 par=1 erg = d1 x= d2 y=150.0 z= d3 vec= 0 -1 0 dir=1
SP1 -3 0.988 2.249
SI2 -20 20
SP2 0 1
SI3 -35 35
SP3 0 1
c
c ----- End of parallel beam -----
c
MODE N
NPS 20000000
c
*tr1 10 8.66025 0 16.10 106.10 90 73.9 16.10 90 90 90 0          $ 16.10 degree rotation
c
fc14 reaction/mSv in the detector cells
fl4:n 1 3 4 6 7 9 10 12 13 15 16 18 19 21 22 24
fm14 1.319E06 3 107
c
c -----
c Composition of water (nominal density 1 g/cm^3)
c -----
m2 1001.50c -0.11190
8016.50c -0.88810
c -----
c Composition of B (nominal density 0.7683 g/cm^3)
c -----
m3 5010.60c -1.0000
c -----
c Composition of the air (nominal density 0.0012 g/cm^3)
c -----
m4 7014.50c -0.7558
8016.50c -0.2314
18000.35c -0.0128
c -----
c Composition of the cadmium (nominal density 8.69 g/cm^3)
c -----
m5 48000.51d -1.0000
c
c -----
mt2 lwtr.01
c --- Print Card
PRINT 110

```

A.2. Anthropomorphic Phantom

MCNP4C example code used to observe the detector responses for a parallel beam of Maxwellian spectrum on the surface of the torso of the anthropomorphic phantom.

```

c Calculation of dose using the semiconductor neutron detector for male anthropomorphic phantom
c -----
c Cell Card
c -----
1  1 -0.001293  -1 (7:-37:6) (-6:33:35) 34 (-45:37:-43:44:4:-46)
    (37:-38:39) (37:-38:40) 107 108 #62 #63 #64 #65 #66
    #67 #68 #69 #70 #71 #72 #73 #74 #75 #76 #77 #78 #79
    #80 #81 #82 #83 #84 #85
2  2 -0.2958  ((-2 -4 3):(-2 4)) 5                                $ left lung
3  3 -0.9869  -7 51 -6 (-8:32) 84 101 #2 #24 #28 #58 #59
    (113:115) (114:115)                                           $ torso
4  3 -0.9869  -7 8 -32 117 113 114 #15 #16 #17 #18 #19 #20
    (-4:-9:116:118:-119) (-4:-9:116:120:-121)                   $ torso
5  3 -0.9869  -7 8 -117 51 113 114 #9 #13 #14
6  3 -0.9869  -7 50 -51 56 84 96 105 106 113 114 #10 #11 #12
    #27 #43 #44 #47                                               $ torso
7  3 -0.9869  -7 97 -50 113 114 #30 #32 #33 #38 #39 #40
8  3 -0.9869  -7 37 -97 95 113 114 #31 #33 #38
9  4 -1.4862  8 -9 5 -10                                           $ rib
10 4 -1.4862  8 -9 11 -12                                          $ rib
11 4 -1.4862  8 -9 13 -14                                          $ rib
12 4 -1.4862  8 -9 15 -16                                          $ rib
13 4 -1.4862  8 -9 17 -18                                          $ rib
14 4 -1.4862  8 -9 19 -20                                          $ rib
15 4 -1.4862  8 -9 21 -22                                          $ rib
16 4 -1.4862  8 -9 23 -24                                          $ rib
17 4 -1.4862  8 -9 25 -26                                          $ rib
18 4 -1.4862  8 -9 27 -28                                          $ rib
19 4 -1.4862  8 -9 29 -30                                          $ rib
20 4 -1.4862  8 -9 31 -32                                          $ rib
21 3 -0.9869  ((35 -34):(-33 6 -35)) 102 (84:85)
    #37 #60 #61                                                    $ head
22 3 -0.9869  -37 38 -39 103                                         $ left leg
23 3 -0.9869  -37 38 -40 104                                         $ right leg
24 2 -0.2958  ((-41 -4 42):(-41 4)) 5                                $ right lung
25 3 -0.9869  45 -37 43 -44 -4 46 39 40 72 73                       $ genitalia
26 3 -0.9869  -47                                                    $ brain
27 3 -0.9869  50 -51 -48 -49                                         $ liver
28 3 -0.9869  (-52 54):(-53 -54 55)                                 $ heart
29 3 -0.9869  -56                                                    $ stomach
30 3 -0.9869  -57 58 -59                                             $ ascending
31 3 -0.9869  (-63 65 -61):(-64 37 -65)                             $ sigmoid
32 3 -0.9869  -62 66 -67                                             $ transverse
33 3 -0.9869  -60 61 -59 -83                                          $ descending
35 3 -0.9869  -72                                                    $ testicle
36 3 -0.9869  -73                                                    $ testicle
37 3 -0.9869  -74 75 -76 6 -77                                        $ thyroid
38 4 -1.4862  -82 83 37 -78 80 (79:-81)                              $ pelvis
39 4 -1.4862  -84 78 -85 102                                          $ spine
40 3 -0.9869  -83 86 -50 88 -87 #30 #32 #33                          $ small int.
41 1 -0.001293 -107 7 -4 #77 #81 #82
42 1 -0.001293 -108 7 -4 #77 #81 #82

```

43	3	-0.9869	-92 65	\$ kidney
44	3	-0.9869	-93 -94	\$ kidney
45	3	-0.9869	-95	\$ bladder
46	3	-0.9869	-96	\$ spleen
47	3	-0.9869	-98 99 (-65:100)	\$ pancreas
48	3	-0.9869	-101	\$ thymus
49	4	-1.4862	47 -102 #60 #61	\$ skull
50	4	-1.4862	-103 38 -37	\$ leg bone
51	4	-1.4862	-104 38 -37	\$ leg bone
52	3	-0.9869	-105 92	\$ adrenal
53	3	-0.9869	-106 93	\$ adrenal
54	4	-1.4862	37 -115 -113	\$ arm bone
55	4	-1.4862	37 -115 -114	\$ arm bone
56	4	-1.4862	4 9 -32 -116 117 -118 119	\$ scapulae
57	4	-1.4862	4 9 -32 -116 117 -120 121	\$ scapulae
58	4	-1.4862	-4 -122 -123 124	\$ clavicle
59	4	-1.4862	-4 -122 -125 126	\$ clavicle
60	3	-0.9869	-33 128 129 -130 133 -134 -4	\$ eye lens
61	3	-0.9869	-33 128 -131 132 133 -134 -4	\$ eye lens
c -----				
c inserting the detector cell				
c -----				
c ----- pair 1 -----				
c				
c ----- Bare detector, D1 -----				
62	6	-0.7683	-141 -151 152	\$ D1, boron cell
c				
c ----- Cd on the back detector, D2 -----				
c				
63	7	-8.69	-142 -151 153	\$ D2, Cd cell
64	6	-0.7683	-142 -153 154	\$ D2, boron cell
c				
c ----- pair 2 -----				
c				
c ----- Bare detector, D1 -----				
65	6	-0.7683	-143 -151 152	\$ D1, boron cell
c				
c ----- Cd on the back detector, D2 -----				
c				
66	7	-8.69	-144 -151 153	\$ D2, Cd cell
67	6	-0.7683	-144 -153 154	\$ D2, boron cell
c				
c ----- pair 3 -----				
c				
c ----- Bare detector, D1 -----				
68	6	-0.7683	-145 -151 152	\$ D1, boron cell
c				
c ----- Cd on the back detector, D2 -----				
c				
69	7	-8.69	-146 -151 153	\$ D2, Cd cell
70	6	-0.7683	-146 -153 154	\$ D2, boron cell
c				
c ----- pair 4 -----				
c				
c ----- Bare detector, D1 -----				
71	6	-0.7683	-147 -151 152	\$ D1, boron cell
c				
c ----- Cd on the back detector, D2 -----				
c				
72	7	-8.69	-148 -151 153	\$ D2, Cd cell
73	6	-0.7683	-148 -153 154	\$ D2, boron cell
c				

```

c
c ----- Rotated pair detectors are starting from here -----
c ----- Pair 1 -----
c
c ----- Bare detector, D1 -----
74 6 -0.7683      -161 -171 172          $ D1, boron cell
c
c ----- Cd on the back detector, D2 -----
c
75 7 -8.69       -162 -171 173          $ D2, Cd cell
76 6 -0.7683     -162 -173 174          $ D2, boron cell
c
c ----- Pair 2 -----
c
c ----- Bare detector, D1 -----
77 6 -0.7683     -163 -171 172          $ D1, boron cell
c
c ----- Cd on the back detector, D2 -----
c
78 7 -8.69       -164 -171 173          $ D2, Cd cell
79 6 -0.7683     -164 -173 174          $ D2, boron cell
c
c ----- Pair 3 -----
c
c ----- Bare detector, D1 -----
80 6 -0.7683     -165 -171 172          $ D1, boron cell
c
c ----- Cd on the back detector, D2 -----
c
81 7 -8.69       -166 -171 173          $ D2, Cd cell
82 6 -0.7683     -166 -173 174          $ D2, boron cell
c
c ----- Pair 4 -----
c
c ----- Bare detector, D1 -----
83 6 -0.7683     -167 -171 172          $ D1, boron cell
c
c ----- Cd on the back detector, D2 -----
c
84 7 -8.69       -168 -171 173          $ D2, Cd cell
85 6 -0.7683     -168 -173 174          $ D2, boron cell
c
86 0              1

```

```

c -----
c Surface Cards
c -----
c
1  so 200
2  sq 23.04 10.24 1 0 0 0 -576 8.5 0 43.5
3  sq 23.04 10.24 1 0 0 0 -576 2.5 0 43.5
4  py 0.0
5  pz 43.5
6  pz 70
7  sq 1 4.0 0 0 0 0 -400.0 0 0 0
8  sq 1 3.15 0 0 0 0 -272.25 0 0 0
9  sq 1 3.01 0 0 0 0 -289.0 0 0 0
10 pz 44.9
11 pz 35.1
12 pz 36.5
13 pz 37.9
14 pz 39.3

```

15 pz 40.7
16 pz 42.1
17 pz 46.3
18 pz 47.7
19 pz 49.1
20 pz 50.5
21 pz 51.9
22 pz 53.3
23 pz 54.7
24 pz 56.1
25 pz 57.5
26 pz 58.9
27 pz 60.3
28 pz 61.7
29 pz 63.1
30 pz 64.5
31 pz 65.9
32 pz 67.3
33 sq 100 49 0 0 0 0 -4900 0 0 0
34 sq 7225 3540.25 4900 0 0 0 -354025 0 0 85.5
35 pz 85.5
37 pz 0
38 pz -80
39 gq 5 5 0 0 0 -1 -100 0 0 0
40 gq 5 5 0 0 0 1 100 0 0 0
41 sq 23.04 10.24 1 0 0 0 -576 -8.5 0 43.5
42 sq 23.04 10.24 1 0 0 0 -576 -2.5 0 43.5
43 p 10 0 1 -100
44 p 10 0 -1 100
45 pz -4.8
46 p 0 10 1 -100
47 sq 2.25 1 1.91716 0 0 0 -81 0 0 86.5
48 sq 64 272.25 0 0 0 0 -17424 0 0 0
49 p 9 7 -7.3256 -315
50 pz 27
51 pz 43
52 gq 45.2 59.9 47.9 17.5 -16.2 34.8 -1632.1 1204.8 -4898.2 124295.2
53 sq 1 1 1 0 0 0 -25 -1 -3 51
54 p .6943 -.3237 -.6428 -32.506
55 p 5.2193 -2.4336 -0.916 -59.6345
56 sq 4 7.11 1 0 0 0 -64 8 -4 35
57 sq 1 1 0 0 0 0 -6.25 -8.5 -2.36 0
58 pz 14.45
59 pz 24
60 gq 4.54 3.53 .096 0 1.16 -0.166 -77.68 -10.08 -.223 323.52
61 pz 8.72
62 sq 0 2.25 6.25 0 0 0 -14.0625 0 -2.36 25.5
63 ty 3 0 8.72 5.72 1.57 1.57
64 ty 3 0 0 3 1.57 1.57
65 px 3
66 px -10.5
67 px 10.5
72 sq 11.9025 8.9401 3.8025 0 0 0 -20.115225 1.3 -8 -2.3
73 sq 11.9025 8.9401 3.8025 0 0 0 -20.115225 -1.3 -8 -2.3
74 c/z 0 -6 2.2
75 c/z 0 -6 1
76 py -6
77 pz 75
78 pz 22
79 pz 14
80 py -3
81 py 5

82 c/z 0 -3 12
83 c/z 0 -3.8 11.3
84 sq 6.25 4 0 0 0 0 -25 0 5.5 0
85 pz 78.5
86 pz 17
87 py 2.2
88 py -4.86
92 sq 1.49 13.44 1 0 0 0 -30.25 6 6 32.5
93 sq 1.49 13.44 1 0 0 0 -30.25 -6 6 32.5
94 px -3
95 sq 1 2.0557 2.0557 0 0 0 -24.5818 0 -4.5 8
96 sq 2.94 9 1 0 0 0 -36 11 3 37
97 pz 12
98 sq 1 225 25 0 0 0 -225 0 0 37
99 px 0
100 pz 37
101 sq 1.78 64 1 0 0 0 -16 -2 -6 60.5
102 sq 2.08 1 1.39 0 0 0 -96.04 0 0 85.5
103 gq 1 1 .0091 0 0 -.2005 -20 0 1.7857 87.75
104 gq 1 1 .0091 0 0 .2005 20 0 1.7857 87.75
105 sq 100 900 9 0 0 0 -225 4.5 6.5 38
106 sq 100 900 9 0 0 0 -225 -4.5 6.5 38
107 sq 1.39 .5 2 0 0 0 -70 -6.5 -3 50
108 sq 1.39 .5 2 0 0 0 -70 6.5 -3 50
113 gq 503.01 135.24 0 0 0 10.206 -19215 0 -202.0788 183257
114 gq 503.01 135.24 0 0 0 -10.206 19215 0 -202.0788 183257
115 pz 69
116 sq 1 3.7589 0 0 0 0 -361 0 0 0
117 pz 50.9
118 p 0.25 -1 0 0
119 p 0.8 -1 0 0
120 p -0.25 -1 0 0
121 p -0.8 -1 0 0
122 tz 0 11.1 68.25 20 0.7883 0.7883
123 p 0.89415 1 0 11.1
124 p 7.0342 1 0 11.1
125 p -0.89415 1 0 11.1
126 p -7.0342 1 0 11.1
128 sq 88.36 40.96 0 0 0 0 -3619.2256 0 0 0
129 px 2
130 px 4
131 px -2
132 px -4
133 pz 82.5
134 pz 84.5
c
c -----
c Inserting the detector surface cards
c -----
141 c/y 0 36 0.5 \$ 1st pair of bare detector
142 c/y 0 34 0.5 \$ Cd-filtered detector
143 c/y 0 46 0.5 \$ 2nd pair of bare detector
144 c/y 0 44 0.5 \$ Cd-filtered detector
145 c/y 0 56 0.5 \$ 3rd pair of bare detector
146 c/y 0 54 0.5 \$ Cd-filtered detector
147 c/y 0 66 0.5 \$ 4th pair of bare detector
148 c/y 0 64 0.5 \$ Cd-filtered detector
c ----- Detector 1, bare -----
151 py -10.001 \$ B, for D1
152 py -10.006 \$ B for D1
c
c ----- Detector 2, Cd on back -----

```

c
153 py -10.004          $ B, for D1
154 py -10.009          $ B for D1
c
c ----- surfaces for the rotated detectors at x=10cm -----
c
161 1 c/y 0 36 0.5      $ 1st pair of bare detector
162 1 c/y 0 34 0.5      $ Cd-filtered detector
163 1 c/y 0 46 0.5      $ 2nd pair of bare detector
164 1 c/y 0 44 0.5      $ Cd -filtered detector
165 1 c/y 0 56 0.5      $ 3rd pair of bare detector
166 1 c/y 0 54 0.5      $ Cd -filtered detector
167 1 c/y 0 66 0.5      $ 4th pair of bare detector
168 1 c/y 0 64 0.5      $ Cd -filtered detector
c ----- Detector 1, bare -----
171 1 py -0.001         $ B, for D1
172 1 py -0.006         $ B for D1
c
c ----- Detector 2, Cd on back -----
c
173 1 py -0.004         $ B, for D1
174 1 py -0.009         $ B for D1
c
c -----
c Data Cards
c -----
vol  0 1689 8882.47 1520.8 855.6 6616.5 7150.5 6830.4 57.83 11r
    2174.72 8988.5 8988.5 1689 158.73 1470 1833 603.1 402.1 187.51
    106.05 247.4 192.22 18.785 18.785 30.16 606.1 887.5 1054
    172.2 172.2 144. 144. 248.33 175.9 61.07 25.13 846.6 1399.5
    1399.5 7.855 7.855 478 478 100.7 100.7 27.35 27.35 2.749 2.749
    0.00392699 0.00235619 0.00392699 0.00392699 0.00235619 0.00392699
    0.00392699 0.00235619 0.00392699 0.00392699 0.00235619 0.00392699
    0.00392699 0.00235619 0.00392699 0.00392699 0.00235619 0.00392699
    0.00392699 0.00235619 0.00392699 0.00392699 0.00235619 0.00392699 0
area  0 5r 6954.21 0 24r 840.6 0 87r 0 23r
imp:n 1 83r 0
c
c ----- Parallel beam of Maxwellian spectrum -----
c
SDEF pos = 0 150 0 par=1 erg=d1 x=d2 y=150.0 z=d3 vec=0.0 -1.0 0.0 dir=1
SP1  -2  2.53E-08
SI2  -20  20
SP2   0  1
SI3   0  70
SP3   0  1
c ----- end of parallel beam -----
c -----
c Material Card
c -----
c  Composition for air
m1  7014 -.7558 8016 -.2314 18000 -.0128
c  Composition for lung tissue
m2  1001 -.1021
    6012 -.1001
    7014 -.0280
    8016 -.7596
    11023 -.0019
    15031 -.0008
    16032 -.0023
    17000 -.0027

```

```

19000 -.0020
20000 -.0001
26000 -.0004
c   Composition for total body minus skeleton and lungs
m3  1001 -.1047
    6012 -.2302
    7014 -.0234
    8016 -.6321
    11023 -.0013
    12000 -.0002
    15031 -.0024
    16032 -.0022
    17000 -.0014
    19000 -.0021
c   Composition for skeletal tissue
m4  1001 -.0704
    6012 -.2279
    8016 -.4856
    7014 -.0387
    11023 -.0032
    12000 -.0011
    15031 -.0694
    16032 -.0017
    17000 -.0014
    19000 -.0015
    20000 -.0991
mt2  lwtr.01
mt3  lwtr.01
mt4  lwtr.01
c -----
c material cards for detector
c -----
c composition of B (nominal density 0.7683 g/cm^3)
c -----
m6  5010.60c -1.0000
c -----
c composition of the cadmium (nominal density 8.69 g/cm^3)
c -----
m7  48000.51d -1.0000
c ----- end of detector material card -----
c
fc44      reaction/mSv in the detector cells
f44:n 62 64 65 67 68 70 71 73 74 76 77 79 80 82 83 85
fm44 4.792E07 6 107  $
c
nps 20e+06                                     $ History Cutoff card,
mode n
c ----- The surface rotation code -----
c
*tr1 10 -8.66025 0 16.10 73.9 90 106.1 16.10 90 90 90 0  $ 16.10 degree rotation
c
c ----- print card -----
print 110

```

Appendix B - Detailed Calculations for Neutron Dosimeter Modeling

This appendix discusses detailed descriptions of the various calculations related to the neutron dosimeter.

B.1. Calculation of Atom Density for ^{10}B Material

The density of natural boron is, $\rho_{nat} = 2.37 \text{ gm cm}^{-3}$ and the mass number is $A_{nat} = 10.811$. The isotopic abundance of natural boron is 19.9% ^{10}B is and 80.1% ^{11}B and the mass number for ^{10}B is $A_{10} = 10.0129$ and for ^{11}B is $A_{11} = 11.0093$.

Therefore the density of pure ^{10}B , ρ_{10} , can be calculated using the equation

$$\frac{\rho_{nat} \times N_a}{A_{nat}} = \frac{\rho_{10} \times N_a}{A_{10}}, \quad (\text{B.1})$$

where N_a is Avogadro's constant, $N_a = 6.022 \times 10^{23} \text{ atoms mol}^{-1}$.

Rearranging Eq. (B.1)

$$\begin{aligned} \rho_{10} &= \frac{A_{10} \times \rho_{nat}}{A_{nat}} \\ &= \frac{10.0129 \times 2.37}{10.811}, \\ &= 2.195 \end{aligned} \quad (\text{B.2})$$

in units of gm cm^{-3} . The detector is assumed to contain boron enriched to 50% in ^{10}B . The coverage of boron in the detector is assumed to be 70%.

Therefore the modified density of ^{10}B material is,

$$\rho_{10} = 2.195 \times 0.5 \times 0.7 = 0.76825, \quad (\text{B.3})$$

and the modified atom density, N_{10} for ^{10}B is,

$$\begin{aligned}
N_{10} &= \frac{\rho_{10} \times N_a}{A_{10}} \\
&= \frac{0.76825 \times 6.022 \times 10^{23}}{10.0129} \times 10^{-24} \\
&= 0.04620
\end{aligned} \tag{B.4}$$

in units of atoms $\text{b}^{-1} \text{cm}^{-1}$.

B.2. Description to Calculate Detector Offset Position at $x = 10$ cm

The detectors at $x = 10$ cm positions are not quite on the surface of the torso because of the curve of the ellipse. The model was corrected at this position in two ways at first the position of the detector along the y -axis was calculated using the equation of the ellipse

$$\frac{x^2}{20^2} + \frac{y^2}{10^2} = 1. \tag{B.5}$$

At $x = 10$ cm and the position of y is 8.66025 cm. The angle of rotation was calculated using the equation of the tangent line of an ellipse is

$$\frac{xx_1}{20^2} + \frac{yy_1}{10^2} = 1 \tag{B.6}$$

The Eq. (B.6) was solved for $x=10$ cm and $y = 8.66025$ cm and rearranging the equation of the tangent line is

$$y = -0.288675x + 11.547, \tag{B.7}$$

which is the equation of a straight line. The slope of the straight line is

$$\tan \theta = 0.288675, \tag{B.8}$$

therefore the angle of rotation of the detector at $x = 10$ cm and $y = 8.66025$ is

$$\theta = 16.10^\circ. \tag{B.9}$$

B.3. MCNP Neutron Dosimeter Normalization Constant

B.3.1 Watt Spectrum

The eight pairs of detectors were analyzed with Watt fission spectrum. The Watt fission spectrum can be written in the form

$$\chi(E) = Ce^{-E/a} \sinh \sqrt{bE}, \quad (\text{B.10})$$

where C , a , and b are parameters that depend on the fissioning isotope and to some extent on the energy of the neutrons causing the fission. For thermal neutron fission of ^{235}U , MCNP uses the values $a = 0.988$ and $b = 2.249$. In order to normalize the Probability Density Function (PDF), the value of C should be approximately 0.438.

The Watt distribution is evaluated at the 47 energies for which the response function is tabulated; these range from 10^{-9} MeV to 20 MeV. Therefore the estimated integral is

$$I = \int_0^{\infty} \chi(E) \mathfrak{R}(E) dE, \quad (\text{B.11})$$

which can be expressed by quadrature, as

$$I_W = \sum_{i=1}^{47} \chi(E_i) \mathfrak{R}(E_i) \Delta E_i, \quad (\text{B.12})$$

where E_i are the energies at which the response function is tabulated and ΔE_i are contiguous energy interval widths centered on the E_i is

$$\Delta E_i = \left[E_i + \frac{E_{i+1} - E_i}{2} \right] - \left[E_{i-1} + \frac{E_i - E_{i-1}}{2} \right], i = 2, 3, \dots, 46, \quad (\text{B.13})$$

with

$$\Delta E_1 = 5.5 \times 10^{-9}, \quad (\text{B.14})$$

and

$$\Delta E_{47} = 1, \quad (\text{B.15})$$

Therefore the value of the Watt integral is

$$I_W = 3.85 \times 10^{-10}, \text{ Sv cm}^2 \text{ per neutron.} \quad (\text{B.16})$$

Thus, the multiplicative constant to multiply the MCNP results, which will give detector response per source neutron, is

$$\frac{1}{S_a I_W} = \frac{2,800}{3.85 \times 10^{-7}} \quad (\text{B.17})$$

B.3.2 Maxwellian Spectrum

For a Maxwellian spectrum of thermal neutrons, the response function is used at the most probable energy, i.e.

$$\mathfrak{R}(E = 0.0253 \text{ eV}) = \mathfrak{R}_0 = 10.6 \times 10^{-12} \text{ Sv cm}^2 \text{ per source neutron} \quad (\text{B.18})$$

and obtain

$$I_M = \mathfrak{R}_0 \int_0^{E_{Tc}} \phi_M(E) dE \cong \mathfrak{R}_0. \quad (\text{B.19})$$

Since

$$\int_0^{E_{Tc}} \phi_M(E) dE \cong \int_0^{\infty} \frac{E}{E_T^2} e^{-E/E_T} dE = 1 \quad (\text{B.20})$$

where

$$E_{Tc} = 2 \times 10^{-7} \text{ MeV}, \quad (\text{B.21})$$

and

$$E_T = kT = 2.53 \times 10^{-8} \text{ MeV}, \quad (\text{B.22})$$

for a “temperature” of $T = 293.41 \text{ K}$, and $k = 8.617342 \times 10^{-11} \text{ MeV/K}$ is Boltzmann’s constant.

Thus, for a Maxwellian spectrum

$$I_M = 1.06 \times 10^{-11} \text{ Sv cm}^2 \text{ per source neutron.} \quad (\text{B.23})$$

Thus, the multiplicative constant to multiply the MCNP results, which will give detector response per source neutron, is

$$\frac{1}{S_a I_M} = \frac{2800}{1.06 \times 10^{-8}} \text{ mSv}^{-1}, \quad (\text{B.24})$$

for a Maxwellian incident spectrum.

B.3.3 Mono-Energetic Neutron Beam

For a mono-energetic beam, the response function per unit fluence for the specific energy is collected from ICRU (2001). The following are the response functions for energies 1 MeV to 5 MeV:

$$E_0 = 1 \text{ MeV} \Rightarrow \mathfrak{R}_H(E_0) = 4.16 \times 10^{-10} \text{ pSv cm}^2 \text{ per source neutron,}$$

$$E_0 = 2 \text{ MeV} \Rightarrow \mathfrak{R}_H(E_0) = 4.20 \times 10^{-10} \text{ pSv cm}^2 \text{ per source neutron,}$$

$$E_0 = 3 \text{ MeV} \Rightarrow \mathfrak{R}_H(E_0) = 4.12 \times 10^{-10} \text{ pSv cm}^2 \text{ per source neutron,}$$

$$E_0 = 4 \text{ MeV} \Rightarrow \mathfrak{R}_H(E_0) = 4.08 \times 10^{-10} \text{ pSv cm}^2 \text{ per source neutron,}$$

and

$$E_0 = 5 \text{ MeV} \Rightarrow \mathfrak{R}_H(E_0) = 4.05 \times 10^{-10} \text{ pSv cm}^2 \text{ per source neutron.}$$

And the multiplicative factors are thus

$$\frac{1}{S_a \mathfrak{R}_H} = \frac{2,800}{4.16 \times 10^{-7}} \text{ mSv}^{-1}, E_0 = 1 \text{ MeV.} \quad (\text{B.25})$$

$$\frac{1}{S_a \mathfrak{R}_H} = \frac{2,800}{4.20 \times 10^{-7}} \text{ mSv}^{-1}, E_0 = 2 \text{ MeV.} \quad (\text{B.26})$$

$$\frac{1}{S_a \mathfrak{R}_H} = \frac{2,800}{4.12 \times 10^{-7}} \text{ mSv}^{-1}, E_0 = 3 \text{ MeV.} \quad (\text{B.27})$$

$$\frac{1}{S_a \mathfrak{R}_H} = \frac{2,800}{4.08 \times 10^{-7}} \text{ mSv}^{-1}, E_0 = 4 \text{ MeV.} \quad (\text{B.28})$$

$$\frac{1}{S_a \mathfrak{R}_H} = \frac{2,800}{4.05 \times 10^{-7}} \text{ mSv}^{-1}, E_0 = 5 \text{ MeV.} \quad (\text{B.29})$$

Appendix C - Efficiency of HPGe Detector

The mixed source used to determine the efficiency of the HPGe detector contains three different isotopes Eu-152, Eu-154 and Eu-155. The data were collected for 40 min. Therefore the disintegration per second for each isotope was converted to disintegrations for 40 min. The isotopes of the mixed source, the disintegration per second of each isotope and the corresponding disintegration for 40 min of each isotope are presented in Table-C.1.

Table - C.1. Emitting Isotopes of the Mixed Source and the Total Number of Radiation Quanta Emitted from Each Isotope.

Isotope	Disintegration per second (DPS)	Disintegration for 40 min, (D_{40})
Eu-152	7489.59	17975016
Eu-154	8595.08	20628192
Eu-155	11736.40	28167360

The identified energy peaks of the mixed source spectrum, the corresponding emitting isotope, the total counts under each energy peak and the corresponding intensity, the calculated efficiency of each energy peak are presented in Table-C.2.

Table - C.2. Identified Energy from the Mixed Source Spectrum, Corresponding Emitting Isotope, Total Counts under Each Peak, Intensity and Calculated Efficiency.

Energy (keV)	Emitting isotope	Total counts under the peak, C^\dagger	Frequency of the emitting energy, I^*	$\varepsilon = \frac{C}{D_{40} I}$
60.06	Eu-155	1862.78	0.0122	0.005420702
86.64	Eu-155	75977.50	0.3070	0.008786188
105.39	Eu-155	58235.10	0.2110	0.009798424
121.80	Eu-152	47966.20	0.2867	0.009307613
123.13	Eu-154	87240.80	0.4060	0.010416755
244.86	Eu-152	10160.10	0.0761	0.007427524
248.08	Eu-154	10229.40	0.0691	0.007176471
344.50	Eu-152	27053.00	0.2660	0.005658020
411.42	Eu-152	2039.63	0.0224	0.005072431
591.87	Eu-154	3297.03	0.0496	0.003222405
723.40	Eu-154	12487.80	0.2011	0.003010320
778.93	Eu-152	7070.65	0.1296	0.003035184
873.13	Eu-154	6519.36	0.1220	0.002590502
964.06	Eu-152	6722.28	0.1465	0.002552758
996.29	Eu-154	5160.13	0.1053	0.002375588
1004.8	Eu-154	9321.35	0.1791	0.002523028
1085.9	Eu-152	4061.50	0.1024	0.002206567
1112.1	Eu-152	5675.99	0.1369	0.002306582
1274.4	Eu-154	14268.70	0.3500	0.001976311
1408.0	Eu-152	6969.80	0.2107	0.001840291

† Using FORTRAN program

* Data collected from the web site, <http://www.nndc.bnl.gov/nudat2>.

Appendix D - Detail Calculation of Thermal and Epi-thermal Flux

D.1. Flux Calculation

The area under the 411.8 keV peak of the irradiated gold foil were calculated using the built in peak analysis report of the Gamma Acquisition & Analysis software, Genie 2000. The area under the peak both for bare and Cd-covered gold foil and their corresponding uncertainty in the peak area are presented in Table D.1.

Table - D.1. Area Under the 411.8 keV Peak of the Irradiated Gold Foils.

Gold Foil	Area Under Peak (total counts, R_γ)	Uncertainty in the peak area, (σ_{R_γ})
Bare Gold Foil (b)	2.95E+ 004	182.78
Cd-covered foil (Cd)	1.55E+004	158.23

To calculate ϕ_t , take into consideration Eqs. (4.42) and (4.45), namely

$$\hat{M}_b - \hat{M}_c = \frac{N_a \bar{\sigma}_a}{A_d} [\phi_t + 0.256 \phi_0] \quad (D.1)$$

and

$$CR = 1 + \frac{\bar{\sigma}_a}{I_d} \left[\frac{\phi_t}{\phi_0} + 0.256 \right]. \quad (D.2)$$

Applying the cadmium filter correction factor, the specific production rate for epithermal neutrons can be written as

$$\hat{M}_e = F_{cd} \hat{M}_c, \quad (D.3)$$

where

$$F_{cd} = e^{-\Sigma_{cd}(E_\gamma)l_c}, \quad (D.4)$$

and

$$\Sigma_{Cd}(E_r) = \frac{N_a \rho_{Cd}}{A_{Cd}} \sigma_{Cd}(E_r), \quad (D.5)$$

where $\sigma_{Cd}(E_r) = 5.5 \text{ b}$, $A_{Cd} = 112.40$, $\rho_{Cd} = 8.65 \text{ gm cm}^{-3}$, $N_a = 6.022 \times 10^{23} \text{ atoms mol}^{-1}$, and the thickness of the Cd sheet was $t_c = 0.0508 \text{ cm}$. Substituting these values into Eq. (D.5) one obtain

$$\Sigma_{Cd}(E_r) = 0.255 \text{ cm}^{-1}, \quad (D.6)$$

and the cadmium correction factor, Eq. (D.4) becomes

$$F_{Cd} = 1.013. \quad (D.7)$$

Replacing \hat{M}_c by \hat{M}_e , Eq. (D.1) and Eq. (D.2) can be written as

$$\hat{M}_b - \hat{M}_e = \frac{N_a \bar{\sigma}_a}{A_d} [\phi_t + 0.256 \phi_0], \quad (D.8)$$

and

$$\frac{\hat{M}_b}{\hat{M}_e} = 1 + \frac{\bar{\sigma}_{at}}{I_d} \left[\frac{\phi_t}{\phi_0} + 0.256 \right]. \quad (D.9)$$

Let

$$C_1 = \frac{N_a \bar{\sigma}_{at}}{A_d} = \frac{(6.023 \times 10^{23}) \times (87.32 \times 10^{-24})}{196.967} = 0.2670, \quad (D.10)$$

and

$$C_2 = \frac{\bar{\sigma}_{at}}{I_d} = \frac{87.32 \times 10^{-24}}{1558 \times 10^{-24}} = 0.05604621. \quad (D.11)$$

Therefore Eq. (D.8) can be written as

$$\hat{M}_b - \hat{M}_e = C_1 [\phi_t + 0.256 \phi_0]. \quad (D.12)$$

Equation (D.12) can be written as

$$\frac{\hat{M}_b - \hat{M}_e}{C_1} = \phi_t + 0.256 \phi_0. \quad (D.13)$$

Rearranging Eq. (D.13), the thermal flux can be written as

$$\phi_t = \frac{\hat{M}_b - \hat{M}_e}{C_1} - 0.256 \phi_0. \quad (D.14)$$

Equation (D.9) can also be written as

$$\frac{\hat{M}_b}{\hat{M}_e} = 1 + C_2 \left[\frac{\phi_t}{\phi_0} + 0.256 \right]. \quad (\text{D.15})$$

Rearranging, Eq. (D.15), one obtain

$$\frac{\phi_0}{C_2} \left(\frac{\hat{M}_b}{\hat{M}_e} - 1 \right) = \phi_t + 0.256 \phi_0. \quad (\text{D.16})$$

Now substituting the value of ϕ_t from Eq. (D.14) into Eq. (D.16) and rearranging, it is seen that

$$\phi_0 = \frac{C_2}{C_1} \hat{M}_e. \quad (\text{D.17})$$

The rate of production is calculated using Eq. (4.18)

$$M = \frac{\lambda R_\gamma}{\varepsilon f \left[1 - e^{-\lambda t_0} \right] e^{-\lambda t_w} \left[1 - e^{-\lambda t_c} \right]} \quad (\text{D.18})$$

From Table D.1. $R_{\gamma_b} = 2.95E + 004$ and $R_{\gamma_c} = 1.55E + 004$ counts. The value of λ is

$$\lambda = \frac{0.693}{t_{1/2}} = 2.98 \times 10^{-6} \text{ s}^{-1}. \quad (\text{D.19})$$

The efficiency, ε , of the detector at energy 411.8 keV was calculated using the equation (4.9), $\varepsilon_{411.8 \text{ keV}} = 0.004916$, the values of t_0 , t_w and t_c for bare and Cd-covered foils are found in Table 4.2, and the value of $f = 0.995$. Substituting all these values into Eq. (D.18) the rate of production for bare foil is

$$M_b = 57415.07 \text{ atoms s}^{-1}, \quad (\text{D.20})$$

and for the Cd-covered foil is

$$M_c = 10152.79 \text{ atoms s}^{-1}. \quad (\text{D.21})$$

The calculated specific activation rates are

$$\hat{M}_b = 21.00 \times 10^5 \text{ atoms gm}^{-1} \text{ s}^{-1}, \quad (\text{D.22})$$

and

$$\hat{M}_c = 24.29 \times 10^4 \text{ atoms gm}^{-1} \text{ s}^{-1}, \quad (\text{D.23})$$

and

$$\hat{M}_e = \hat{M}_c \times F_{Cd} = 24.61 \times 10^4 \text{ atoms gm}^{-1} \text{ s}^{-1}. \quad (\text{D.24})$$

Therefore using Eq. (D.17), the value of ϕ_0 is

$$\phi_0 = 5.17 \times 10^4 \text{ cm}^{-2} \text{ s}^{-1}. \quad (\text{D.25})$$

and using Eq. (D.14) the value of ϕ_t is

$$\phi_t = 6.93 \times 10^6 \text{ cm}^{-2} \text{ s}^{-1}. \quad (\text{D.26})$$

Calculation of Free-Field Thermal Flux

The free-field thermal flux was calculated using Eq. (4.51)

$$\phi_\infty = \frac{1}{F_1 F_2} \bar{\phi}, \quad (\text{D.27})$$

where

$$\bar{\phi} = \phi_t. \quad (\text{D.28})$$

and considering that the beam is parallel at the tangential beam port.

$$F_2 = 1 \quad (\text{D.29})$$

The value of F_1 from Eq. (4.59) is

$$F_1 = \frac{1 - e^{-\bar{\Sigma}_a t}}{\bar{\Sigma}_a t}, \quad (\text{D.30})$$

where

$$\bar{\Sigma}_a t = N \bar{\sigma}_a t. \quad (\text{D.31})$$

Substituting the values of, $N = \frac{\rho N_a}{A} = \frac{19.32 \times 6.022 \times 10^{23}}{196.967} = 5.91 \times 10^{22} \text{ atoms cm}^{-3}$,

$\bar{\sigma}_a = \frac{\sigma_{a0}}{1.128} \cong \frac{98.5 \times 10^{-24}}{1.128} = 87.3227 \times 10^{-24} \text{ cm}^2$, and $t = 0.00153 \text{ cm}$, thickness of the foil

in Eq. (D.31)

$$\bar{\Sigma}_a t = 7.90 \times 10^{-3}. \quad (\text{D.32})$$

and substituting the value of Eq. (D.32) into Eq. (D.30), the value of F_1 is

$$F_1 = 0.9961. \quad (\text{D.33})$$

Therefore free field thermal flux from Eq. (D.27) is

$$(\phi_\infty)_t = 6.96 \times 10^6 \text{ cm}^{-2} \text{ s}^{-1}. \quad (\text{D.34})$$

Calculation of Fast Flux

From Eq. (4.23)

$$\phi_F \cong 18\phi_0. \quad (\text{D.35})$$

Substituting the value of ϕ_0 from Eq. (D.25)

$$\phi_F = 9.31 \times 10^5 \text{ cm}^{-2} \text{ s}^{-1}. \quad (\text{D.36})$$

Calculation of Free-Field Epi-Thermal Flux

From Eq. (4.60)

$$F_1 = e^{-\frac{\sum_{ar}^{\max} t}{2}} \left[I_0 \left(\frac{\sum_{ar}^{\max} t}{2} \right) + I_1 \left(\frac{\sum_{ar}^{\max} t}{2} \right) \right] \quad (\text{D.37})$$

where,

$$\begin{aligned} \sum_{ar}^{\max} &= N_t \sigma_{ar}^{\max} \\ &= \frac{\rho N_a}{N} \sigma_{ar}^{\max} \\ &= 5.91 \times 10^{22} \times 30600 \times 10^{-24} \\ &= 1808.46 \end{aligned} \quad (\text{D.38})$$

and

$$\frac{\sum_{ar}^{\max} t}{2} = \frac{1808.46 \times 0.00153}{2} = 1.3835. \quad (\text{D.39})$$

From the CRC tables [Zwillinger, 2003],

$$e^{-\frac{\sum_{ar}^{\max} t}{2}} I_0 \left(\frac{\sum_{ar}^{\max} t}{2} \right) = 0.3865 \quad (\text{D.40})$$

and

$$e^{-\frac{\sum_{ar}^{\max} t}{2}} I_1 \left(\frac{\sum_{ar}^{\max} t}{2} \right) = 0.2183. \quad (\text{D.41})$$

Therefore

$$F_1 = 0.3865 + 0.2183 = 0.6048, \quad (\text{D.42})$$

and the free field epithermal flux, from Eq. (D.27), is

$$(\phi_{\infty})_{epi} = \frac{1}{F_1 F_2} \phi_F . \quad (D.43)$$

$$(\phi_{\infty})_{epi} = \frac{9.31 \times 10^5}{0.6048} = 1.85 \times 10^6 \text{ cm}^{-2} \text{ s}^{-1} . \quad (D.44)$$

D.2. Calculation of Propagation of Error

From Eq. (4.54) the free field thermal flux is

$$\phi_{\infty} = \frac{1}{F_1 F_2} \bar{\phi} , \quad (D.45)$$

where

$$\bar{\phi} = \phi_t = \frac{\hat{M}_b}{C_1} - \frac{\hat{M}_e}{C_1} - 0.256 \phi_0 , \quad (D.46)$$

and

$$\frac{\hat{M}_b}{C_1} = \frac{1}{C_1} \times \frac{1}{m_b} \times \frac{\lambda R_{\gamma_b}}{\varepsilon_j f_j [1 - e^{-\lambda t_0}] e^{-\lambda t_w} [1 - e^{-\lambda t_c}]} . \quad (D.47)$$

Substituting the values of C_1 , m_b , ε_j , f_j , λ , t_0 , t_w and t_c from above

$$\frac{\hat{M}_b}{C_1} = 280 R_{\gamma_b} . \quad (D.48)$$

From Eq. (D.3) it follows that

$$\frac{\hat{M}_e}{C_1} = \frac{1}{C_1} \times F_{cd} \times M_c . \quad (D.49)$$

Eq. (D.48) can also be written as

$$\frac{\hat{M}_e}{C_1} = \frac{1}{C_1} \times F_{cd} \times \frac{1}{m_c} \times \frac{\lambda R_{\gamma_c}}{\varepsilon_j f_j [1 - e^{-\lambda t_0}] e^{-\lambda t_w} [1 - e^{-\lambda t_c}]} . \quad (D.50)$$

Substituting all the values from above

$$\frac{\hat{M}_e}{C_1} = 175.7497 R_{\gamma_c} . \quad (D.51)$$

Therefore the Eq. (D.45) can be written as

$$\phi_{\infty} = \frac{1}{F_1 F_2} [280 R_{\gamma_b} - 175.7497 R_{\gamma_c} - 0.256 \phi_0]. \quad (\text{D.52})$$

The associated propagation of error is

$$\sigma_{\phi_{\infty}} = \left[\left(\frac{\partial \phi_{\infty}}{\partial R_{\gamma_b}} \right)^2 \sigma_{R_{\gamma_b}}^2 + \left(\frac{\partial \phi_{\infty}}{\partial R_{\gamma_c}} \right)^2 \sigma_{R_{\gamma_c}}^2 + \left(\frac{\partial \phi_{\infty}}{\partial \phi_0} \right)^2 \sigma_{\phi_0}^2 \right]^{1/2}. \quad (\text{D.53})$$

The value of each term in Eq. (D.53) is following

$$\frac{\partial \phi_{\infty}}{\partial R_{\gamma_b}} = \frac{280}{F_1 F_2} = 281.1. \quad (\text{D.54})$$

$$\frac{\partial \phi_{\infty}}{\partial R_{\gamma_c}} = \frac{175.75}{F_1 F_2} = 176.44. \quad (\text{D.55})$$

$$\frac{\partial \phi_{\infty}}{\partial \phi_0} = \frac{0.256}{F_1 F_2} = 0.257. \quad (\text{D.56})$$

From Table-D.1.

$$\sigma_{R_{\gamma_b}} = 182.78. \quad (\text{D.57})$$

$$\sigma_{R_{\gamma_c}} = 158.23. \quad (\text{D.58})$$

Calculation of σ_{ϕ_0}

From Eq. (D.17)

$$\phi_0 = \frac{C_2}{C_1} \hat{M}_e = \frac{C_2}{C_1} F_{cd} \hat{M}_c. \quad (\text{D.59})$$

Substituting the value of \hat{M}_c , Eq. (D.59) can be written as

$$\phi_0 = \frac{C_2}{C_1} \hat{M}_e = \frac{C_2}{C_1} \times F_{cd} \times \frac{1}{m_c} \times \frac{\lambda R_{\gamma_c}}{\varepsilon_j f_j [1 - e^{-\lambda t_0}] e^{-\lambda t_w} [1 - e^{-\lambda t_c}]}. \quad (\text{D.60})$$

Substituting all the values from above in Eq. (D.60), ϕ_0 can be written as

$$\phi_0 = 3.3780 R_{\gamma_c}. \quad (\text{D.61})$$

Therefore

$$\sigma(\phi_0) = \left[\left(\frac{\partial \phi_0}{\partial R_{\gamma_c}} \right)^2 \sigma^2(R_{\gamma_c}) \right]^{1/2}. \quad (\text{D.62})$$

From Eq. (D.61),

$$\frac{\partial \phi_0}{\partial R_{\gamma_c}} = 3.3780. \quad (\text{D.63})$$

Therefore

$$\sigma(\phi_0) = \left[(3.3780)^2 (158.23)^2 \right]^{1/2} = 228.58. \quad (\text{D.64})$$

Substituting all the values the propagation error for free field thermal flux is

$$\sigma(\phi_\infty) = \left[(281.1)^2 (182.78)^2 + (176.44)^2 (158.23)^2 + (0.257)^2 (228.58)^2 \right]^{1/2} \quad (\text{D.65})$$

And finally the propagation error is

$$\sigma(\phi_\infty) = 58474.546 \text{ cm}^{-2} \text{ s}^{-1}. \quad (\text{D.66})$$

Therefore the free field thermal flux is

$$\phi_\infty = 6.96 \times 10^6 \pm 0.58 \times 10^6 \text{ cm}^{-2} \text{ s}^{-1}. \quad (\text{D.67})$$

Calculation of propagation of error for epithermal flux

Using Eq. (4.54) the Free filed epithermal flux is

$$\phi_\infty = \frac{1}{F_1 F_2} \bar{\phi}, \quad (\text{D.68})$$

which can also be written as

$$\phi_\infty = \frac{1}{F_1 F_2} (18 \phi_0). \quad (\text{D.69})$$

Using Eq. (D.61), Eq. (D.42), and $F_2 = 1$

$$\phi_\infty = \frac{1}{F_1} (18 \times 3.3780 R_{\gamma_c}) = 100.54 \times R_{\gamma_c}. \quad (\text{D.70})$$

The corresponding propagation of error is

$$\sigma_{\phi_{\infty}} = \left[\left(\frac{\partial \phi_{\infty}}{\partial R_{\gamma_c}} \right)^2 \sigma_{R_{\gamma_c}}^2 \right]^{1/2} \quad (\text{D.71})$$

$$\sigma_{\phi_{\infty}} = \left[(100.54)^2 \sigma_{R_{\gamma_c}}^2 \right]^{1/2} \quad (\text{D.72})$$

$$\sigma_{\phi_{\infty}} = \left[(100.54)^2 (158.23)^2 \right]^{1/2} \quad (\text{D.73})$$

$$\sigma_{\phi_{\infty}} = 15908.44. \quad (\text{D.74})$$

Therefore the free field epithermal flux is

$$(\phi_{\infty})_{epi} = 1.54 \times 10^6 \pm 0.016 \times 10^6 \text{ cm}^{-2} \text{ s}^{-1}. \quad (\text{D.75})$$

Appendix E - Calculation of Dose

The Panoramic Irradiator contains a ^{137}Cs source. The source strength at the reference date, Oct. 26, 2006 is 67 mCi. This source emits gamma ray at energy of 0.662 keV with 85% frequency. Therefore the emission rate can be written as

$$67(3.7 \times 10^7) 0.85 = 21.07 \times 10^8 \text{ gamma rays per second} \quad (\text{E.1})$$

The activity on the experiment date was calculated using Eq. (4.2)

$$A = A_0 e^{-\lambda t} \quad (\text{E.2})$$

The half life of ^{137}Cs is, $t_{1/2} = 30.07$ yrs, therefore

$$\lambda = \frac{0.693}{t_{1/2}} = 0.023046 \quad (\text{E.3})$$

Table - E.1. Source Reference Date, Experiment Date, Elapsed Time and Activity on Experiment Date.

Source reference date	Experiment Date	Elapsed Time, t (yrs)	Activity on Experiment Date, S_p (dps)
Oct. 26, 2007	TLD- 600		
	Dec. 5, 2006	0.1079	21.0285×10^8
	TLD-700		
	Nov. 28, 2006	0.0887	21.0192×10^8

The dose was calculated using the Eq. (4.67)

$$D = \left(\frac{S_p}{4\pi r^2} \right) (\mathfrak{R}), \quad (\text{E.4})$$

The response function \mathfrak{R} was considered for a parallel beam of AP incidence on anthropomorphic torso phantom and for energy 0.662 MeV photon [Shultis and Faw, 2000]. Therefore

$$\mathfrak{R} = 3.2504 \times 10^{-12} \text{ Sv cm}^2 \quad (\text{E.5})$$

Calculated dose rates for different distances, using Eq. (E.3), for TLD-700 are recorded in Table-E.2 and for TLD-600 are recorded in Table-E.2 and Table-E.3 respectively.

Table - E.2. Calculated Dose Rates for TLD-700 Dosimeters at Different Distances from the Source.

Distance (cm)	Dose rate (Sv s ⁻¹)	Dose rate (mSv h ⁻¹)
20	1.3598E-06	4.8952
30	6.0435E-07	2.1756
40	3.3995E-07	1.2238
50	2.1756E-07	0.7832
60	1.5108E-07	0.5439

Table - E.3. Calculated Dose Rate for TLD-600 Dosimeters at Different Distances from the Source.

Distance (cm)	Dose rate (Sv s ⁻¹)	Dose rate (mSv h ⁻¹)
20	1.3592E-06	4.8931
30	6.0408E-07	2.1747
40	3.3980E-07	1.2232
50	2.1747E-07	0.7829
60	1.5102E-07	0.5436